Control of sound radiation and transmission by means of passive piezoelectric networks : modelling, optimization and experimental implementation

Giuseppe Rosi

SAPIENZA
UNIVERSITÀ DI ROMA

UPMC
PARISUNIVERSITAS

THESE DE DOCTORAT EN COTUTELLE
(TESI DI DOTTORATO IN COTUTELA)

Spécialité: MECANIQUE

présentée par (presentata da)

Giuseppe ROSI

pour obtenir le grade de (per ottenere il titolo di)

DOCTEUR DE L'UNIVERSITE PARIS 6
DOTTORE DI RICERCA in Meccanica Teorica e Applicata

Sujet de thèse

Control of sound radiation and transmission by means of passive piezoelectric networks: modelling, optimization and experimental implementation

Soutenance prevue le 9 Mars 2010 devant le jury composé de
(Discussione prevista il 9 Marzo 2010 davanti alla commissione composta da)

Massimo CUOMO (Università degli studi di Catania)	Examinateur
Francesco DELL'ISOLA (Sapienza Università di Roma)	Directeur de thèse
Jean-François DEÜ (CNAM, Paris)	Rapporteur
Angelo LUONGO (Università dell'Aquila)	Rapporteur
Jean-Dominique POLACK (UPMC-Paris 6)	Examinateur
Joël POUGET (CNRS/UPMC-Paris 6)	Directeur de thèse

Abstract:

This thesis studies the reduction of radiated and transmitted sound power by means of piezoelectric passive networks. A detailed analysis of the radiation and transmission properties of thin plates is presented, and this concept are used for the optimization of the smart structures. Two main control strategies are considered: localized and distributed control.
In localized control the piezoelectric elements are positioned in selected locations, and the circuit is optimized for concentrating the effort of control in the reduction the radiated sound power. The modelling, optimization and experimental implementation of a localized smart plate is presented.
In distributed control the transducers are uniformly disposed on the structure, exploiting this spatial distribution for controlling the radiation. The modelling of an innovative structure, the Piezoelectric Resistive Electrode plate, is described in details.

Keywords: Piezoelectricity, Structure borne sound, Passive control, distributed systems, smart structures, mechatronics

Resumé:

Cette thèse a comme objet la réduction du rayonnement acoustique des structures minces par un réseau piézoélectrique passif. Une analyse détaillé des caractéristiques de rayonnement des structures minces est présenté, avec l'objectif d'utiliser ces caractéristiques pour l'optimisation de la structure intelligente. Deux stratégies de contrôle sont considérées: contrôle localisé et contrôle distribué. Le contrôle localisé utilise un réseau de actionneurs positionnés en des endroits optimisés, et le circuit est conçu pour concentré l'effort de contrôle dans la réduction de la puissance acoustique rayonnée. La modélisation, l'optimisation et l'étude expérimentale d'une structure intelligente localisée est ici présenté. Le contrôle distribué utilise un réseau uniforme de actionneurs piézoélectriques, connecté à un circuit optimisé pour profiter de cette distribution spatiale en termes de efficacité dans la réduction de la puissance acoustique rayonnée et transmise. Une nouvelle structure intelligente, la plaque avec un électrode résistif (PRE) est ici présenté.

Keywords: Piezoelectricité, Rayonnement acoustique des structures, Contrôle passif, structures intelligentes

Contents

Chapter 1

Introduction

1.1 Motivations

One of the main aspects that contributes to the valuation of the overall quality of a certain vehicle, such as a car, a ship or an aircraft, is the noise propagating into the passenger compartment due to the vibrations of the structure or to an external source. Moreover uncontrolled vibrations can affect the reliability and durability of mechanical structures, increasing fatigue load, and consequently the risk of damaging the structure.

The study of structural vibrations, structure-borne sound and air-borne sound is then a key topic in the automotive, naval and aeronautic industry. The classical techniques adopted for reducing vibrations in vehicles are essentially based on the use of dissipative materials, e.g. viscoelastic layers bonded on the structure, or on added mass. While these techniques have the advantage of being easy to optimize, they have as main drawback the problem of making the structure heavier, especially when trying to efficiently reduce low frequency vibrations. This is usually in counter-position with the low-weight requirements, especially for aeronautic and aerospace applications. In order to overcome this difficulties, the research on active materials, as piezoelectric ceramics, shape memory alloys, electrostrictive and magnetic materials, increased over the last twenty years. Their advantages with respect to traditional solutions are reduced mass and weight, high performances and adaptability. This work will focus on the application of piezoelectric materials for reducing the sound power radiated and transmitted by thin plane structures. Examples of techniques that do not use piezoelectric actuators can be found in [Li 2007, MasahiroToyoda 2005, Larbi 2006].

The use of piezoelectric elements for vibration control is widely diffused in the literature, because of their property of generating an electric charge when subjected to mechanical strains, the so called *direct* piezoelectric effect, and vice-versa of generating a local deformation when a charge or a voltage is applied, the *inverse* piezoelectric effect. Exploiting these properties, piezoelectric materials can be used as sensors and actuators. Furthermore one single transducer can be also used co-located[1] sensor.

[1] A co-located sensor-actuator pair is a transducer capable of measuring a quantity and

When an electronic circuit is connected to this sensor-actuator network bonded to the structure, the dynamic of the circuit influences that of the mechanical system. There exist several categories of vibration control using piezoelectric transducer, the main are:

- **Active control circuits:** in active control circuit the signal read by sensor is processed, amplified and sent through the control circuit to the actuators. This kind of systems can be very effective, but as drawback they require high power electronics and, since they supply power to the mechanical system, they can cause instability.

- **Passive and semi-passive control circuits:** passive control strategies are obtained shunting the piezoelectric transducers with an optimized network of optimized passive components. Being the control circuit passive, it cannot supply power to the system and then it cannot cause instability. Since very often this control networks are too complex for a discrete passive realization, they are realized using active components, while the control law remaining passive. This systems are called semi-passive, since they require power. In this category we place also the switch-shunts.

Even though each of these approaches has its advantages and drawbacks this study is focused on passive and semi-passive control. The choice of using a passive control law is mainly motivated by the already mentioned stability issues. Another reason is that a passive circuit does not need, in principle, any external power supply and can then be suitable for aerospace applications, where power electronics cannot be used.

The main principle behind a passive control law is the following: connecting a mechanical and an electrical system creates an energy flow, from the mechanical form to the electrical form and vice versa. Subtracting mechanical energy and dissipating it into a non-conservative electric circuit is a means to damp mechanical vibrations. The control technique is then related to the optimization of the energy flow and the non-conservative part of the circuit. Examples of active control systems can be found in [Carneal 2004, Lee 1999b, Lee 1999a, Strassberger 2000, Gardonio 2005, Gardonio 2004, Zhang 2004, Chomette 2008, Trindade 2007].
When considering passive control two main strategies are possible: localized control and distributed. The first approach uses a control system with optimally placed piezoelectric patches [Halim 2003, Gawronski 1997], connected to a circuit operating in selected frequency windows. With respect to the distributed controller this scheme uses a smaller number of piezoelectric elements and, usually, a simpler circuit. Examples can be

acting on the same quantity, or another, in the same location.

found in [Carneal 2004, Behrens 2003, Lee 1999b, Zhang 2004, Ozer 2003]. However, it can introduce a performance trade-off in terms of amount of vibrational energy transferred to the circuit.
A different approach for solving the same problem considers a distributed piezoelectric network connected to a passive or semi-passive modular circuit, optimized for harvesting mechanical energy of the plate and dissipating it into the non conservative part of the circuit. The uniform spatial distribution of sensors and actuators permits to have, with optimized electrical parameters, the duality between the electrical circuit and the mechanical structure. This duality has as its consequence the superposition of the electric and mechanic eigenfrequencies and then permits an optimal energy flow. This passive technique assures stability and optimized broadband control. Applications of this technique can be found in [Maurini 2005, dell'Isola 2003, Alessandroni 2004, Alessandroni 2002].

Finding the solution of the acoustic problem implies difficult calculations and sometimes an analytical solution of the considered problem does non even exist. Following [Wallace 1972, Elliott 1993, Borgiotti 1994, Bai 2002] the elementary radiator decomposition and the concept of radiation spatial filters will be used in order to reduce the computational cost of the analytical treating and to make the synthesis of the controller easier. With the study of the dispersion relations of the waves, propagating through the fluid and the structure, it is possible to obtain optimal parameters for the components and for the acoustic purposes. This is a crucial step for the optimization of the control strategy and for developing an ad-hoc controller.

1.2 Objectives

The objective of this work is to model and optimize passive and semi-passive piezoelectric smart structures, with the aim of reducing the radiated and transmitted sound power.
In particular the main themes that will be investigated are

- Study of the radiation and transmission properties of thin plates, including a modal approach to the analysis of the radiation properties of the structure. Analysis of the transmission properties of single and double plate structures.

- Model and optimization of a passive localized and distributed piezoelectric smart plate for reducing the radiated sound power. Introduction of an optimization procedure based on acoustic principles, for the piezoelectric patches placement. Experimental tests.

- Modelling and optimization of a passive distributed piezoelectric smart plate for reducing radiated and transmitted sound power. Introduction of a novel passive structure to overcome the problems related to the complexity of the circuitry.

1.3 Outline

The thesis is organized with an introductory part (Chapters 1 and 2), a core part reporting the theoretical works and numerical simulations (Chapters 3 and 4), an experimental part (Chapter 5) and a closure (Chapter 6). Each chapter of the core part includes a specific introduction and a dedicated literature review.

Chapter 2 is a general introduction to the acoustic properties of thin structures, and introduces all the performance indices that will be used in the following chapters. A detailed analysis of the radiation properties of thin plates is included, along with the definition of the modal radiation efficiency. The study of the transmission of a plane wave and of a diffuse sound field through single and double plates is also investigated.

Chapter 3 is about the modelling and optimization procedure of a localized piezoelectric smart plate. First of all the modal model of the plate is derived, using a variational formulation. Then several passive multimodal control networks are presented, along with their optimization processes. After this, an acoustically based optimization procedure for the piezoelectric actuators positioning is introduced, using the novel concept of acoustical controllability. The final section of the chapter is devoted to a simulation of the acoustic behaviour of a smart plate conceived and optimized following the previous considerations.

Chapter 4 is devoted to the modelling and optimization of a distributed piezoelectric smart structure. A novel type of distributed smart plate, the Piezoelectric Resistive Electrode (PRE) plate, is presented. The model of the PRE plate is derived using a variational principle, and the optimization of the electrical parameters is described in detail. Finally the behaviour of PRE plate in terms of radiation and transmission properties is compared with other multimodal electric and viscoelasitc passive control strategies.

Chapter 5 resumes the experimental works about the optimization of a localized piezoelectric smart structures, following the procedures described in Chapter 3. The full process of conception and assembling of the smart structure is here described in detail. Acoustic measures of the radiated sound pressure are presented, in order to confirm the effectiveness of the proposed control strategies.

Finally Chapter 6 is left for conclusions and suggestions for further extensions of the present work.

Chapter 2

Sound radiation and transmission of plates

Contents

Object of the Chapter

This chapter is a general introduction to the acoustic properties of thin structures, and introduces all the performance indices that will be used in the following chapters. A detailed analysis of the radiation properties of thin plates is included, along with the definition of the modal radiation efficiency. The study of the transmission of a plane wave and of a diffuse sound field through single and double plates is also investigated.

2.1 Equation of acoustic propagation in linear acoustics

Since acoustics is defined as the dynamics of small perturbations of a compressible fluid, the starting point is the study of fundamental equations of continuum mechanics, such as conservation, state and behaviour equations. Starting from a generic formulation, the linear equations for small perturbation around a steady state will be briefly derived, following [Cremer 1973, Fahy 2001, Filippi 1984, Ohayon 1998].

- **Conservation of the mass**: Let Ω be a closed volume filled with a homogeneous media with volume density ρ. Then the total mass is $M(\Omega) = \int_\Omega \rho d\Omega$, and the mass conservation equation for any volume Ω is

$$\frac{\mathrm{d}}{\mathrm{d}t}\int_\Omega \rho d\Omega = f_i, \tag{2.1}$$

  where f_i is a source of mass and $\dfrac{d}{dt}$ is the material derivative of a volume integral.

- **Conservation of the linear momentum**: being $\mathbf{v}$, $\mathbf{T}$ and $\mathbf{b}_v$ the velocity of a particle, the stress tensor and the volume density of the applied forces, the conservation equation for the linear momentum with boundary $\partial\Omega$ and its normal $\underline{\mathbf{n}}$ is

$$\frac{\mathrm{d}}{\mathrm{d}t}\int_\Omega \rho\mathbf{v} d\Omega = \int_{\partial\Omega} \mathbf{T}\cdot\underline{\mathbf{n}} dS + \int_\Omega \mathbf{b}_v\cdot\mathbf{v} d\Omega \tag{2.2}$$

- **Conservation of the energy** : being e, $\mathbf{q}$, r the internal energy, the heat flow and the heat source density, the energy conservation equation is

$$\frac{\mathrm{d}}{\mathrm{d}t}\int_\Omega \rho\left(e+\frac{1}{2}\mathbf{v}^2\right) d\Omega = \int_{\partial\Omega} \left(\mathbf{T}\cdot\underline{\mathbf{n}} - \mathbf{q}\right)\underline{\mathbf{n}}\, dS + \int_\Omega \left(\mathbf{b}_v + r\right) d\Omega. \tag{2.3}$$

The lemma of material derivatives on a volume leads to:

$$\frac{\mathrm{d}}{\mathrm{d}t}\int_\Omega \varphi d\Omega = \int_\Omega \left(\frac{\mathrm{d}}{dt}\varphi + \varphi\,\mathrm{div}(\mathbf{v})\right) d\Omega = \int_\Omega \left(\frac{\partial}{\partial t}\varphi + \mathrm{div}(\varphi\mathbf{v})\right) d\Omega, \tag{2.4}$$

where

$$\frac{\mathrm{d}}{\mathrm{d}t}\varphi = \dot{\varphi} + \mathbf{v}\cdot\mathbf{grad}(\varphi\mathbf{v})$$

is the material derivative of a function and $\dot{\square}$ denotes a first order time derivative.

Using equation (2.4), considering that conservation equations must be independent of the volume Ω, using the symmetry of the stress tensor one can write a local form for equations (2.1), (2.2) and (2.3) as:

$$\frac{\mathrm{d}}{\mathrm{d}t}\rho + \rho \operatorname{div} \mathbf{v} = f_i, \tag{2.5a}$$

$$\rho \frac{\mathrm{d}}{\mathrm{d}t}\mathbf{v} - \operatorname{div} \mathbf{T} = \mathbf{b}_v, \tag{2.5b}$$

$$\rho \frac{\mathrm{d}}{\mathrm{d}t}e + \operatorname{div} \mathbf{q} = \mathbf{T} : \mathbf{S} + r, \tag{2.5c}$$

where $\mathbf{S}$ is the strain tensor.

2.1.1 State equation

The state equation describes the current thermodynamic state of the system. For a fluid a state equation can be written choosing two independent thermodynamic variables. With the choice of entropy s and specific volume $v = \rho^{-1}$, the internal energy has the form $e = e(s, v)$.
Considering its first differential the *Gibbs equation* is obtained:

$$\mathrm{d}e = T\mathrm{d}s - p\mathrm{d}v, \tag{2.6}$$

where $T = \left(\frac{\partial e}{\partial s}\right)_v$ is the temperature and $p = \left(\frac{\partial e}{\partial v}\right)_s$ the pressure. In acoustics, being the perturbations very small, a first differential approximation is enough accurate. Then, using equation (2.6) the energy balance, equation (2.5c) becomes

$$T\rho \frac{\mathrm{d}}{\mathrm{d}t}s = \boldsymbol{\Theta} : \mathbf{S} - \operatorname{div} \mathbf{q} + r \tag{2.7}$$

where $\boldsymbol{\Theta} = \mathbf{T} - p\mathbf{I}$ is the viscous stress tensor (being $\mathbf{I}$ the identity tensor).

2.1.2 Equation of acoustic propagation and linear acoustic approximation

In this section the equations of propagation for acoustic waves into a fluid will be derived.
For sake of simplicity dissipative phenomena in the fluid can be neglected, i.e. $\boldsymbol{\Theta} = 0$. Then supposing that there is not any heat flow, volume force density and heat source, that means $\mathbf{q}$, $\mathbf{b}_v$ and $r = 0$, the system (2.5) then finally becomes:

$$\frac{\mathrm{d}}{\mathrm{d}t}\rho + \rho \operatorname{div} \mathbf{v} = f_i, \tag{2.8a}$$

$$\rho \frac{\mathrm{d}}{\mathrm{d}t}\mathbf{v} + \mathbf{grad}\, p = 0, \tag{2.8b}$$

$$T\rho \frac{\mathrm{d}}{\mathrm{d}t}s = 0, \tag{2.8c}$$

Then applying the definition of material derivative

$$\dot{\rho} + \mathbf{v}\,\mathbf{grad}\,\rho + \rho\,\mathrm{div}\,\mathbf{v} = f_i, \tag{2.9a}$$

$$\rho\dot{\mathbf{v}} + \rho\mathbf{v}\cdot\mathbf{grad}\,\mathbf{v} + \mathbf{grad}\,p = 0, \tag{2.9b}$$

$$T\rho\,(\dot{s} + \mathbf{v}\,\mathbf{grad}\,s) = 0, \tag{2.9c}$$

Considering linear variations near an homogeneous steady state the variables are rewritten as

$$\rho = \rho^0 + \rho^1,\ p = p^0 + p^1,\ \mathbf{v} = \mathbf{v}^1, s = s^0 + s^1,\ f_i = f_i^0 + f_i^1 \tag{2.10}$$

where with the superscripts $\square^0$ and $\square^1$ an initial state and a variation of the respective quantity are identifies. Being the initial condition a steady state, this implies $\rho^0 = \text{const}$, $p^0 = \text{const}$, $s^0 = 0$, $f_i^0 = 0$, $\mathbf{v} = 0$.
Then the first order terms system (2.9) are

$$\dot{\rho}^1 + \rho^0\,\mathrm{div}\,\mathbf{v}^1 = f_i, \tag{2.11a}$$

$$\rho^0\dot{\mathbf{v}}^1 + \mathbf{grad}\,p^1 = 0, \tag{2.11b}$$

$$T^0\rho^0\dot{s}^1 = 0, \tag{2.11c}$$

The second order differential of the state equation (2.6) gives the following equations:

$$T^1 = \frac{T^0}{C_v^0}s^1 + \frac{1}{\rho^0\alpha_s^0}\rho^1 \tag{2.12a}$$

$$p^1 = \frac{\rho^0}{\alpha_v^0}s^1 + \frac{1}{\rho^0\chi_s^0}\rho^1 \tag{2.12b}$$

From equation (2.11c) it is evident that the process is adiabatic, i.e. $\frac{\partial s^1}{\partial t} = 0$. This implies

$$p^1 = \frac{1}{\rho^0\chi_s^0}\rho^1 \tag{2.13}$$

that is

$$\rho^1 = \rho^0\chi_s^0 p^1 \tag{2.14}$$

Substituting the last equation into system (2.11) gives

$$\rho^0\chi_s^0\,\dot{p}^1 + \rho^0\,\mathrm{div}\,\mathbf{v}^1 = f_i, \tag{2.15a}$$

$$\rho^0\dot{\mathbf{v}}^1 + \mathbf{grad}\,p^1 = 0, \tag{2.15b}$$

Then considering the partial time derivative of equation (2.15a) minus the divergence of equation (2.15b) leads to

$$\rho^0\chi_0^s\,\ddot{p}^1 - \mathrm{div}\,(\mathbf{grad}\,p^1) = \dot{f}_i.$$

Introducing $c = \sqrt{\rho^0\chi_s^0}$ as the speed of sound in the specific medium the linearized equation of propagation in the final form is:

$$\ddot{p}^1 - \frac{1}{c^2}\mathrm{div}\,(\mathbf{grad}\,p^1) = \dot{f}_i. \tag{2.16}$$

It is easy to notice that equation (2.16) is a d'Alembert equation and then each solution is a wave propagating into the medium. In order to simplify the notation the superscript which denote the linear approximation will be neglected throughout the rest of the thesis.

$$\ddot{p} - \frac{1}{c^2}\mathrm{div}\,(\mathbf{grad}\,p) = \dot{f}_i. \tag{2.17}$$

Remark 1. *The only source for acoustic pressure is then the time derivative of the injection of mass $\dot{f}_i$, that represents any common structural acoustic source. Vibrating surfaces are to be considered as pistons injecting matter into the considered volume.*

2.2 Sound Radiation of plane structures

In this section the radiation properties of finite plate in an infinite baffle, figure (2.1) are investigated. The main performance indexes used for determining the radiation properties of a structure will be introduced, as well as optimized computational methods for calculating these values. Finally a modal approach to the estimation of the radiated sound power will be described. The introduction of modal radiation efficiency coefficients will be crucial towards the acoustic optimization of the controllers proposed in next chapters.

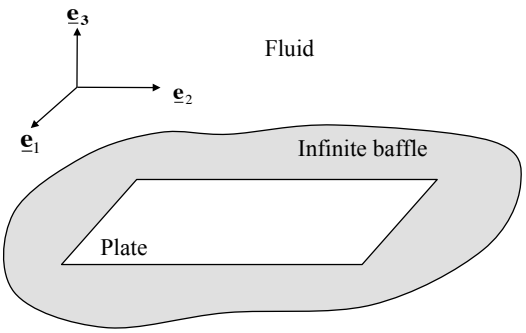

Figure 2.1: Finite plate in an infinite baffle

2.2.1 Far Field Sound Pressure

The acoustic pressure at a generic point of the space due to the transverse motion w_0 of a portion S of the plate can be calculated using the Rayleigh formula:

$$\widehat{p}(\mathbf{p},\omega,S) = \frac{j\omega\rho}{2\pi}\int_S \frac{e^{-j\mathbf{k}(\mathbf{p}-\mathbf{r})}}{\mathbf{p}-\mathbf{r}}\widehat{w}_0(\mathbf{r},\omega)dS, \tag{2.18}$$

where $\widehat{\square}$ denotes a quantity in frequency domain and $\mathbf{k} = (\omega/c\ \underline{\mathbf{k}})$ is the wave vector of a sound wave propagating in a light fluid along direction $\underline{\mathbf{k}}$.

This is a very important performance index, since it is related to a physical quantity that can be easily measured, such as the pressure. In the literature there exists a standard method for measuring this quantity, see [ISO 3745 1977] and figure 2.2.

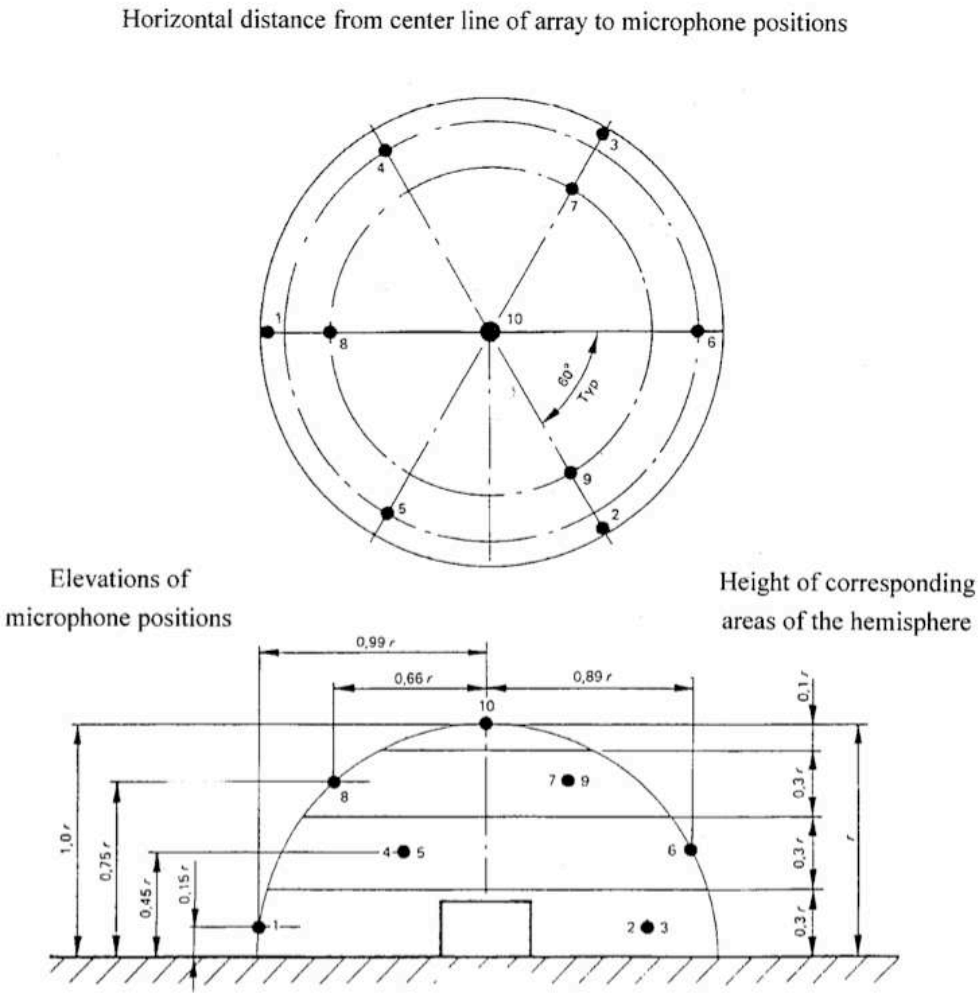

Figure 2.2: Microphone positions according to [ISO 3745 1977]

2.2.2 Sound Power at plate level

The radiated power at the plate level can be expressed by the surface integral of the product between the pressure in each point of the plate, calculated with equation (4.43), multiplied by its velocity:

$$\pi_r(\omega, S) = \frac{1}{2}\int_S Re\left\{(\widehat{p}(\mathbf{r},\omega)|_{z=0}) \cdot (j\omega\widehat{w}_0(\mathbf{r},\omega))^*\right\} dS, \tag{2.19}$$

where $\square^*$ is a conjugate quantity.
This is a global parameter that gives us different informations with respect

to the far field pressure, since it involves also the near field, but it is not a measurable quantity. Unfortunately this double integral very often does not admit an analytical solution, therefore a optimized numerical approach is needed for calculating the radiated sound power.

Spatial radiation filters and modal radiation efficiency

The procedure here proposed has a double advantage:

- reduces the computational cost of calculating the radiated sound power
- introduces modal radiation coefficients

The first step consists in performing a standard modal decomposition of the transverse velocity field of the plate, in terms of the sum of the modal shapes $\Psi_i(\mathbf{r})$ and the corresponding modal velocity coefficients $y_i(\omega)$:

$$\widehat{v}(\omega, \mathbf{r}) = \sum_{i=1}^{N} y_i(\omega)\Psi_i(\mathbf{r}) \tag{2.20}$$

Then using equation (4.43), the pressure at the point $\mathbf{r}_1$ due to the velocity of the point $\mathbf{r}_2$, where $\mathbf{r}_1$ and $\mathbf{r}_2$ are both points of the plate, i.e. $(\mathbf{r}_1, \mathbf{r}_2) \in S$ is

$$\widehat{p}(\omega, \mathbf{r}_1) = \frac{\rho}{2\pi} \int_S \frac{e^{-j\mathbf{k}\cdot(\mathbf{r}_2-\mathbf{r}_1)}}{(\mathbf{r}_2-\mathbf{r}_1)} \widehat{v}(\omega, \mathbf{r}_2) dS. \tag{2.21}$$

Substituting the modal decomposition for the transverse velocity, equation (2.20), into equation (2.21) gives

$$\widehat{p}(\omega, \mathbf{r}_1) = \sum_{i=1}^{N} y_i(\omega) \frac{\rho}{2\pi} \int_S \frac{e^{-\frac{j\omega}{c}\underline{\mathbf{k}}\cdot(\mathbf{r}_2-\mathbf{r}_1)}}{(\mathbf{r}_2-\mathbf{r}_1)} \Psi_i(\mathbf{r}_2) dS, \tag{2.22}$$

that is the modal decomposition for the pressure field. Then using equations (2.20) and (2.22) into equation (4.44) a reduced modal expression of the radiated power can be written as:

$$\tilde{\pi}(\omega, S) = \sum_{i=1}^{N} |y_i(\omega)|^2 \frac{\rho}{2\pi} \int_S \int_S \frac{e^{-\frac{j\omega}{c}\underline{\mathbf{k}}\cdot(\mathbf{r}_2-\mathbf{r}_1)}}{(\mathbf{r}_2-\mathbf{r}_1)} \Psi_i(\mathbf{r}_2)\Psi_i^*(\mathbf{r}_2) dS dS \tag{2.23}$$

that can be rewritten as

$$\tilde{\pi}_r(\omega) = \sum_{i=1}^{n} \eta_i(\omega)|y_i(\omega)|^2 \tag{2.24}$$

where

$$\eta_i(\omega) = \frac{\rho}{2\pi} \int_S \int_S \frac{e^{-\frac{j\omega}{c}\underline{\mathbf{k}}\cdot(\mathbf{r}_2-\mathbf{r}_1)}}{(\mathbf{r}_2-\mathbf{r}_1)} \Psi_i(\mathbf{r}_2)\Psi_i^*(\mathbf{r}_2) dS dS. \tag{2.25}$$

Equation (2.25) defines the modal radiation efficiency for the i^{th} vibration mode of the plate, and depends only on the geometry of the plate and the properties of the fluid. From equation (2.24) the radiated power is then a quadratic function of the modal velocity, weighted by the modal efficiency coefficient.

Finding the analytical solutions for equation (2.25) is complicated, as it was finding the solution of (4.44). Then, following the literature, see [Elliott 1993, Bai 2002, Borgiotti 1994], a discretization of the domain will be performed in order to deal with sums instead that with integrals. The plate domain is then divided in a matrix of M elements, radiating as pistons, and the discrete form of equation (4.44) is

$$\pi_r(\omega) = \frac{A}{2}\Re\left\{\mathbf{v}^H(\omega)\cdot\mathbf{p}(\omega)\right\}, \tag{2.26}$$

where $\mathbf{v}$ is the vector of the complex velocities, $\mathbf{p}$ is the vector of the pressure immediately in front of each element averaged on the surface A of each element and $\Re\{\cdot\}$ denotes the real part of a complex vector.
Being the velocity field known by modal analysis, and given that the pistons are radiating as plane surfaces with transverse velocity, the pressure on the n^{th} piston due to the velocity of the m^{th} can be calculated with equation (4.43)

$$\mathbf{p}_n(\omega) = \frac{\rho}{2\pi}\int_S \frac{e^{-jkr_{n,m}}}{r_{n,m}}\mathbf{v}_m(\omega)dS, \tag{2.27}$$

For a plate in an infinite baffle the pressure vector can then be then rewritten as

$$\mathbf{p} = R\mathbf{v}$$

The matrix R is a real, symmetric, positive definite matrix whose elements can be analytically calculated:

$$R(\omega) = \frac{\omega^2\rho A^2}{4\pi c}\begin{bmatrix} 1 & \frac{\sin(k\,r_{1,2})}{k\,r_{1,2}} & \dots & \frac{\sin(k\,r_{1,M})}{k\,r_{1,M}} \\ \frac{\sin(k\,r_{2,1})}{k\,r_{2,1}} & 1 & \dots & \dots \\ \dots & \dots & \dots & \dots \\ \frac{\sin(k\,r_{M,1})}{k\,r_{M,1}} & \dots & \dots & 1 \end{bmatrix}, \tag{2.28}$$

where ρ is the density of the medium, c the speed of sound in the medium, S the area of the elementary radiating element and $\mathbf{r}_{n,m}$ the distance between the n^{th} and the m^{th} piston.

Remark 2. *For a plate in an infinite baffle the matrix R only depends on the dimensions of the plate and the characteristics of the fluid.*

Since R is a real, symmetric, positive definite matrix it is always possible to perform an eigenvalue/eigenvector decomposition

$$R(\omega) = Q^T(\omega)\Lambda(\omega)\,Q(\omega),$$

where Q is a $N \times M$ matrix, whose columns $\mathbf{q}_i$ are the eigenvectors, here called radiation filters, and Λ the diagonal matrix of the eigenvalues. These radiation filters $\mathbf{q}_i$, also called radiation modes in the literature, can be interpreted as optimal velocity patterns in terms of radiation efficiency and they depend on frequency, as well as their associated eigenvalue. An example of

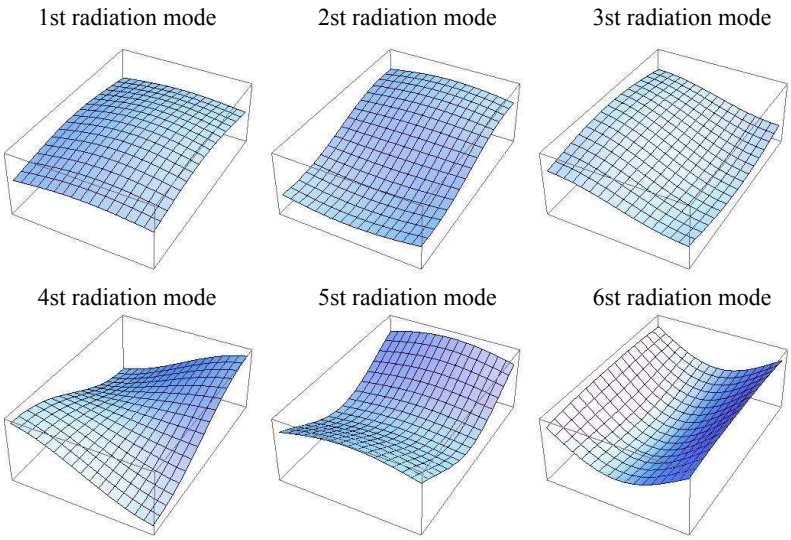

Figure 2.3: First six radiation filters of a rectangular plate at 1kHz

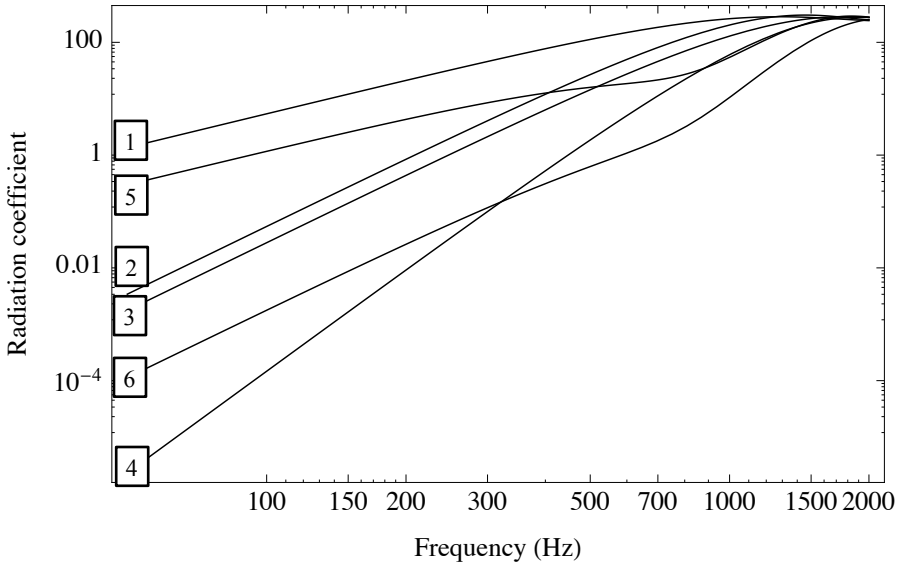

Figure 2.4: Eigenvalues associated to the first six radiation filters of a rectangular plate.

the first six radiation filters for a rectangular plate is shown in figure 2.3. The corresponding eigenvalues are plotted in figure 2.4. Being R a large matrix that depends on frequency, performing an eigenvalue/eigenvector decomposition can be a cumbersome task in terms of computational cost. Since is

known from the literature, [Elliott 1993], that the largest amount of the radiated power is due to the first radiation filters, only the first L radiation filters will be considered. In this reduced model the reduced eigenvectors and eigenvalues matrix are $\tilde{Q}_{L\times M}$ and $\tilde{\Lambda}_{L\times L}$, and consequently the radiation matrix is

$$R(\omega)=\tilde{Q}^T(\omega)\,\tilde{\Lambda}(\omega)\tilde{Q}(\omega).$$

Each eigenvalue $\tilde{\lambda}_i(\omega)=\tilde{\Lambda}_{ii}(\omega)$ represents the radiation efficiency of each radiation filter, and its value depends on frequency. For the radiation properties of a plate coupled with a light fluid, these eigenvalues will have a high-pass behaviour and for frequencies $f > f_c$, where f_c is the critical frequency, they all contribute equally to the radiation, see figure 2.4. This critical frequency depends only on the geometry of the plate and the properties of the fluid. Hence, in order to reduce computational costs for calculating the radiated sound power the so called *nesting property* of radiation filters, as discussed in [Borgiotti 1994], can be used. Considering two frequencies f_1 and f_2 so that $f_1 < f_2$, the nesting property imply that:

$$Span\left\{\mathbf{q}\left(f_1\right)\right\} \subset Span\left\{\mathbf{q}\left(f_2\right)\right\}. \tag{2.29}$$

The meaning of equation (2.29) is the following: if the eigenvalue corresponding to a radiation filter calculated at f_2 is set to zero, that means no radiation, every radiation filter for $f_1 < f_2$ will be set to zero as well. Since we are interested in controlling the radiation in a limited frequency band, we use this result to simplify the calculations. After these considerations it is possible to write the final approximated form for the radiation resistances matrix calculated at f_{max}

$$R_{\max}(\omega) = \tilde{Q}^T_{\max}\,\tilde{\Lambda}(\omega)\tilde{Q}_{\max},$$

where $\tilde{Q}_{\max}$ is the matrix of the eigenvectors calculated at $f_{\max}$, i.e. the maximum frequency of interest. We can now write an approximated equation for the radiated power

$$\tilde{\pi}(\omega) = \mathbf{v}^H(\omega)\tilde{Q}^T_{\max}\,\tilde{\Lambda}(\omega)\tilde{Q}_{\max}\mathbf{v}(\omega).$$

The compact form of equation (2.20) is

$$\mathbf{v}(\omega) = \Psi\,\mathbf{y}(\omega),$$

where $\mathbf{\Psi}_{N\times M}$ is the matrix of modal shapes. Therefore the expression of the radiated power becomes

$$\begin{aligned}\tilde{\pi}_r(\omega) &= \left(\Psi\,\mathbf{y}(\omega)\right)^H\,\tilde{Q}^T_{\max}\,\tilde{\Lambda}(\omega)\tilde{Q}_{\max}\left(\Psi\,\mathbf{y}(\omega)\right) = \\ &= \mathbf{y}^H(\omega)\left(\Psi\,\tilde{Q}_{\max}\right)^H\tilde{\Lambda}(\omega)\left(\Psi\,\tilde{Q}_{\max}\right)\underline{\mathbf{y}}(\omega) = \mathbf{y}^H(\omega)\tilde{E}(\omega)\,\mathbf{y}(\omega)\end{aligned}$$

where

$$\tilde{E}(\omega) = \left(\Psi\,\tilde{Q}\right)^H_{\max}\tilde{\Lambda}(\omega)\left(\Psi\,\tilde{Q}_{\max}\right)$$

is the diagonal matrix of the approximated modal radiation efficiencies. Then the expression of the approximated modal efficiency for each structural mode is:

$$\tilde{\eta}_i(\omega) = \tilde{E}_{ii}(\omega) = \sum_{n}^{L} \lambda_n(\omega) \underline{\tilde{\mathbf{\Psi}}}_i \cdot \underline{\tilde{\mathbf{Q}}}_n^{\max} \tag{2.30}$$

In words each modal radiation efficiency coefficient is determined by the sum of the projection of that structural mode on each radiation filter, weighted by the efficiency of that filter. Each coefficient $\tilde{\eta}_i$ is the approximation of the integral radiation coefficient η_i defined in (2.25). Then the approximated expression for the radiated power is

$$\tilde{\pi}_r(\omega) = \sum_{i=1}^{N} \eta_i(\omega) |y_i(\omega)|^2.$$

Since $\eta_i(\omega)$ is a function of the radian frequency in order to know how much a structural mode effectively radiates the value of the i^{th} coefficient can be calculated at the corresponding radian frequency ω_i. The effective modal efficiency is then defined as follows:

$$\overline{\eta}_i = \eta_i(\omega_i) \tag{2.31}$$

These coefficients will be used for optimizing the controller.

Remark 3. *Since the efficiency of each vibrational mode is calculated form the efficiency of the radiation filters, and since this efficiency has has a low pass filter behaviour, these concepts can be used only at low frequencies, below the critical frequency f_c.*

2.3 Infinite thin plates

In this section the behaviour of infinite thin plates in terms of radiation and transmission properties is analysed. This is done according to the procedure described in the literature, [Cremer 1973, Fahy 2001, Filippi 1984, Fahy 1985].

2.3.1 Impedance of an infinite thin plate

In order to efficiently describe the plate fluid interaction the concept of plate impedance will be here introduced. Since the fluid plate interaction can be modelled as a pressure acting on the plate surface the impedance will be defined as the ratio between this pressure and the induced displacement.

$$Z(\omega, k_x, k_y) = \frac{p(x,y)}{w(x,y)} \tag{2.32}$$

The pressure source is introduced as an unitary progressive plane wave on the surface:

$$p(x,y) = e^{-j(k_x x + k_y y)} \tag{2.33}$$

The response of the plate in terms of displacement will be a solution of the generic plate equation

$$\mathcal{L}\{w(x,y)\} = e^{-j(k_x x + k_y y)} \tag{2.34}$$

Since $\mathcal{L}\{\cdot\}$ is a linear differential operator the solution will be in the form

$$w(x,y) = A(\omega, k_x, k_y) e^{-j(k_x x + k_y y)}. \tag{2.35}$$

The expression of A depends on the differential operator $\mathcal{L}\{\cdot\}$ and will always be a function of ω, k_x and k_y. Then the impedance of the plate is

$$Z(\omega, k_x, k_y) = \frac{p(x,y)}{w(x,y)} = \frac{1}{A(\omega, k_x, k_y)} \tag{2.36}$$

It is important to denote that the impedance is a pair function of the wavenumbers, so that $Z(\omega, k_x, k_y) = Z(\omega, -k_x, -k_y)$. This implies that the impedance is independent on the sense of propagation. A general expression of the impedance that will be considered in this work is

$$Z(\omega, k_x, k_y) = \underbrace{D(k_x^2 + k_x^2)^2}_{stiffness} - \underbrace{m\omega^2}_{inertia} + \underbrace{\Gamma(\omega, k_x, k_y)}_{piezoelectric\ coupling} \tag{2.37}$$

Any sort of mechanical damping will be modelled using complex stiffness coefficients and any electrical damping is included into the piezoelectric coupling term.

2.3.2 Sound radiation and propagation of coupled waves

Consider two half-spaces filled by identical light fluids, separated by an infinite plate placed at $z = 0$. The equation of motion and the boundary conditions are the following:

Fluid 1 ($z < 0$)

$$\nabla^2 p_1 + \frac{\omega^2}{c^2} p_1 = 0 \tag{2.38a}$$

$$\left.\frac{\partial p_1}{\partial z}\right|_{z=0} = \rho\omega^2 w \tag{2.38b}$$

$$\text{Sommerfeld condition}^1 \text{ at infinity} \tag{2.38c}$$

[1] in 1912 Arnold Sommerfeld defined the condition of radiation for a scalar field satisfying the Helmholtz equation as *"the sources must be sources, not sinks of energy. The energy which is radiated from the sources must scatter to infinity; no energy may be radiated from infinity into ... the field."*.

Fluid 2 ($z > 0$)

$$\nabla^2 p_2 + \frac{\omega^2}{c^2} p_2 = 0 \tag{2.39a}$$

$$\left.\frac{\partial p_2}{\partial z}\right|_{z=0} = \rho\omega^2 w \tag{2.39b}$$

$$\text{Sommerfeld condition at infinity} \tag{2.39c}$$

Plate ($z = 0$)

$$\mathcal{L}\{w\} = (p_1 - p_2)_{z=0}\,, \tag{2.40}$$

where $\mathcal{L}\{\cdot\}$ is a generic plate operator and w is the transverse displacement of a point of the plate. Supposing no acoustic sources this kind of solutions for the pressure and transverse displacement fields are posed

$$p_1 = \left(A_x^1 e^{-jk_x x} + B_x^1 e^{jk_x x}\right)\left(A_y^1 e^{-jk_y y} + B_y^1 e^{jk_y z}\right)\left(B_z^1 e^{+jk_z z}\right) \tag{2.41a}$$

$$p_2 = \left(A_x^2 e^{-jk_x x} + B_x^2 e^{jk_x x}\right)\left(A_y^2 e^{-jk_y z} + B_y^2 e^{jk_y y}\right)\left(A_z^2 e^{-jk_z z}\right) \tag{2.41b}$$

$$w_1 = \left(C_x e^{-jk_x x} + D_x e^{jk_x x}\right)\left(C_y e^{-jk_y z} + D_y e^{jk_y y}\right) \tag{2.41c}$$

Considering equations (2.38b) and (2.39b) the following relations between the transverse displacement and the pressure fields in $z = 0$ are easily obtained

$$jk_z p_1 = \omega^2 \rho w \tag{2.42a}$$

$$-jk_z p_2 = \omega^2 \rho w \tag{2.42b}$$

Substituting these results into equation (2.40) and neglecting the trivial solution $w = 0$ the dispersive equation for the coupled system is obtained:

$$Z(\omega, k_x, k_y) + 2\frac{j\omega^2\rho}{k_z} = 0 \tag{2.43}$$

Being

$$k_z = \sqrt{\frac{\omega^2}{c^2} - k_x^2 - k_y^2}, \tag{2.44}$$

The general expression of the dispersion relation becomes

$$Z(\omega, k_x, k_y) + 2\frac{j\omega^2\rho}{\sqrt{\frac{\omega^2}{c^2} - k_x^2 - k_y^2}} = 0 \tag{2.45}$$

Then the fields are

$$p_1 = -\frac{j\omega^2\rho}{\sqrt{\frac{\omega^2}{c^2} - k_x^2 - k_y^2}} w e^{+j\sqrt{\frac{\omega^2}{c^2} - k_x^2 - k_y^2}\, z} \tag{2.46a}$$

$$p_2 = -\frac{j\omega^2\rho}{\sqrt{\frac{\omega^2}{c^2} - k_x^2 - k_y^2}} w e^{-j\sqrt{\frac{\omega^2}{c^2} - k_x^2 - k_y^2}} \tag{2.46b}$$

$$w = \left(C_x e^{-jk_x x} + D_x e^{jk_x x}\right)\left(C_y e^{-jk_z z} + D_z e^{jk_z}\right) \tag{2.46c}$$

This shows that the radiated waves are plane waves, which can be evanescent or progressive depending on k_z. The amount of power radiated by a portion S of the plate is

$$\pi_r^{1,2}(S) = \frac{1}{2}\int_S \mathrm{Re}\left\{ p_{1,2}|_{z=0}\, w^* \right\} dS \tag{2.47}$$

and then using equations (2.46)

$$\pi_r^{1,2}(S) = \frac{1}{2}\omega^2 \rho c \mathrm{Re}\left\{ \frac{k}{\sqrt{k^2 - k_x^2 - k_y^2}} \right\} \int_S |w|^2 \, dS. \tag{2.48}$$

Then the quadratic velocity of a generic portion S of the plate can be introduced as

$$< v^2 >= \frac{1}{2}\omega^2 \int_S |w|^2 \, dS, \tag{2.49}$$

and the expression of the radiated power is

$$\pi_r(S) = \rho c \mathrm{Re}\left\{ \frac{k}{\sqrt{k^2 - k_x^2 - k_y^2}} \right\} < v^2 > . \tag{2.50}$$

From the last equation, the radiation coefficient can be defined as

$$\sigma_r = \left| \frac{\pi_r(S)}{\rho c < v^2 >} \right| = \mathrm{Re}\left\{ \frac{k}{\sqrt{k^2 - k_x^2 - k_y^2}} \right\} = \mathrm{Re}\left\{ \frac{k}{k_z} \right\} \tag{2.51}$$

Remark 4. *Being k always real there is radiated power only if k_z, that is for progressive waves. Evanescent waves does not radiate.*

In order to clarify these concepts, the case study of an aluminium plate is considered.

The case an aluminium plate

Introducing the trace wave-number of the waves propagating into a plate coupled with fluids as

$$k_f = \sqrt{k_x^2 + k_y^2}, \tag{2.52}$$

equation (2.45) can be rewritten as

$$Dk_f^4 - m\omega^2 + 2\frac{j\omega^2}{\sqrt{k^2 - k_f^2}} = 0. \tag{2.53}$$

In order to study this dispersion relation a new parameter a is introduced:

$$a = \sqrt{k_f^2 - k^2} = jk_z, \tag{2.54a}$$

$$k_f = \sqrt{a^2 + k^2}. \tag{2.54b}$$

The parameter a that is then related to the propagation of the waves along the z direction. Substituting into the dispersive relation

$$a^5 + 2k^2a^3 + \left(k^4 - k_F^4\right)a - 2\frac{\rho_f}{m_1} = 0, \tag{2.55}$$

where $k_F^4 = \rho\omega^2/D$ is the trace wave-number of the plate "in vacuo", a polynomial equation for a it is obtained. From equations (2.38b) and (2.38b) and considering the parameter a the value of the pressure fields can be found

$$p_1 = \frac{\omega\rho_f ck}{a}e^{az} \tag{2.56}$$

$$p_2 = -\frac{\omega\rho_f ck}{a}e^{-az} \tag{2.57}$$

So the being

$$\pi_r(S) = \frac{1}{2}\int_S \mathrm{Re}\left\{p_1|_{z=0}\, w^*\right\} dS \tag{2.58}$$

the amount of power radiated by a portion S of the plate in the halfspace $z > 0$, the expression in function of a is

$$\pi_r(S) = \frac{1}{2}\omega^2\rho c\mathrm{Re}\left\{\frac{jk}{a}\right\}\int_S |w|^2\, dS. \tag{2.59}$$

The quadratic velocity of the portion of the plate can be introduced as

$$< v^2 >= \frac{1}{2}\omega^2\int_S |w|^2\, dS. \tag{2.60}$$

then

$$\pi_r(S) = \rho c\mathrm{Re}\left\{\frac{jk}{a}\right\} < v^2 > \tag{2.61}$$

is the expression of the radiated power. The radiation coefficient can be introduced as

$$\sigma_r = \left|\frac{\pi_r(S)}{\rho c < v^2 >}\right| = \mathrm{Re}\left\{\frac{jk}{a}\right\} = k\mathrm{Im}\left\{\frac{1}{a}\right\} \tag{2.62}$$

that depends mainly on a. It is useful to study the dispersion relation (2.55) in order to analyse the radiation coefficient. Introducing the light fluid approximation, $\rho \ll m_1$, and neglecting the trivial solution $a = 0$, the equation (2.55) becomes

$$a^4 + 2k^2a^2 + k^4 - k_F^4 = 0, \tag{2.63}$$

and its solutions are

$$a_{1,2} = \pm j\sqrt{k^2 - k_F^2}, \tag{2.64}$$

$$a_{3,4} = \pm\sqrt{k_F^2 - k^2}. \tag{2.65}$$

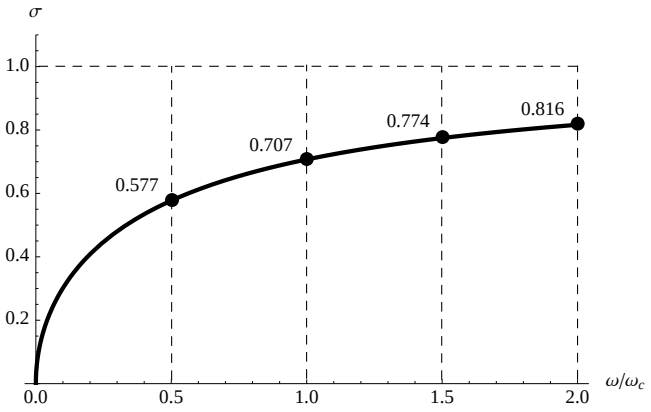

Figure 2.5: Radiation coefficient for an evanescent flexural wave

Negative solutions, that correspond to waves travelling towards the plate, will not be considered because of the Sommerfeld condition. The remaining solutions are:

$$a_1 = j\sqrt{k^2 - k_F^2}, \tag{2.66a}$$

$$a_3 = \sqrt{k_F^2 - k^2}. \tag{2.66b}$$

From equation (2.54b) we deduce the following relationship between these solutions and the wave-number k_f:

$$a_1 \longrightarrow k_f = jk_F, \tag{2.67}$$

$$a_3 \longrightarrow k_f = k_F. \tag{2.68}$$

Analysis of the first solution, evanescent flexural wave ($k_f = jk_F$)
The corresponding radiation coefficient is

$$\sigma_1 = \frac{1}{\sqrt{1 + \left(\frac{k_F}{k}\right)^2}} \tag{2.69}$$

$$\sigma_1 = \frac{1}{\sqrt{1 + \left(\frac{\omega_c}{\omega}\right)}} \tag{2.70}$$

Where

$$\omega_c = c^2\sqrt{\frac{m_1}{D}} \tag{2.71}$$

The frequency behaviour of the radiation coefficient σ_1 for an evanescent flexural wave is plotted in figure 2.5. Evanescent flexural waves always radiate, but the radiation efficiency increase with the frequency and tends to be equal to one.

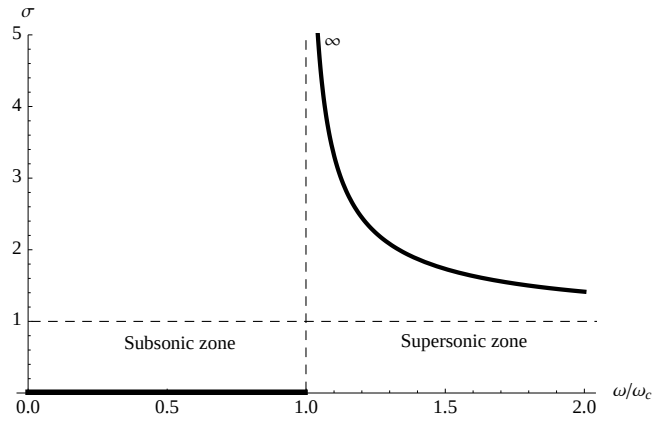

Figure 2.6: Radiation coefficient for a progressive flexural wave

Analysis of the second solution, progressive flexural wave $k_f = k_F$
The corresponding radiation coefficient is

$$\sigma_3 = \frac{1}{\sqrt{1 - \left(\frac{k_F}{k}\right)^2}} \tag{2.72}$$

$$\sigma_3 = \frac{1}{\sqrt{1 + \left(\frac{\omega_c}{\omega}\right)}} \tag{2.73}$$

The frequency behaviour of the radiation coefficient σ_3 for an evanescent flexural wave is plotted in figure 2.6. Progressive flexural waves radiate only for $\omega > \omega_c$. Above ω_c the radiation coefficient is always greater than one. This because for $\omega < \omega_c$ the acoustic wave is evanescent, for $\omega > \omega_c$ is progressive.

2.3.3 Transmission properties of single plate structures

Considering the same geometry as in the previous section, this time the system is excited by a plane waves with the angles of incidence θ and ϕ defined as in figure 2.7.

$$p_{inc} = e^{-jk\sin\theta\sin\phi x - jk\sin\theta\cos\phi y - jk_z z} \tag{2.74}$$

For the sake of simplicity and without losing generality the incident wave can be chosen with $\phi = 0$.

$$p_{inc} = e^{-jk_x x - jk_z z} \tag{2.75}$$

where

$$k_x = k\sin\theta, \quad k_y = 0, \quad k_z = k\cos\theta, \tag{2.76}$$

This implies that the wavenumber of the transmitted wave is always real, and the transmitted wave is always progressive. This result come from the choice

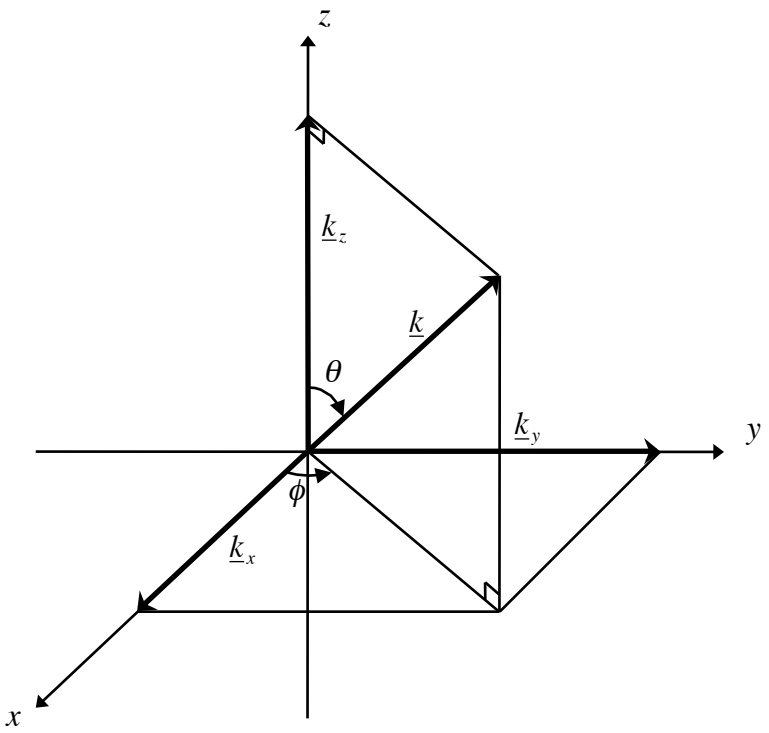

Figure 2.7: Radiation coefficient for a progressive flexural wave

of using identical fluids.

$$p_1 = e^{-jk_x x}\Big(\underbrace{e^{-jk_z z}}_{\text{Incident wave}} + \underbrace{B_z^1 e^{jk_z z}}_{\text{Reflected wave}} \Big) \tag{2.77a}$$

$$p_2 = \underbrace{A_x^2 e^{-jk_x x}\left(A_z^2 e^{-jk_z z}\right)}_{\text{Transmitted wave}} \tag{2.77b}$$

$$w_1 = C_1 e^{-jk_x x} \tag{2.77c}$$

Using these solutions in equations (2.38b), (2.39b), and (2.40) it is easy to obtain the value of the constant C_1, that is the modulus of the bending waves.

$$C_1 = \frac{2}{Z_{pl} + j2\omega\dfrac{\rho c}{\cos\theta}} \tag{2.78}$$

Introducing the transparence function as the ratio between the power radiated form the plate and that of the incident wave

$$\tau = \frac{\pi_{rad}}{\pi_{inc}}. \tag{2.79}$$

where

$$\pi_{inc} = \frac{1}{2}\int_S \mathrm{Re}\left\{ p_{inc}|_{z=0} \left(\left.\frac{\partial p_{inc}}{\partial z}\right|_{z=0} \frac{1}{j\omega\rho} \right)^* \right\} \mathrm{d}S = \frac{1}{2}\frac{\cos\theta}{\rho c} S \tag{2.80}$$

The value of the transparency is then

$$\pi_{rad} = \frac{1}{2}\int_S \mathrm{Re}\left\{ p_{inc}|_{z=0} \left(j\omega w\right)^* \right\} \mathrm{d}S = \frac{1}{2}\frac{\rho c\omega^2}{\cos\theta} S|C_1|^2 \tag{2.81}$$

$$\tau(\theta,\omega) = \frac{\omega^2\rho^2c^2}{\cos\theta^2}|C_1|^2. \tag{2.82}$$

and using equation (2.78)

$$\tau(\theta,\omega) = \frac{\omega^2\rho^2c^2}{\cos\theta^2}\frac{4}{\left|Z_{pl} + j2\omega\dfrac{\rho c}{\cos\theta}\right|^2}. \tag{2.83}$$

A standard parameter used in structural acoustics for verifying the performances of structures is the Sound Reduction Index, defined as follows:

$$SRI(\theta,\omega) = 10\log_{10}\left(\frac{1}{\tau(\theta,\omega)}\right) \tag{2.84}$$

Sound transmission through an aluminium plate

The trivial case of an aluminium plate is discussed in this section.
Since for an aluminium plate $Z_{pl} = Dk_x^4 - m\omega^2$ the transparency is

$$\tau(\theta,\omega) = \tau(\theta,\omega) = \frac{\omega^2\rho^2c^2}{\cos\theta^2}\frac{4}{\left|Dk_x^4 - m\omega^2 + j2\omega\dfrac{\rho c}{\cos\theta}\right|^2}. \tag{2.85}$$

From the decomposition of the scalar wavenumbers, equation (2.76), it is known that

$$k_x = k\sin\theta = \frac{\omega}{c}\sin\theta$$

then introducing the *coincidence frequency* as

$$\omega_{coin}(\theta) = \frac{c^2}{\sin^2\theta}\sqrt{\frac{m}{D}} \tag{2.86}$$

and performing some easy calculations the expression of the transparency is

$$\tau(\theta,\omega) = \frac{1}{\left(\dfrac{\omega m\cos\theta}{\rho c}\right)^2\left(1 - \dfrac{\omega^2}{\omega_{coin}^2}\right)^2 + 1}. \tag{2.87}$$

It is easy to verify that at ω_{coin} the transparency is equal to one. This means that for $\omega = \omega_{coin}$ the plate il completely transparent.

Remark 5. *Since ω_{coin} is a function of the angle of incidence plane waves with a different angle of incidence have different ω_{coin}. Since $\omega_{coin}(\pi/2) = \omega_c$ there will be no total transparency below the critical frequency.*

Let us set a specific angle θ_0, the analysis can now be performed concentrating it in three distinct ranges of frequencies.

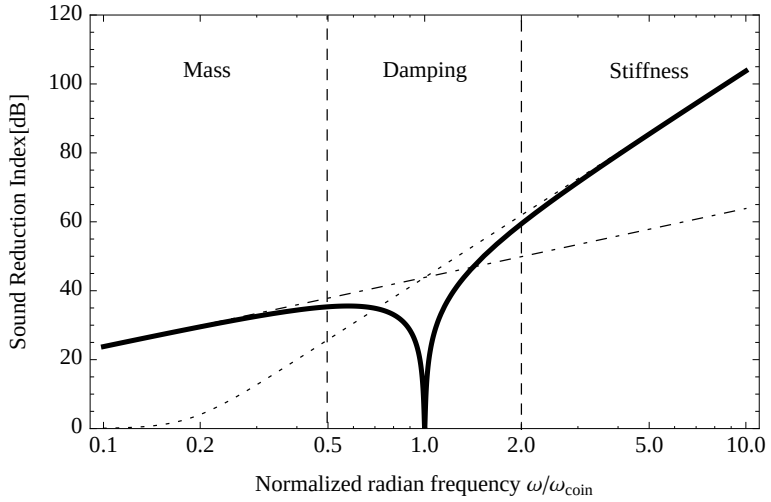

Figure 2.8: Sound Reduction Index for a specific incidence angle.

The region of the mass ($\omega < \omega_{coin}$) Since the term ω^2/ω_{coin}^2 can be neglected the transparency becomes

$$\tilde{\tau}(\theta,\omega) = \frac{1}{\left(\omega^2 \frac{m\cos\theta}{\rho c}\right)^2 + 1}. \tag{2.88}$$

Then the sound reduction index is

$$S\tilde{R}I(\theta,\omega) = 10\log\left(\omega^2\left(\frac{m\cos\theta}{\rho c}\right)^2 + 1\right). \tag{2.89}$$

It is clear from the last equation that the slope is fixed to $6dB$/Octave, then supposing the parameters of the fluid fixed the only parameter which can raise the value of sound reduction in this range of frequency is the surface mass density of the plate, that is why this region is called *region of the mass*. A plot of the Sound Reduction Index with different mass values is in figure 2.9(a).

The region of the stiffness ($\omega > \omega_{coin}$)**:** The term ω^2/ω_{coin}^2 becomes dominant and the transparency becomes

$$\tilde{\tau}(\theta,\omega) = \frac{1}{\omega^4\left(\frac{\sin^2\theta\cos\theta}{D\rho c^2}\right)^2}. \tag{2.90}$$

Then the sound reduction index is

$$S\tilde{R}I(\theta,\omega) = 10\log\left(\omega^4\left(\frac{\sin\theta\cos\theta}{D\rho c^2}\right)^2\right). \tag{2.91}$$

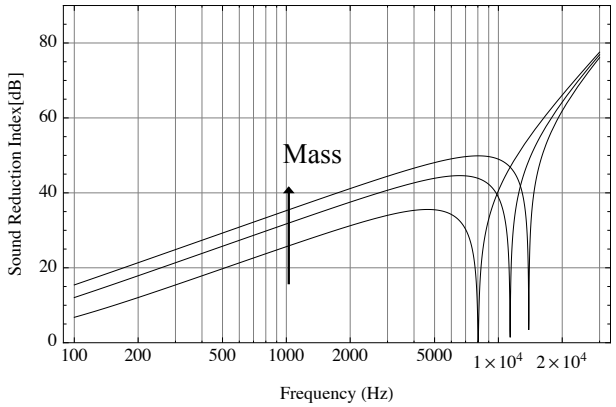

(a) Increasing Mass

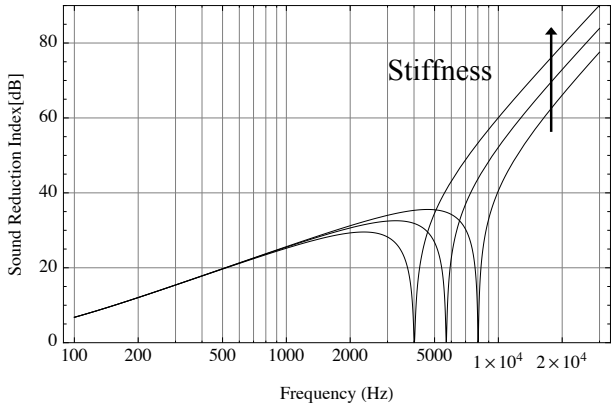

(b) Increasing Stiffness

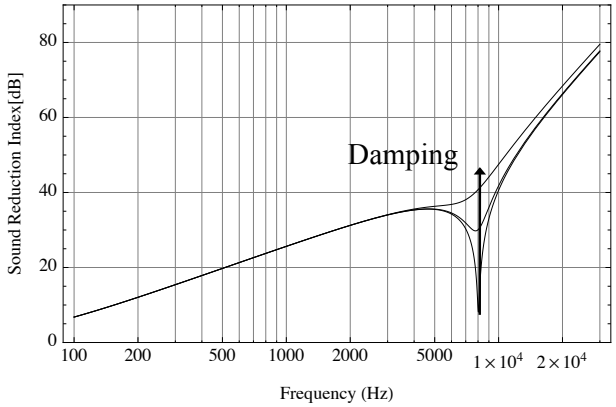

(c) Increasing Damping

Figure 2.9: Sound Reduction index in function of mass, stiffness and damping

This region is called *region of the stiffness* since the acoustic behaviour of the structure in this range of frequencies can be influenced only changing the value of the stiffness D, as before was for the region of the mass. A plot of the Sound Reduction Index with different stiffness values is in figure 2.9(b).

The coincidence region ($\omega = \omega_{coin}$) In order to better investigate the behaviour near this region we need to introduce a structural damping in the plate equation.
The simplest structural damping modelling for an isotropic plate is done by introducing a complex Young Modulus $Y^* = Y(1 + j\zeta)$.
Hence the impedance of the plate becomes:

$$Z_{pl} = Dk_x^4 - m\omega^2 + j\zeta Dk_x^4,$$

were ζ is the structural damping coefficient.

$$\tau(\theta, \omega) = \frac{1}{\left(\frac{\omega m \cos\theta}{\rho c}\right)^2 \left(1 - \frac{\omega^2}{\omega_{coin}^2}\right)^2 + \left(\zeta \frac{\cos^2\theta}{2\rho c} \frac{\omega^2}{\omega_{coin}^2} + 1\right)}. \tag{2.92}$$

Then the value of the transparency at the coincidence frequency becomes

$$\tau(\theta, \omega_{coin}) = \frac{1}{\left(\frac{\zeta \cos^2\theta}{2\rho c} + 1\right)}. \tag{2.93}$$

Remark 6. *The coincidence region is the only one in which the value of the Sound Reduction Index depends on the damping.*

A plot of the Sound Reduction Index with different values of the damping parameter is in figure 2.9(c).

3D Plots and Contour Plots Since the value of the SRI depends not only on frequency, but also on the angle of incidence two clearer way to plot this quantity is here introduced. The first one is the 3D plot of the SRI as in figure 2.10(a), where the trend of the ω_{coin} can be easily identified. Plots like those in figure 2.8 are to be seen as slices of the 3D plot for a specific θ. Similarly the contour plot in figure 2.10(b) shows the same results in 2D. These two way of representing the SRI are very useful in order to compare the behaviour of different sound transmission control strategies.

2.3.4 Double plate structures

In this section systems composed by two parallel infinite plates are considered, as sketched in figure 2.11. As already done in section 2.3.2 the equation for pressure and flexural waves can be written in frequency domain in this way

Fluid 1 ($z < 0$)

$$\nabla^2 p_1 + \frac{\omega^2}{c^2} p_1 = 0 \tag{2.94a}$$

$$\left.\frac{\partial p_1}{\partial z}\right|_{z=0} = \rho\omega^2 w_1 \tag{2.94b}$$

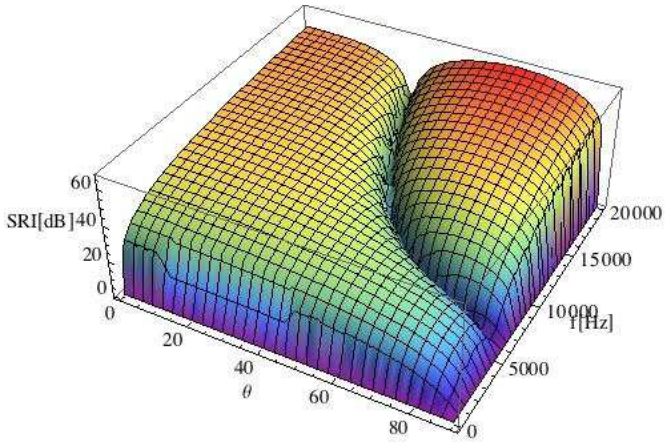

(a) 3DPlot

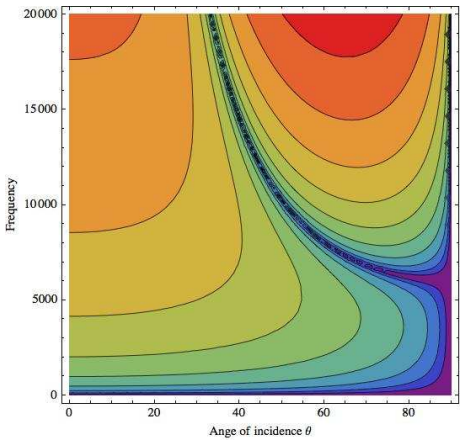

(b) ContourPlot

Figure 2.10: Contour Plot and 3D Plot of the Sound Reduction Index in function of θ.

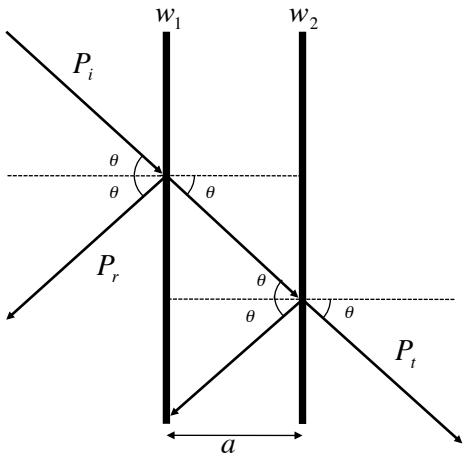

Figure 2.11: Infinite double plates

Fluid 2 $(0 < z < a)$

$$\nabla^2 p_2 - \frac{\omega^2}{c^2} p_2 = 0 \tag{2.95a}$$

$$\left.\frac{\partial p_2}{\partial z}\right|_{z=0} = \rho\omega^2 w_1 \tag{2.95b}$$

$$\left.\frac{\partial p_2}{\partial z}\right|_{z=a} = \rho\omega^2 w_2 \tag{2.95c}$$

Fluid 3 $(z > a)$

$$\nabla^2 p_3 + \frac{\omega^2}{c^2} p_3 = 0 \tag{2.96a}$$

$$\left.\frac{\partial p_3}{\partial z}\right|_{z=a} = \rho\omega^2 w_2 \tag{2.96b}$$

Sommerfeld condition at infinity

Plate 1

$$\mathcal{L}_1\{w_1, w_2\} = (p_1 - p_2)_{z=0} \tag{2.97}$$

Plate 2

$$\mathcal{L}_2\{w_1, w_2\} = (p_2 - p_3)_{z=a} \tag{2.98}$$

where $\mathcal{L}\{w_1, w_2\}$ is the generic linear differential operator of the plate. The generic solutions for the propagation equations supposing an incident wave in this form

$$p_{inc}(x, y, z) = e^{-jk(sin\theta)y - jk(cos\theta)z} \tag{2.99}$$

are written in this form

$$p_1(x, y, z) = e^{-jk(sin\theta)y}\left(e^{-jk(cos\theta)z} + B_z^1 e^{+jk(cos\theta)z}\right) \tag{2.100a}$$

$$p_2(x, y, z) = e^{-jk(sin\theta)y}\left(A_z^2 e^{-jk(cos\theta)z} + B_z^2 e^{+jk(cos\theta)z}\right) \tag{2.100b}$$

$$p_3(x, y, z) = e^{-jk(sin\theta)y}\left(A_z^3 e^{-jk(cos\theta)z}\right) \tag{2.100c}$$

$$w_1(x, y) = C_1 e^{-jk(sin\theta\, cos\phi)y} \tag{2.100d}$$

$$w_2(x, y) = C_2 e^{-jk(sin\theta\, cos\phi)y} \tag{2.100e}$$

2.3.4.1 The case of two aluminium plates

In this section a structure composed by two infinite thin aluminium plates immersed in air is considered. Substituting the solutions (2.100) into equations (2.94), (2.95), (2.96), (2.97), (2.98) the following system, written in matrix

form, is obtained:

$$\begin{bmatrix} jkcos\theta & 0 & 0 & 0 & -\rho\omega^2 & 0 \\ 0 & -jkcos\theta & jkcos\theta & 0 & -\rho\omega^2 & 0 \\ 0 & -jkcos\theta e^{-jkcos\theta a} & jkcos\theta e^{jkcos\theta a} & 0 & 0 & -\rho\omega^2 \\ 0 & 0 & 0 & -jkcos\theta e^{-jkcos\theta a} & 0 & -\rho\omega^2 \\ 1 & -1 & -1 & 0 & -Z_1 & 0 \\ 0 & -e^{-jkcos\theta a} & e^{jkcos\theta a} & e^{jkcos\theta a} & 0 & -Z_2 \end{bmatrix} \times$$

$$\times \begin{bmatrix} B_z^1 \\ A_z^2 \\ B_z^2 \\ A_z^3 \\ C_1 \\ C_2 \end{bmatrix} = \begin{bmatrix} jkcos\theta \\ 0 \\ 0 \\ 0 \\ 0 \\ -1 \\ 0 \end{bmatrix}$$

Then the expression of the amplitude coefficients of the waves is

$$A_z^3 = j\omega \frac{\rho c}{\cos\theta e^{-jk\cos\theta a}} \quad (2.101a)$$

$$B_z^1 = 1 + j\omega \frac{\rho c}{\cos\theta} C_1 \quad (2.101b)$$

$$A_z^2 = B_z^2 + j\omega \frac{\rho c}{\cos\theta} C_2 \quad (2.101c)$$

$$B_z^2 = \left(\frac{\omega\rho c \cot(k\cos\theta a)}{2\cos\theta} - j\frac{\omega\rho c}{2\cos\theta} \right) C_1 - \frac{\rho\omega c}{2\cos\theta \sin(k\cos\theta a)} C_2 \quad (2.101d)$$

A compact form for writing the impedance of a double plate is the following

$$\begin{bmatrix} Z_{11} & -Z_{12} \\ -Z_{12} & Z_{22} \end{bmatrix} \begin{bmatrix} C_1 \\ C_2 \end{bmatrix} = \begin{bmatrix} 2 \\ 0 \end{bmatrix} \quad (2.102)$$

where

$$Z_{11} = Z_1 + j\omega \frac{\rho c}{\cos\theta} + \frac{\omega\rho c}{\cos\theta} \cot(kcos\theta a) \quad (2.103a)$$

$$Z_{22} = Z_1 + j\omega \frac{\rho c}{\cos\theta} + \frac{\omega\rho c}{\cos\theta} \cot(kcos\theta a) \quad (2.103b)$$

$$Z_{12} = \frac{\omega\rho c}{\cos\theta \sin(k\cos\theta a)} \quad (2.103c)$$

Then incident and radiated power are

$$\pi_{inc} = \int_S \frac{1}{2} Re \left\{ p_{inc}(x,y,0) \left(\frac{\partial}{\partial z} p_{inc}(x,y,0) \frac{1}{j\omega\rho} \right)^* \right\} dS = \frac{1}{2} \frac{\cos\theta}{\rho c} S \quad (2.104a)$$

$$\pi_{rad} = \int_S \frac{1}{2} Re \left\{ p_2(x,y,0) \left(j\omega w_2(x,y) \right)^* \right\} dS = \frac{\omega^2 \rho c}{2\cos\theta} |C_2|^2 S \quad (2.104b)$$

and following the definition the transparency coefficient is

$$\tau(\omega,\theta) = \frac{\omega^2\rho^2c^2}{\cos^2\theta}|C_2|^2 \tag{2.105}$$

Using system (2.102)

$$C_2 = \frac{2Z_{12}}{Z_{11}Z_{22} - Z_{12}^2}$$

the final expression for the transparency is

$$\tau(\omega,\theta) = 4\omega^2\left(\frac{\rho c}{\cos\theta}\right)^2 \frac{|Z_{12}|^2}{|Z_{11}Z_{22} - Z_{12}^2|^2} \tag{2.106}$$

As already done in section 2.3.2 the analysis will be performed for different ranges of frequency

Low frequency, the "mass-air-mass" pseudo-resonance

The low frequency region can be defined with the following conditions:

$$\omega \ll c\frac{\pi}{2}\frac{1}{\cos\theta a}, \tag{2.107a}$$

$$\omega \ll \omega_{coin}^{(1)}, \tag{2.107b}$$

$$\omega \ll \omega_{coin}^{(2)}. \tag{2.107c}$$

In this region it is possible to perform the following simplifications:

$$\cot(k\cos\theta e) \backsimeq \frac{1}{k\cos\theta a}, \tag{2.108a}$$

$$\sin(k\cos\theta e) \backsimeq k\cos\theta a, \tag{2.108b}$$

$$Z_1 \backsimeq -\omega^2 m_1, \tag{2.108c}$$

$$Z_2 \backsimeq -\omega^2 m_2 \tag{2.108d}$$

where m_1 and m_2 are the mass densities of each plate. This means neglecting

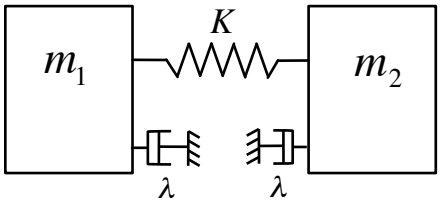

Figure 2.12: Mass-spring-mass of the double plate

the stiffness of the plates, and considering the structure as a two degrees of freedom system, as in figure 2.12 where the parameters are

$$K = \frac{\rho c^2}{a\cos^2\theta} \tag{2.109a}$$

$$\lambda = \frac{\rho c}{\cos\theta} \tag{2.109b}$$

$$\omega_R = \sqrt{K\frac{m_1 + m_2}{m_1 m_2}} \tag{2.109c}$$

These parameters are obtained considering that

$$Z_{11} = -\omega^2 m_1 + j\omega \underbrace{\frac{\rho c}{\cos\theta}}_{\lambda} + \underbrace{\frac{\rho c^2}{a\cos^2\theta}}_{K}, \tag{2.110a}$$

$$Z_{22} = -\omega^2 m_2 + j\omega \underbrace{\frac{\rho c}{\cos\theta}}_{\lambda} + \underbrace{\frac{\rho c^2}{a\cos^2\theta}}_{K}, \tag{2.110b}$$

$$Z_{12} = \underbrace{\frac{\rho c^2}{a\cos^2\theta}}_{\lambda}, \tag{2.110c}$$

The value for the approximated value of the transparency function at low frequency is then:

$$\tau(\omega,\theta) = \frac{4\omega^2\lambda^2K^2}{\left[m_1m_2\omega^2\left(\omega^2-\omega_R^2\right)+\lambda^2\omega^2\right]^2+\left[\omega\left(2\lambda K-\omega^2\left(m_1+m_2\lambda\right)\right)\right]^2} \tag{2.111}$$

The coincidence region

As for a single plate there is a frequency ω_{coin} for which each single plate becomes completely transparent. In this case , since there are two plates, it is crucial to make them have different ω_{coin}. This can be easily done choosing different values for the thickness.

The stationary waves phenomenon

When the condition

$$k\cos\theta a = n\pi, \tag{2.112}$$

that means when the wave vector in the x direction matches the distances between the plates, stationary waves are excited. This occurs at When the condition

$$\omega_{st}^n = n\frac{c}{\cos\theta a}\pi, \tag{2.113}$$

and the value of the transparency is

$$\tau(\omega,\theta) = (\omega_{st}^n)^2\left(\frac{\rho c}{\cos\theta}\right)\frac{4}{\left|Z_1+Z_2+2j\frac{\rho c}{\cos\theta}\omega_{st}^n\right|^2} \tag{2.114}$$

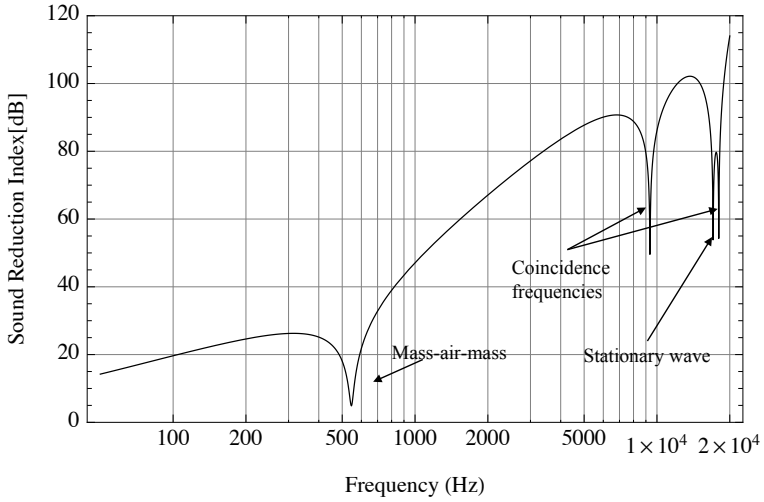

Figure 2.13: SRI for a double aluminium plate calculated at $\pi/3$

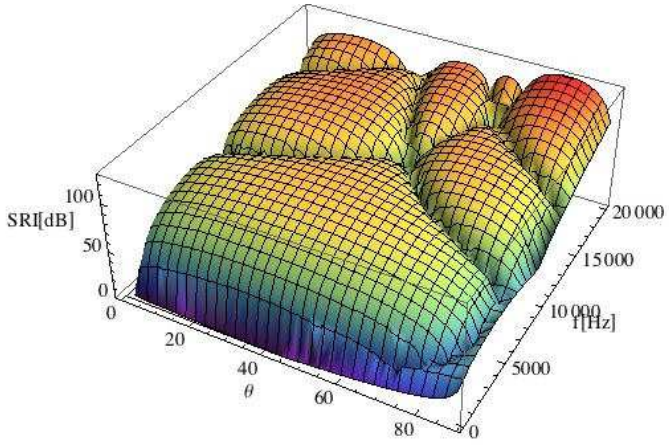

(a) 3DPlot

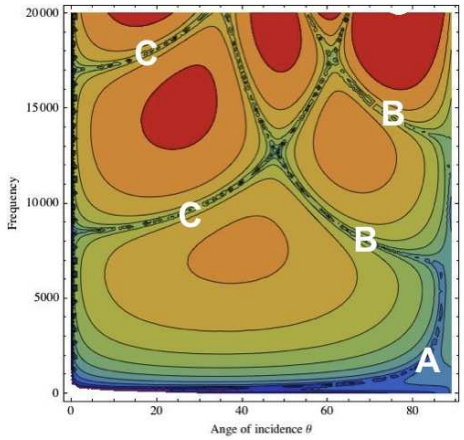

(b) ContourPlot

Figure 2.14: Contour Plot and 3D Plot of the Sound Reduction Index in function of θ.

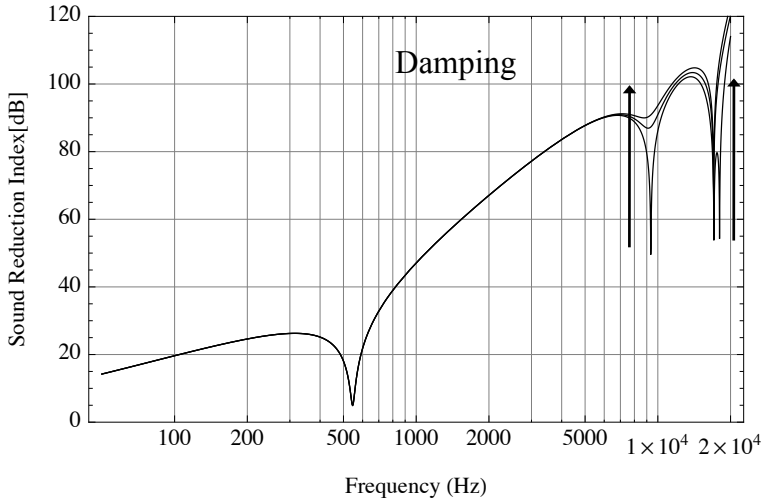

Figure 2.15: SRI for a double aluminium plate calculated at $\pi/3$

In figure 2.13 the SRI of a double aluminium plate is plotted. From figure 2.14(b) it is possible to remark the trend of the Mass-air-mass pseudo-resonance (Curve A), of the two coincidence frequencies of the plates (Curve B) and of the first two stationary frequencies (Curve C).
When considering the effects of the parameters variations, the behaviour of a double plate reflects that of a single plate system, except for the presence of more parameters, as the distance of the plates or the relative mass and stiffness, which influence the positioning of the pseudo-resonances. With respect to damping, the effects on the SRI are concentrated at the coincidence frequencies, as shown in figure 2.15

2.3.5 Comparison between single and double plate structures

As seen in sections 2.3.3 and 2.3.4, single plate system and double plate system have a different behaviour.
The differences can be easily found by analysing figures 2.8 and 2.13, where the structures are both undamped. The mean slope of the SRI of a double plate system is higher, as the value od the SRI at the coincidence frequency, than for a single plate. This means that a double plate system performs better, in terms of overall properties. But on the other hand, a double wall structure introduces pseudo-resonances, due to the coupling phenomenons between the two plates and the inner fluid. It is also important to remark that the double wall structure here presented does not have any connection between the two plates, which is needed for evident structural requirements. Adding structural connections between the two walls results in a mixed behaviour between a single plate structure, at low frequency, and a double plate structure at high frequency. This means that in order to

fully exploit the potential of a double wall structure a specific optimization procedure is needed, since the involved parameters are manifold, a explained in [Oniszczuk 2004]. For this reasons, and considering that the proposed control strategies are always based on damping, the rest of the work the study is then concentrated on single plate structures. This does not prevent us to extend in the future the proposed works to double plate structures.

2.4 Hearing and sound perception

While the physical characteristics of a sound field can be measured with precision by standard acoustic instruments (microphones, filters, spectrum analysers, etc.), the interpretative characteristics of hearing are expressible in terms of subjective parameters that lead to statistical predictions of the judgement of an average listener under assumed or known conditions [Kuttruff 2007, Kinsler 2000]. For example, judgements of the relative loudness of two sounds of different frequencies allow relating the subjective loudness to the physical parameters of intensity and frequency. The threshold of audibility and free field, equal loudness level contours for pure tones with subject facing the source are plotted in figure 2.16.

These kind of experiments often suffer from uncertainty, and it is difficult to

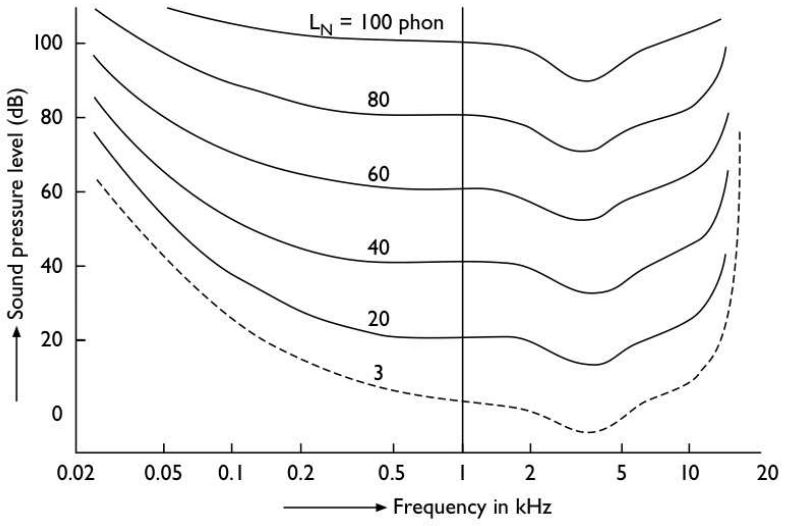

Figure 2.16: Threshold of audibility and free field, equal loudness level contours [Kuttruff 2007].

find an exact analytical representation od the sensitivity curve of the human ear. In the literature there exist different kind of weightings. The curve that will be used as reference in this work is the A-weighting, $A(f)$ and it is defined

using the auxiliary function $R_A(f)$

$$R_A(f) = \frac{12200^2 f^4}{(f^2 + 20.6^2)(f^2 + 12200^2)\sqrt{(f^2 + 107.7^2)(f^2 + 737.9^2)}} \tag{2.115}$$

as

$$A(f) = A_{\text{off}} + 20\log(R_A(f)) \tag{2.116}$$

where the offset A_{off} can be used for obtaining a value of $0dB$ at a certain frequency.

This weighting will be used in the following sections for the optimization of the controller with respect to the human hearing characteristics.

Chapter 3

Modelling a localized piezoelectric smart plate

Contents

Object of the Chapter

The object of the chapter is the modelling and optimization process of a smart plate, with the aim of controlling the radiated sound power. The structure here considered is a thin metal plate with a set of piezoelectric transducers. The goal is to derive an optimal passive circuit topology which permits to efficiently reduce the radiated sound power.
Several types of passive piezoelectric networks will be analysed and compared, and a novel procedure for optimizing the piezoelectric transducer positioning is presented. The entire modelling and optimization procedure is then applied to the classical case study of a simply supported plate. These concepts will be used in the experimental tests described in Chapter 5

3.1 Introduction and literature review

The aim of this chapter is the modelling and the optimization of a smart plate that uses localized[1] piezoelectric transducers for the reduction of the radiated sound power. To this end an aluminium plate equipped with a set of optimally placed patches connected to a passive circuit is considered.
The difficulties in designing a smart structure are not only related to the conception of the electric circuit used as controller, but also in choosing how the circuit itself is coupled with the structure. The choice of the number of transducers to be used, and their positioning, is a crucial step in the designing process. In this chapter the entire design process of a smart structure is proposed, with the objective of obtaining the best efficiency in terms of reduction of radiated sound power. To this end classical instruments of the vibrational mechanics are used together with acoustic concepts, as the modal radiation efficiency introduced in Chapter 2. The introduction of this acoustic characterization of the structure in the optimization process, is done by using a new cost function, the Acoustic Controllability, for the optimization of the transducers positioning.

Section 3.2 is devoted to a detailed description of the modelling process. The equations of motion will be derived by using a variational method based on the virtual work principle and finally a modal model of the structure is derived.
The object of section 3.3 is a survey of several passive multi-modal control circuits. The optimization procedure for each of these circuits is shown.
Section 3.4 is dedicated to optimization of the piezoelectric transducer placement, with the aim of efficiently reduce the radiated sound power. In this section a novel cost function for the optimization, the acoustic controllability, is introduced.
In section 4.4.2 the entire design process is applied to the case study of a simply supported aluminium plate, and some numerical simulations are shown.

3.1.1 Literature review

In the literature there exists lots of examples of control techniques based on using localized piezoelectric transducers, aimed to the control of structural vibrations. Some of them are appropriate for being used in acoustics, some are not.
When choosing suitable circuits for sound radiation control, some essential requirements must be fulfilled:

[1]Localized means placed in particular optimized positions, used in counter position to distributed.

- The control must be capable of controlling multiple modes over a large band, and to concentrate the control effort over some selected modes.
- The controller itself must not generate noise.

These consideratons lead to the choice of linear resonating circuit, over non linear circuits, as the commutation shunts [Ducarne 2009, Thomas 2009].

One of the first paper that introduces passive linear shunt for piezoelectric material with the aim of damping vibrations is [Hagood 1991]. This is an adaptation of Den Hartog's damped vibration absorber for two degrees of freedom systems [Den Hartog 1956].

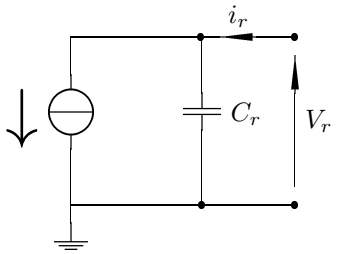

Figure 3.1: Equivalent circuit for a piezoelectric transducer.

The idea behind this control technique is very simple: since a piezoelectric patch can be modelled as variable current generator in parallel with a capacitance, figure 3.1, shunting the transducer with a RL circuit will forms a resonant circuit. When considering a single vibration mode at frequency ω_i, and if the electric resonator is also tuned at the same frequency, the energy flux between the two systems is optimized for a selected value of the resistance R. Some optimization techniques used for determining the optimal circuit parameters are the same used for a two degrees of freedom mechanical system, as presented in [Hagood 1991, Ozer 2003, Caruso 2001].
The main problems of using a single RL shunt the following:

- each patch can control only one mode,
- large values for the inductances are needed,
- the performances of the system strongly depend on the electromechanical coupling.

To overcome the first problem, a generalized version of this control circuit is easily obtained using multiple shunted piezoelectric actuators, one for each target mode. However, since the shunts act independently, a single mode does not take advantage of the presence of the other actuators. For that reason several improvements has been made to this first model, in order to ameliorate the performances and introduce multi-modal damping. Some works also concentrates in the reduction of inductance requirements [Fleming 2003].

In [Behrens 2003] the current flowing shunt is introduced. This circuit is composed by several RL circuits tuned to different modes, shunted to the same patch. A filter is added on each branch to permit the current flow only for a selected frequency. In this way, multiple RL shunts can be used on one patch. Another advantage of this topology is that using multiple patches and replicating the circuit, the damping of each mode increases with the number of patches. The main drawback is that adding a capacitance in the shunt decreases the electromechanical coupling, and consequently the damping capability of the controller. Furthermore when using multiple patches the fact that the shunts are independent does not permit to take advantage of the spatial distribution of the transducers.

A circuit that adds multi-modal control and that exploits the spatial distribution of the patches is presented in [Giorgio 2009]. The system is optimized for using one patch for each mode, but since the proposed topology uses an optimized RL network, the energy flux is optimized thanks to the communication between the transducers. The main drawback of this control topology is the need of a simulated circuitry, being the components values too high, or even negative, and then not suitable for a passive realization.

The optimization procedure for determining the optimal positioning of the transducers for passive vibration control is presented in different works, among the others [Halim 2003, Moheimani 1999]. These procedures are all based on vibration control optimization, and not on sound radiation control. An acoustic based optimization of the circuit parameter, but not of the positioning, is presented in [Ozer 2003], considering also the hysteresis of the piezoelectric materials.

3.1.2 Objectives

From the analysis of the literature these main statement are evinced:

- There exists several passive control techniques that are used for vibration control, which can be efficiently used for reducing radiated sound power.
- There does not exists an optimization procedure for placing piezoelectric co-located transducers that directly involves the radiation properties of the structure in the cost function.

Theen the objectives of the chapter are the following:

- Find a model for the smart structure
- Find a suitable passive circuit for sound radiation control
- Introduce a novel cost function for optimizing the transducer positioning for sound radiation control

3.2 Smart Plate modelling

This section is about the modelling process of a smart plate. The objective is the derivation of a modal model for the structure, that will be used as a starting point for the optimization of the circuit. This is done following and adapting the results present in the literature [Benjeddou 2002, Carrera 2007, Fernandes 2002, Sze 004, Teresi 1997, Trindade 2008, Hurlebaus 2006].

3.2.1 Geometry

Let us consider a plate of dimensions $a \times b$ where two sets of piezoelectric elements polarized along the thickness are symmetrically bonded and shunted to form M bimorph pairs.

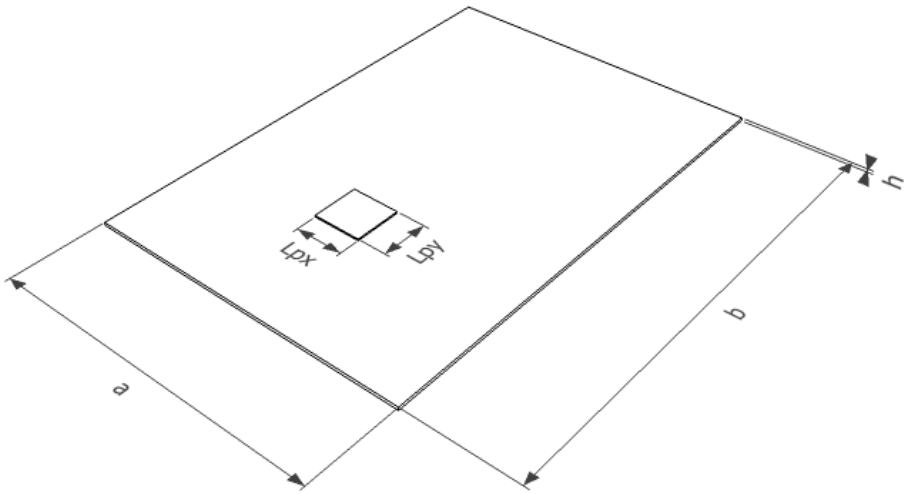

Figure 3.2: Geometry of the smart plate

The domain B of the plate is then divided in purely elastic portions, and three-layer piezoelectric portions with an elastic core. The geometry of the structure is resumed in figures 3.2, and 3.3. We identify the plate by its reference shape B. Let S be a flat surface of dimensions $a \times b$, $\underline{e}_3$ the corresponding normal unit vector, $\underline{r}$ a generic vector in the plane $(\mathbf{I} - \underline{e}_3 \otimes \underline{e}_3)$, where $\mathbf{I}$ is the unitary tensor, and $I(x, y)$ an interval corresponding to the plate thickness in the point (x, y). We assume that

$$B = \{\underline{r} + z\underline{e}_3, \underline{r} \in S, z \in I\}.$$

Introducing the function $\chi_r(x,y)$ that is unity where the r^{th} transducer exists, and otherwise is zero, it is possible to write the generic expression of the thickness interval, considering that the patches cannot overlap:

$$I(x,y) = I_2 \cup \left(\bigcup_{r=1}^{M} \chi_r(x,y) \left(I_1 \cup I_3 \right) \right) \tag{3.1}$$

The value of intervals is (see figure 3.3 for the layer thickness definitions)

$$I_1 = \left[-\frac{h}{2} - h_p, -\frac{h}{2} \right], \qquad I_2 = \left[-\frac{h}{2}, \frac{h}{2} \right], \qquad I_3 = \left[\frac{h}{2}, \frac{h}{2} + h_p \right].$$

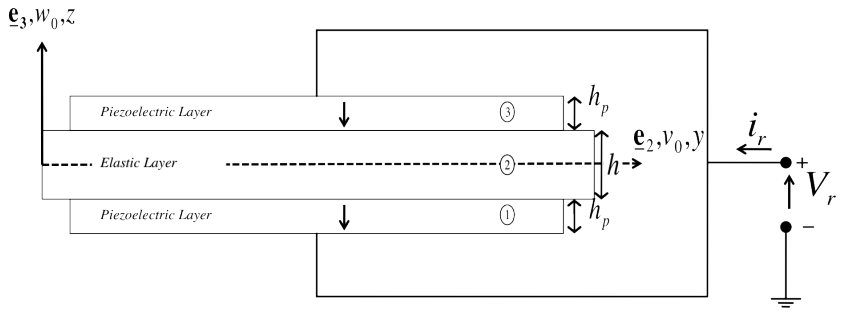

Figure 3.3: Transverse section of a piezoelectric actuator

Then following sets of indices are considered in order to distinguish between piezoelectric and elastic layers:

$$i = \{1,2,3,\}, \qquad l = \{1,3\}.$$

The boundary of B can be decomposed in the lateral boundary $\partial S \times I_1$, since there is the constraint that patches cannot touch the border. Througout the rest of the thesis we will denote by $\square^{(i)}$ a quantity in the generic i^{th} layer.

Kinematic restrictions for the elastic layer

According to the Kirchhoff-Love (K-L) plate theory, the following assumption for the displacement field is considered:

$$\underline{u}(x,y,z,t) = \underline{u}_0(x,y,t) + w_0(x,y,t)\underline{e}_3 - z\nabla w_0(x,y,t)$$

where w_0 is the transverse displacement, and

$$\underline{u}_0(x,y,t) = u_0(x,y,t)\,\underline{e}_{\mathbf{1}} + v_0(x,y,t)\,\underline{e}_{\mathbf{2}}$$

is the displacement of the middle plane. The differential operator is defined as follows

$$\nabla = \frac{\partial}{\partial x}\underline{e}_{\mathbf{1}} + \frac{\partial}{\partial x}\underline{e}_2.$$

The corresponding strain field is

$$\mathbf{S}(\underline{u}_0, w_0) = \mathbf{S}_0(\underline{u}) - z\mathbf{S}_1(w_0),$$

where

$$\mathbf{S}_0(\underline{u}_0) = sym(\nabla \underline{u}_0), \quad \mathbf{S}_1(w_0) = \nabla^2 w_0.$$

Remark 7. *The choice of considering a K-L plate theory instead of the more general Reissner-Mindlin (R-M) plate theory is motivated by to the fact that the approximations introduced the reduced K-L model do not affect the results considerably. This because the plate is considerably much thinner than the considered wavelengths.*

Kinematic restrictions for the piezoelectric layers

In each piezoelectric layer the assumptions for the electric potential $\varphi_r^{(l)}(x, y, z, t)$ and electric field $\underline{E}_r^{(l)}(x, y, z, t)$ on the r^{th} patch are

$$\varphi^{(l)}(x, y, z, t) = \varphi_0^{(l)}(x, y, t) + z\varpi^{(l)}\varphi_1^{(l)}(x, y, t), \tag{3.2}$$

$$\underline{E}^{(l)}(x, y, t) = -\text{grad}(\varphi^{(r)}) = -\frac{d\varphi^{(l)}}{dz}\underline{e}_3. \tag{3.3}$$

where the value of $\varpi^{(l)}$ depends on the polarization of the l^{th} layer. As shown in figure 3.3 it is $\varpi^{(1)} = -1$ and $\varpi^{(3)} = 1$. These conditions imply that, being V_r the voltage measured at the electrodes of each patch, and introducing $\Psi_r = \int V_r dt$ the flux linkage , the electric field is constant along the thickness and its value is

$$\underline{E}_r \cdot \underline{e}_3 = \frac{V_r^{(l)}}{h_p} = \varpi^{(l)}\frac{\dot{\Psi}_r^{(l)}}{h_p}. \tag{3.4}$$

A schematic diagram of voltage distribution along the thickness is displayed in figure 3.4.

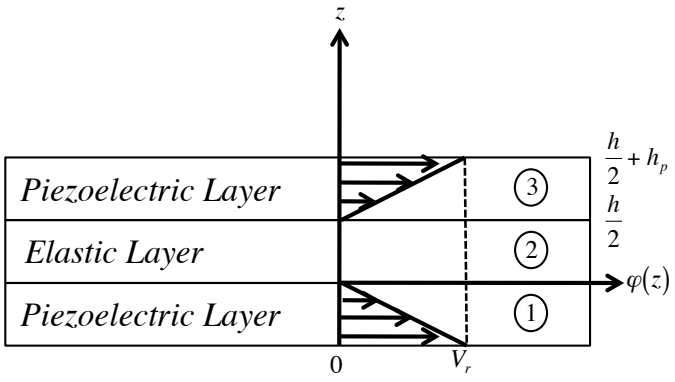

Figure 3.4: Voltage distribution along the thickness.

3.2.2 Principle of virtual work and balance equations

According to the kinematic conditions introduced a variational principle will be applied to the structure, in order to obtain balance equations and well-posed boundary conditions.

Internal work In order to apply principle of virtual work a suitable expression for the internal energy must be found. Introducing $\mathbf{T}$ and $\underline{D}$ as the stress tensor and the electric displacement vector, and defining by $\widetilde{\square}$ a virtual quantity, we can write the internal work L_{int} as

$$L_{int} = \underbrace{\delta E^m(\mathbf{T}(\underline{u}_0, w_0), \mathbf{S}(\tilde{\underline{u}}_0, \tilde{w}_0))}_{\text{Elastic energy}} + \sum_{r=1}^{M} \underbrace{\delta E^e_r(\underline{D}_r(V_r), \tilde{\underline{E}}_r(\tilde{V}_r))}_{\text{Electric energy}}. \tag{3.5}$$

In equation (3.5) there are two conservative terms, the variation of elastic energy δE^m and the sum of the variations of the electric energy δE^e_r for each patch. For the kinematic conditions introduced in each layer we have

$$\delta E^m = \int_S \int_I \mathbf{T}_\wp : sym\left[\nabla \tilde{\underline{u}}_0 - z\nabla^2 \tilde{w}_0\right], \tag{3.6}$$

$$\delta E^e_r = \int_S \int_I \chi_r(x,y) \frac{\underline{D}_r \cdot \underline{e}_3}{h_p} \tilde{V}_r, \tag{3.7}$$

where $\mathbf{T}_\wp = \mathbf{T}\ (\mathbf{I} - \underline{e}_3 \otimes \underline{e}_3)$ is the projection of $\mathbf{T}$ on the plane perpendicular to $\underline{e}_3$ and remembering that $\chi_r(x,y)$ is unity where the $r-th$ transducer exists, otherwise is zero. Introducing the terms

$$\mathbf{N} = \int_I \mathbf{T}_\wp, \qquad \mathbf{M} = \int_I -z\mathbf{T}_\wp, \qquad q = \int_I \frac{\underline{D} \cdot \underline{e}_3}{h_p},$$

we can write the final form for the internal energy

$$L_{int} = \underbrace{\int_S \mathbf{N} : sym(\nabla \tilde{\underline{u}}_0)}_{(a)} + \underbrace{\int_S \mathbf{M} : \nabla^2 \tilde{w}_0}_{(b)} + \underbrace{\int_S q\tilde{V}}_{(c)}. \tag{3.8}$$

where (a) is the virtual work of the forces acting on the plane $(\mathbf{I} - \underline{e}_3 \otimes \underline{e}_3)$, (b) that of the bending moments, (c) that of the electric forces.

External work In order to apply the principle of virtual work we now have to define the work done by the external forces and electric entities on the virtual displacements. Introducing $\underline{b}$, $\underline{f}$ as the body and surface forces acting on B, including the inertia forces, and Q_r as the electric charge of the $r-th$ transducer, we can write for the virtual work of a generic virtual displacement

$$L_{ext} = \int_B \underline{b} \cdot \tilde{\underline{u}} + \int_{\partial B} \underline{f} \cdot \tilde{\underline{u}} + \sum_{r=1}^{M} Q_r \tilde{V}_r. \tag{3.9}$$

	Force	Conjugate
Body	$\underline{b}_p = \sum_i \int_{I_i} \underline{b}$	$\tilde{\underline{u}}_0$
	$b_w = \sum_i \int_{I_i} \underline{b} \cdot \underline{e}_3$	$\tilde{w}_0$
	$\underline{b}_m = -\sum_i \int_{I_i} z\underline{b}$	$\nabla\tilde{w}_0$
Surface	$\underline{f}_p = \sum_i \int_{I_i} \underline{f}$	$\tilde{\underline{u}}_0$
	$f_w = \sum_i \int_{I_i} \underline{f} \cdot \underline{e}_3$	$\tilde{w}_0$
	$\underline{f}_m = \sum_i \int_{I_i} z\underline{f}$	$\nabla\tilde{w}_0$

Table 3.1: Decomposition of external forces with respect to the conjugate virtual quantities.

We now decompose the forces and the displacements in their respective conjugate quantities, this decomposition is summarized in table 3.1. With these assumptions the expression of the external work becomes

$$\begin{aligned} L_{ext} = &\int_S [\underline{b}_p \cdot \tilde{\underline{u}}_0 + b_w \tilde{w}_0 + \underline{b}_m \cdot \nabla\tilde{w}_0] + \\ &+ \int_{\partial S} [\underline{f}_p \cdot \tilde{\underline{u}}_0 + f_w \tilde{w}_0 + \underline{f}_m \cdot \nabla\tilde{w}_0] + \sum_{r=1}^{M} Q_r \tilde{V}_r. \end{aligned} \tag{3.10}$$

Balance equations The principle of virtual work states that

$$L_{int} = L_{ext}. \tag{3.11}$$

Considering equations (3.8) and (3.10), the balance equations on S can be obtained, preforming some integrations by parts, as

$$\nabla \cdot \mathbf{N} + \underline{b}_p = 0 \tag{3.12a}$$

$$\nabla^2 : (\mathbf{M}) + \nabla \cdot (\underline{b}_m) - b_w = 0, \tag{3.12b}$$

$$\sum_{r=1}^{M} \int_S \chi_r q_r - Q_r = 0, \tag{3.12c}$$

along with all boundary conditions on ∂B and $\partial(\partial B)$.

3.2.3 Constitutive equations

In this section the constitutive equations for each of both materials used for assembling the plate are investigated.
The aim is to derive the constitutive equations for the plate itself, that is $\mathbf{M}$, $\mathbf{N}$, q_r as functions of the reduced strain parameters and the electric field.

Elastic plate constitutive equations From the linear theory of elasticity we have, for the elastic layer

$$\mathbf{T} = \mathbb{C}\,\mathbf{S} \tag{3.13}$$

where $\mathbb{C}$ is the fourth order tensor of elasticity.

Piezoelectric constitutive equations According to [IEEE 1987] the constitutive equations for a piezoelectric material in the (S-E) form are

$$\mathbf{T}_p = \mathbb{C}_p^E \mathbf{S}_p - \mathbf{e}\underline{E}, \tag{3.14a}$$
$$\underline{D} = \mathbf{e}^t \mathbf{S}_p + \varepsilon^S \underline{E}. \tag{3.14b}$$

Another equivalent form (the T-E form) is obtained from the last equations

$$\mathbf{S}_p = \left(\mathbb{C}_p^E\right)^{-1} \mathbf{T}_p - \mathbf{d}\,\underline{E}, \tag{3.15a}$$
$$\underline{D} = \mathbf{d}^t\,\mathbf{S}_p + \varepsilon^T \underline{E}, \tag{3.15b}$$

where

$$\mathbf{e} = \mathbb{C}_p^E \mathbf{d}.$$

We will use these constitutive equations in the hypothesis of thin plates in plane stress and plane strain.

Smart plate constitutive equations In section 3.2.2 we defined the quantities $\mathbf{N}$, $\mathbf{M}$, q_r. Now that we have introduced constitutive equations for each layer, we can find the piezoelectric plate constitutive equations.

$$\mathbf{N} = \mathbb{K}_{Nu} \nabla \underline{u}_0, \tag{3.16a}$$
$$\mathbf{M} = \mathbb{K}_{Mw} \nabla^2 w_0 + e_r \chi_r V_r, \tag{3.16b}$$
$$q_r = -e_r \chi_r \nabla^2(w_0) + C_p \chi_r V_r, \tag{3.16c}$$

or in compact form

$$\begin{bmatrix} \mathbf{N} \\ \mathbf{M} \\ q_r \end{bmatrix} = \begin{bmatrix} \mathbb{K}_{Nu} & 0 & 0 \\ 0 & \mathbb{K}_{Mw} & \chi_r e_r \\ 0 & -\chi_r e_r & \chi_r C_p \end{bmatrix} \begin{bmatrix} \nabla(\underline{u}_0) \\ \nabla^2(w_0) \\ V_r \end{bmatrix} \tag{3.17}$$

where the coefficients are listed in table 3.2 and where we introduced $\xi_p = h_p/h$ as the ratio between the thickness of the piezoelectric layer and that of the elastic layer and

$$\alpha = 8\xi_p^3 + 12\xi_p^2 + 6\xi_p.$$

This parameter α which is related to the ratio between the thickness of the piezoelectric layer and the host plate will appear in the stiffness terms of the piezoelectric plate equations.

Coefficient	Value	Description
$\mathbb{K}_{Mw}$	$\frac{h^3}{12}\left[\mathbb{C}^E + \sum_{r=1}^{M} \chi_r \alpha \mathbb{C}_p^E\right]$	Bending Stiffness
e_r	$\frac{d_{31} Y_p h(\xi_p + 1)}{(1-\nu_p)}$	Bending Coupling
$\mathbb{K}_{Nu}$	$h(\mathbb{C}^E + \sum_{r=1}^{M} \chi_r 2\xi_p \mathbb{C}_p^E)$	Extensional Stiffness
k_{NV}	$\frac{d_{31} Y}{(1-\nu)}$	Extensional Coupling
C_p	$\frac{\varepsilon_{33}^S}{h_p}$	Capacitance

Table 3.2: Coefficients in piezoelectric plate constitutive equations, see appendix for definitions

3.2.4 Equations of motion

From equations (3.12) and using the system (3.16) we have the complete form of the Piezoelectric plate equations

$$\mathbb{K}_{Nu}\nabla^2 \underline{u}_0 + \underline{b}_p = 0, \tag{3.18a}$$

$$\mathbb{K}_{Mw}\nabla^4 w_0 + \nabla \underline{b}_m - b_w + \sum_{r=1}^{M} \chi_r e_r V_r = 0, \tag{3.18b}$$

$$\int_S \left(\chi_r C_p \dot{V}_r + \chi_r e_i \nabla^2 \dot{w}_0\right) = \imath_r, \tag{3.18c}$$

$$\tag{3.18d}$$

where $\imath_r = \dot{q}_r$ is the current flowing in each transducer.
In common applications one can neglect $\underline{b}_m$, that is given by

$$b_w = -\rho_{pl}\ddot{w}_0 + f_{ext}, \tag{3.19}$$

$$\underline{b}_p = -\rho_{pl}\ddot{\underline{u}}_0, \tag{3.20}$$

where the ρ_{pl} is the surface mass density, being the contribution of the piezoelectric patches to the overall mass density neglectable. Moreover, being the ratio ξ_p very little and considering that the patches do not entirely cover the plate, the contribution of the transducers to the overall stiffness can be neglected, and the bending stiffness S_{pl} is then defined as

$$S_{pl} = \frac{h^3}{12}\left[\frac{Y}{1-\nu^2}\right].$$

With these assumptions the system 3.18 becomes:

$$\mathbb{K}_{Nu}\nabla^2 \underline{u}_0 + \rho_{pl}\ddot{\underline{u}}_0 = 0, \tag{3.21a}$$

$$S_{pl}\nabla^4 w_0 + \rho_{pl}\ddot{w}_0 + \sum_{i=1}^{M} e_r \nabla^2 \chi_r V_r = f_{ext}, \tag{3.21b}$$

$$C_r \dot{V}_r - \int_S \chi_r C_p \dot{V}_r e_r \nabla^2(\dot{w}_0) = \imath_r, \tag{3.21c}$$

If we only consider bending vibration we have

$$\mathbb{K}_{Nu}\nabla^2 u_0 + \rho_{pl}\underline{\ddot{u}}_0 = 0.$$

This derives from the symmetry of the structure with respect to its mean plane, the so called bimorph configuration for the piezoelectric patches, and means that the extensional vibrations are uncoupled from the flux linkage.

Remark 8. *The bimorph configuration makes extensional vibrations uncoupled from flexural ones and electric potential. This is due to the symmetry of the structure with respect to the middle plane and to the chosen polarization for the transducers. However when using a small number of thin piezoelectric patches these couplings are neglectable. Then in common applications this approximation holds even if the transducers are bonded only on one side of the structure.*

The final form for the governing equations in terms of the transverse displacement and of voltages is

$$S_{pl}\nabla^4 w_0 + \rho_{pl}\ddot{w}_0 + \sum_{r=1}^{M} e_r \nabla^2(\chi_r) V_r = f_{ext}, \tag{3.22a}$$

$$C_r \dot{V}_r - \int_S \chi_r e_r \nabla^2(\dot{w}_0) = \imath_r. \tag{3.22b}$$

where $\nabla^2(\chi_r)$ must be considered as a limiting case of some continuous function of x, y.

3.2.5 Reduced Modal model

The reduced modal form of equations (3.22), is obtained introducing the following Galerkin decomposition, for the transverse displacement field $w_0(x, y, t)$:

$$w_0(x, y, t) = \sum_{i=1}^{N} Y_i(t)\,\phi_i(x, y), \tag{3.23}$$

where $Y_i(t)$ are the Fourier coefficients of the eigenfunctions $\phi_i(x, y)$ defined by the eigenvalue problem

$$\nabla^4\phi_i = \lambda_i^2\phi_i, \tag{3.24a}$$

$$\nabla^2\phi_i = -\lambda_i\phi_i, \tag{3.24b}$$

along with proper boundary conditions.
From equations (3.24) the values for natural frequencies are obtained

$$\omega_i = \lambda_i\sqrt{\frac{S_{pl}}{\rho_{pl}}}.$$

Substituting equation (3.23) into equations (3.22) and projecting on the given basis, we have

$$\rho\Omega_i^2 Y_i - \ddot{Y}_i - \sum_{r=1}^{M} \int_S \phi_i e_r \nabla^2 (\chi_r) V_r = f_i, \tag{3.25a}$$

$$C_p \dot{V}_r + \sum_{i=1}^{N} \int_S e_r \nabla^2 (\phi_i) \dot{Y}_i = \imath_r. \tag{3.25b}$$

Since there are no patches at the boundary, the inner product $\int_S \phi_i \nabla^2 (\chi_r)$ can be rewritten in a more convenient form:

$$\int_S \phi_i \nabla^2 (\chi_r) = \int_S \chi_r \nabla^2 (\phi_i) . \tag{3.26}$$

Then, using equation (3.24b) the modal coupling coefficient is defined as follows

$$g_{ir} = \int_S \chi_r e_r \nabla^2 (\phi_i) . \tag{3.27}$$

The non-dimensional form of system (3.25) is

$$\Omega_i^2 y_i - \ddot{y}_i - \sum_{r=1}^{M} \Omega_i \gamma_{ir} v_r = \overline{f}_i, \tag{3.28a}$$

$$\dot{v}_r + \sum_{i=1}^{N} \Omega_i \gamma_{ir} \dot{y}_i = \bar{\imath}_r. \tag{3.28b}$$

where the non-dimensional coupling coefficient is

$$\gamma_{ir} = \frac{g_{ir}}{\omega_i \sqrt{C_p \rho_{pl}}} \tag{3.29}$$

and where the circular frequencies Ω and Ω_i are

$$\Omega = \frac{\omega}{\Omega_0}, \quad \Omega_i = \frac{\omega_i}{\Omega_0} \tag{3.30}$$

being Ω_0 is a scaling circular frequency.
The non-dimensional state variables and forcing terms in equations (3.28) are given by

$$y = \frac{y}{l_0}, \quad v = \frac{V}{V_0}, \quad \overline{f}_i = \frac{f_i}{F_0} \quad \bar{\imath}_r = \frac{\imath_r}{\imath_0}.$$

with the following scaling voltage, force and current:

$$V_0 = l_0 \Omega_0 \sqrt{\frac{\rho_{pl}}{C_p}} \quad F_0 = l_0 \Omega_0^2 \rho_{pl} \quad \imath_0 = C_p \Omega_0 V_0.$$

In frequency domain the system (3.28) has this form:

$$\Omega_i^2 \hat{y}_i - \Omega^2 t y_i - \sum_{r=1}^{M} \gamma_{ir} \Omega_i \hat{v}_r = \hat{f}_i, \tag{3.31a}$$

$$j\Omega \hat{v}_r + j\Omega \sum_{i=1}^{N} \gamma_{ir} \Omega_i \hat{y}_i = \hat{\imath}_r. \tag{3.31b}$$

where $\hat{\square}$ denotes a non-dimensional quantity in frequency domain.

Compact notation

A more convenient form for writing equations (3.28) and (3.31) is in compact notation:

$$\ddot{\boldsymbol{y}} + \boldsymbol{\Omega}^2 \boldsymbol{y} - \boldsymbol{\Omega}\,\boldsymbol{\Gamma}\,\boldsymbol{v} = \boldsymbol{f} \tag{3.32a}$$

$$\dot{\boldsymbol{v}} + (\boldsymbol{\Omega}\,\boldsymbol{\Gamma})^{\mathrm{T}}\,\dot{\boldsymbol{y}} = \boldsymbol{\imath} \tag{3.32b}$$

and

$$\boldsymbol{\Omega}\hat{\boldsymbol{y}} - \Omega^2 \hat{\boldsymbol{y}} - \boldsymbol{\Omega}\,\boldsymbol{\Gamma}\,\hat{\boldsymbol{v}} = \hat{\boldsymbol{f}} \tag{3.33a}$$

$$j\Omega\hat{\boldsymbol{v}} + j\Omega\,(\boldsymbol{\Omega}\,\boldsymbol{\Gamma})^{\mathrm{T}}\,\hat{\boldsymbol{y}} = \hat{\boldsymbol{\imath}} \tag{3.33b}$$

where $\boldsymbol{y}$ is the vector of the non-dimensional modal coordinates, $\boldsymbol{v}$ the vector of the non-dimensional voltages, $\boldsymbol{f}$ the vector of the non-dimensional mechanical forcing terms, $\boldsymbol{\imath}$ the vector of the non-dimensional currents, $\boldsymbol{\Omega}$ the diagonal matrix of the non-dimensional circular eigenfrequencies and $\boldsymbol{\Gamma}$ the matrix of electromechanical couplings.
In order to introduce symmetry between mechanical and electrical equation the voltages V_r can be replaced by the flux linkages ψ_r.

$$\Psi = \int V dt, \qquad \dot{\Psi} = V. \tag{3.34}$$

Then equations (3.32) become:

$$\ddot{\boldsymbol{y}} + \boldsymbol{\Omega}^2 \boldsymbol{y} - \boldsymbol{\Omega}\,\boldsymbol{\Gamma}\,\dot{\boldsymbol{\psi}} = \boldsymbol{f} \tag{3.35a}$$

$$\ddot{\boldsymbol{\psi}} + (\boldsymbol{\Omega}\,\boldsymbol{\Gamma})^{\mathrm{T}}\,\dot{\boldsymbol{y}} = \boldsymbol{\imath} \tag{3.35b}$$

and in frequency domain:

$$\boldsymbol{\Omega}\hat{\boldsymbol{y}} - \Omega^2 \hat{\boldsymbol{y}} - j\Omega(\boldsymbol{\Omega})\,\boldsymbol{\Gamma}\,\hat{\boldsymbol{\psi}} = \hat{\boldsymbol{f}} \tag{3.36a}$$

$$\Omega^2\hat{\boldsymbol{\psi}} + j\Omega\,(\boldsymbol{\Omega}\,\boldsymbol{\Gamma})^{\mathrm{T}}\,\hat{\boldsymbol{y}} = \hat{\boldsymbol{\imath}} \tag{3.36b}$$

where $\boldsymbol{\psi}$ is the vector of non dimensional flux linkages and it is given by:

$$\psi_r = \frac{\Psi_r}{\Psi_0} \tag{3.37}$$

where the scaling flux linkage is $\Psi_0 = l_0\sqrt{\dfrac{\rho}{C_p}}$.

3.3 Linear multimodal passive control networks and optimization

3.3.1 Multimodal passive control circuits

In this sections several approaches for passive multimodal vibration control applied to the reduction of the radiated sound power are discussed.
The aim is to damp the most radiating modes, chosen using methods described in section 2.2. Since the intent is not to control each structural modes all the control effort has to be concentrated on the limited number of target modes. This is why only resonant shunts will be considered and all proposed control systems will be using a number of piezoelectric elements equal to the number of modes to be controlled.

3.3.2 Multiple RL Shunt

The simplest kind of passive resonant shunt for vibrations control is a RL circuit, introduced for the first time in [Hagood 1991]. It consists in an inductor in parallel with a resistor, shunted to the piezoelectric transducers, as in figure 3.5.

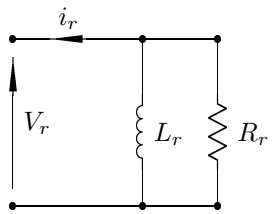

Figure 3.5: Equivalent circuit for a virtual passive shunt circuit in parallel configuration.

Since the piezoelectric patch can be also represented with a current generator in parallel with an inductor, the resulting electrical network is a resonant RLC circuit.

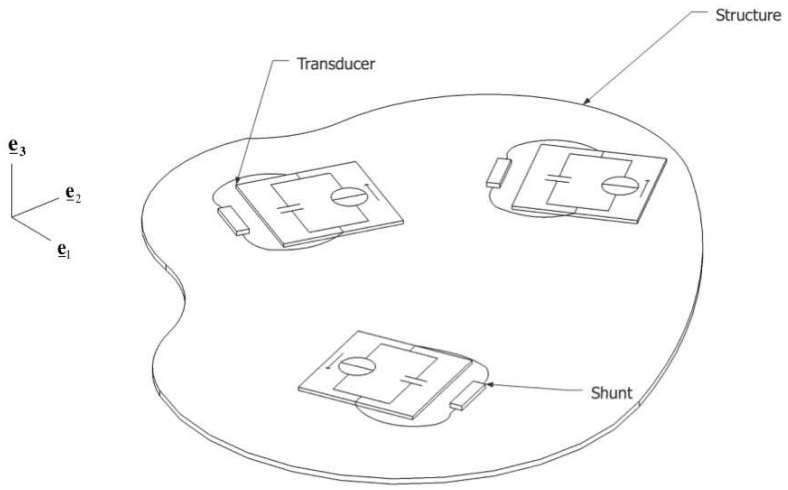

Figure 3.6: Smart structure with localize shunted piezoelectric transducers.

A schematic example of a smart structure with a set of shunted piezoelectric transducers is in figure 3.6
The forcing vector introduced in system (3.36) by shunting each transducer with a RL circuit is the following:

$$\boldsymbol{\imath} = -\mathscr{R}^{RL}\dot{\boldsymbol{\psi}} - \mathscr{L}^{RL}\boldsymbol{\psi} \tag{3.38}$$

and in frequency domain

$$\hat{\boldsymbol{\imath}} = -j\Omega\mathscr{R}^{RL}\hat{\boldsymbol{\psi}} - \mathscr{L}^{RL}\hat{\boldsymbol{\psi}} \tag{3.39}$$

where $\mathscr{R}^{RL}$ and$\mathscr{L}^{RL}$ are two diagonal matrices whose non-zero elements are $\mathscr{R}^{RL}_{ii} = (1/R_i)$ and $\mathscr{L}^{RL}_{ii} = 1/(L_i)$.
For each mode is then possible to write the closed loop equations as

$$\Omega_i^2\hat{y}_i + \Omega^2\hat{y}_i + \sum_{r=1}^{M} i\gamma_{ir}\Omega\Omega_i\hat{\psi}_{rr} = f_i, \tag{3.40a}$$

$$\Omega^2\hat{\psi}_r - j\Omega\frac{1}{\Omega_0 C_r R_r}\hat{\psi}_r - \frac{1}{\Omega_0 C_r L_r}\hat{\psi}_r + \sum_{i=1}^{M} j\gamma_{ir}\Omega\Omega_i\hat{y}_i = 0. \tag{3.40b}$$

This system has $2M$ degrees of freedom (dof), that are the mechanical resonance frequencies Ω_i and the electrical resonance frequencies $\overline{\Omega}_r = 1/(\Omega_0\sqrt{L_r C_r})$. Supposing to associate each transducer to a vibrational mode, the electric tuning and damping coefficient β_i and δ_i can be introduced as:

$$\beta_i = \left(\frac{\overline{\Omega}_i}{\Omega_i}\right)^2 = \frac{1}{\Omega_0^2\Omega_i^2 L_i C_i}, \tag{3.41}$$

$$\delta_i = \frac{1}{R_i C_r \Omega_i \Omega_0} \tag{3.42}$$

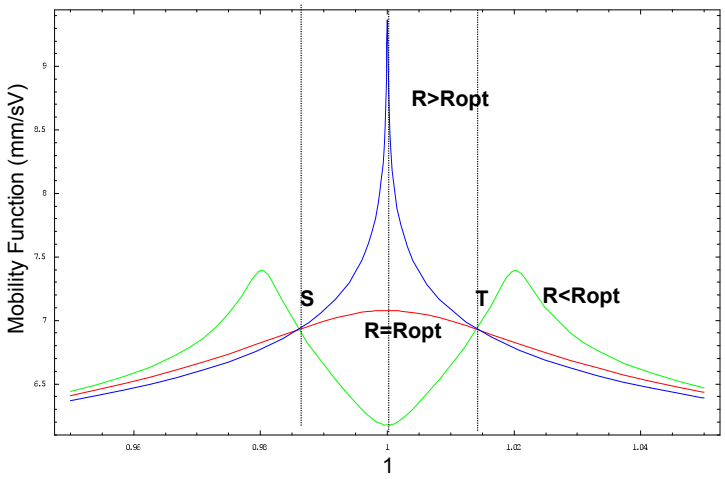

Figure 3.7: Fixed points.

. If the modes are sufficiently spaced in frequency, the system (3.40) becomes

$$\Omega_i^2 \hat{y}_i - \Omega^2 \hat{y}_i - j\gamma_{ii}\Omega\Omega_i\hat{\psi}_{ii} = f_i, \tag{3.43a}$$

$$\Omega^2\hat{\psi}_{r_r} + j\Omega\Omega_i\delta\hat{\psi}_i + \Omega_i^2\beta\hat{\psi}_i + j\gamma_{ii}\Omega\Omega_i\hat{y}_i = 0. \tag{3.43b}$$

Then it is possible to introduce the Mobility function as the ratio between the velocity $j\Omega\hat{y}$ and the forcing term $\hat{f}$ as

$$H(\beta, \delta, \Omega) = \frac{j\Omega\hat{y}}{\hat{f}} \tag{3.44}$$

Using equations (3.43) it is easy to derive the expression of the mobility function for the given system:

$$H(\beta, \delta, \Omega) = \frac{j\Omega\Omega_i^2\left(\beta - \Omega^2 + j\Omega\delta\right)}{\Omega^4 - j\Omega^3\delta - \Omega 2\left(\beta + 1 + \gamma_{ii}^2\right) + j\Omega\delta + \beta} \tag{3.45}$$

Now that the equation of the closed loop system has been written, the optimization of the circuit can be performed.

Optimization of the Forced response, the Fixed Points theory

Introduced for the first time in [Den Hartog 1956] for mechanical vibration absorbers, the fixed point theory can be used to describe the behaviour of two *dof* systems. The theory states that given two perfectly coupled systems, as in equations (3.43) , for a certain fixed value of β in the mobility function $H(\beta, \delta, \Omega)$, there exist two points that are common to all curves of the mobility, regardless of the damping value in the shunt circuit. It is important to remark that, in general, such two fixed points exist for continuous structures with well separated natural frequencies.

When β tends to infinity (meaning that $L \to 0$), $H(\infty, \delta, \Omega)$ is the mobility function corresponding to the case where the $r-th$ transducer is short-circuited. As stated by the fixed points theory it is possible to show that the absolute values of $H(\infty, \delta, \Omega)$ and $H(\beta, \delta, \Omega)$ for any value of δ intersect at two points $S = (\Omega_S, |H_S|)$ and $T = (\Omega_T, |H_T|)$ and that the two amplitudes $|H_S|$ and $|H_T|$ are equal when

$$\beta_{opt} = 1 \implies L_r = \frac{1}{\Omega^2 \Omega_i^2 C_r}. \tag{3.46}$$

that is the condition of resonance of the electric system at the mechanical resonance frequency.
The frequencies Ω_S and Ω_T can be calculated by looking for the intersection of the mobility functions $H(\beta, 0, \Omega)$ and $H(\beta, \infty, \Omega)$:

$$\Omega_{S,T} = \frac{1}{2}\sqrt{2 + 2\beta + \gamma^2 \pm \sqrt{(2 + 2\beta + \gamma^2)^2 - 16\beta}} \tag{3.47}$$

For optimizing the forced response a widely adopted approach consists in minimizing the $\mathscr{H}_\infty$ norm of the mobility function, defined as

$$||H(\beta, \delta, \Omega)||_\infty = \sup_{\Omega \in R} |H(\beta, \delta, \Omega)|. \tag{3.48}$$

Since for $\beta = \beta_{opt}$ the modulus of the mobility function has the same value, satisfying the condition (3.48) means setting the value of δ such that the transfer function $H(\beta_{opt}, \delta, \Omega)$ has horizontal tangents in Ω_S and Ω_T.
Than imposing

$$\frac{\partial}{\partial \Omega}|H(\beta_{opt}, \delta, \Omega_S)|\Big|_{\Omega=\Omega_S} = \frac{\partial}{\partial \Omega}|H(\beta_{opt}, \delta, \Omega_T)|\Big|_{\Omega=\Omega_T} = 0 \tag{3.49}$$

the resulting optimal value for the damping parameter is

$$\delta_{opt} = \sqrt{\frac{3}{2}}\gamma \tag{3.50}$$

The corresponding $\mathscr{H}_\infty$ norm of the mobility function is

$$H(\beta_{opt}, \delta_{opt}) = \frac{\sqrt{2}}{\gamma} \tag{3.51}$$

Optimization of the transient response, the Pole Placement criterion

The closed-loop pole locations have a direct impact on time response characteristics of the coupled system, such as transient oscillations. With the pole placement method, these poles are selected in advance in order to maximise all closed-loop pole distances from the imaginary axis, while remaining on the

left part of the complex plane. This means on one hand obtaining a large gain margin which guarantees asymptotic stability, on the other hand the largest decay rate of free oscillations, where the decay rate is defined by

$$D(\delta) = \min_{i=1,2,3,4} \left(|\mathrm{Re}(\lambda_i)| \right), \tag{3.52}$$

being λ the closed-loop poles of the i^{th} system.
The characteristic polynomial of the system (3.63) is in this form

$$\lambda^4 + \lambda^3\delta + \lambda^2(\gamma^2 + \beta + 1) + \lambda\delta + \beta. \tag{3.53}$$

As stated in [Hagood 1991] this condition is realized when the roots appear as two complex conjugate pairs. Hence, denoting the closed-loop poles associated with the i-th system by

$$\lambda_{1,2} = a + jb, \qquad \lambda_{3,4} = a - jb \tag{3.54}$$

the characteristic polynomial is then

$$(\lambda-\lambda_1)^2(\lambda-\lambda_4)^2 = \lambda^4 - 4a\lambda^3 + \lambda^2(6a^2+2b^2) - 4\lambda a(a^2+b^2) + (a^2+b^2). \tag{3.55}$$

By imposing that the characteristic polynomial (3.53) is in the desired form (3.55), the following optimal damping and tuning parameters are found:

$$\beta_{opt} = 1, \qquad \delta_{opt} = 2\gamma \tag{3.56}$$

and the associated decay rate is

$$D_{opt} = \frac{\gamma}{2}. \tag{3.57}$$

The root locus of the poles can be seen in figure 3.8.

On the stability

The last thing that has to be analyzed is the stability, to this end some energy considerations are made. Inserting the control law (3.38)in the governing equations (3.32) we obtain:

$$\ddot{\boldsymbol{y}} + \boldsymbol{\Omega}^2\,\boldsymbol{y} - \boldsymbol{\Omega}\,\boldsymbol{\Gamma}\,\dot{\boldsymbol{\psi}} = \boldsymbol{f}, \tag{3.58a}$$

$$\ddot{\boldsymbol{\psi}} + \mathscr{R}^{RL}\,\dot{\boldsymbol{\psi}} + \mathscr{L}^{RL}\,\boldsymbol{\psi} + (\boldsymbol{\Omega}\,\boldsymbol{\Gamma})^{\mathrm{T}}\,\dot{\boldsymbol{y}} = \boldsymbol{0}. \tag{3.58b}$$

Next, multiplying the first equation of system (3.58) by $\dot{\boldsymbol{y}}^{\mathrm{T}}$ and the second equation by $\dot{\boldsymbol{\psi}}^{\mathrm{T}}$ and rearranging, one obtains

$$\frac{d}{dt}\underbrace{\left(\frac{1}{2}\dot{\boldsymbol{y}}^{\mathrm{T}}\dot{\boldsymbol{y}}\right)}_{\text{Kinetic energy}} + \underbrace{\frac{1}{2}\boldsymbol{y}^{\mathrm{T}}\boldsymbol{\Omega}^2\boldsymbol{y}}_{\text{Potential energy}} = \underbrace{\dot{\boldsymbol{y}}^{\mathrm{T}}\boldsymbol{\Omega}\,\boldsymbol{\Gamma}\,\dot{\boldsymbol{\psi}}}_{\text{Converted energy}}, \tag{3.59a}$$

$$\frac{d}{dt}\underbrace{\left(\frac{1}{2}\dot{\boldsymbol{\psi}}^{\mathrm{T}}\dot{\boldsymbol{\psi}}\right)}_{\text{Electric Energy}} + \underbrace{\frac{1}{2}\boldsymbol{\psi}^{\mathrm{T}}\mathscr{L}^{RL}\boldsymbol{\psi}}_{\text{Magnetic energy}} = -\underbrace{\dot{\boldsymbol{\psi}}^{\mathrm{T}}\mathscr{R}^{RL}\,\dot{\boldsymbol{\psi}}}_{\text{Dissipated energy}} - \underbrace{\dot{\boldsymbol{\psi}}^{\mathrm{T}}(\boldsymbol{\Omega}\,\boldsymbol{\Gamma})^{\mathrm{T}}\,\dot{\boldsymbol{y}}}_{\text{Converted energy}}. \tag{3.59b}$$

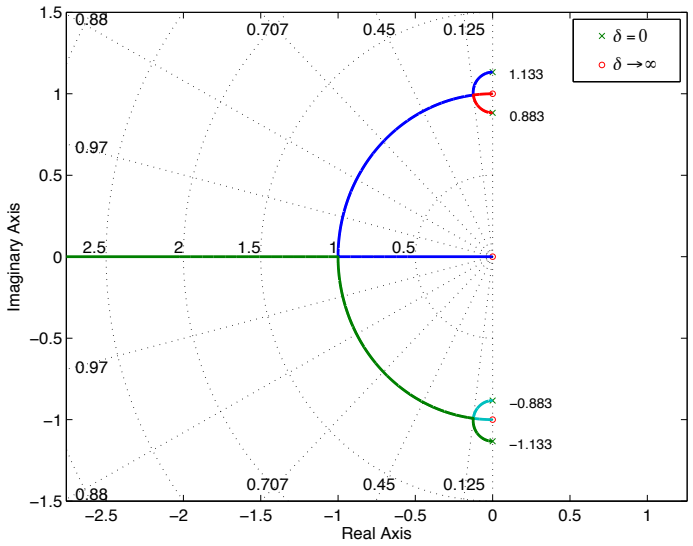

Figure 3.8: Root locus in function of the electrical damping δ.

On the left side of the first equation it is possible to identify the kinetic energy expressed in terms of modal velocities and the potential energy expressed in terms of modal displacements; on the left side of the second equation it is possible to recognise the electric energy stored in the piezoelectric inherent capacitances and the electric energy associated to the "inductive" gain matrix, $\mathscr{R}^{RL}$. Last terms on the right hand side represent the power through the piezoelectric elements toward the mechanical subsystem in the first equation, and toward the electric subsystem in the second equation. Hence, the balance of power through the piezoelectric elements yields

$$\dot{\boldsymbol{y}}^{\mathrm{T}}\boldsymbol{\Omega}\,\boldsymbol{\Gamma}\dot{\boldsymbol{\psi}} - \dot{\boldsymbol{\psi}}^{\mathrm{T}}\left(\boldsymbol{\Omega}\,\boldsymbol{\Gamma}\right)^{\mathrm{T}}\dot{\boldsymbol{y}} = 0 \tag{3.60}$$

Next, substituting equation (3.60) in system (3.59) we obtain:

$$\frac{d}{dt}\left(\frac{1}{2}\dot{\boldsymbol{y}}^{\mathrm{T}}\dot{\boldsymbol{y}} + \frac{1}{2}\boldsymbol{y}^{\mathrm{T}}\Omega^2\boldsymbol{y} + \frac{1}{2}\dot{\boldsymbol{\psi}}^{\mathrm{T}}\dot{\boldsymbol{\psi}} + \frac{1}{2}\boldsymbol{\psi}^{\mathrm{T}}\mathscr{L}^{RL}\boldsymbol{\psi}\right) = -\dot{\boldsymbol{\psi}}^{\mathrm{T}}\mathscr{R}^{RL}\dot{\boldsymbol{\psi}} \tag{3.61}$$

The expression inside the parentheses on the left hand side of equations (3.61) can be identified as the total energy of the system, including the effect of the inductive matrix, $\mathscr{L}^{RL}$. The objective of the feedback control is to drive the total energy to zero. Being the resistive matrix $\mathcal{R}^{RL}$ positive definite, the right hand side of Eqs. (3.61) is sure negative, except when $\dot{\boldsymbol{\psi}}$ vanishes. Thus, the energy is being dissipated at all times until the whole structure is driven to rest. Hence, in this case the electro-mechanical structure is guaranteed to be asymptotically stable. Moreover, anyway being the gain matrices $\mathscr{R}^{RL}$ and $\mathscr{L}^{RL}$ *positive definite* even an unconditional stability is assured.

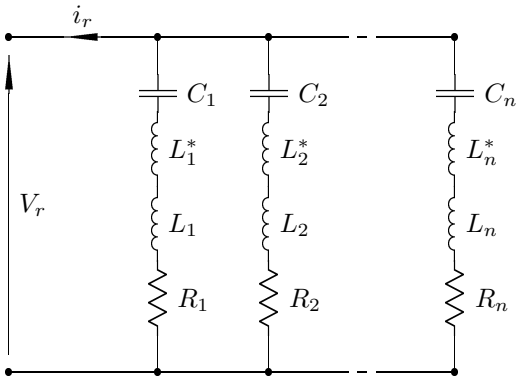

Figure 3.9: Example of a current flowing circuit.

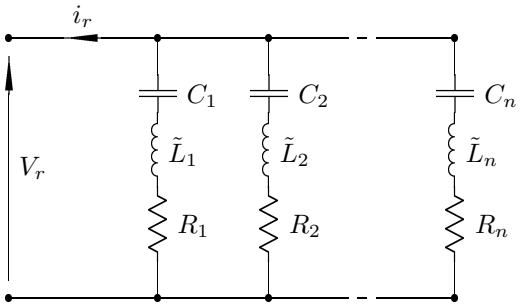

Figure 3.10: Example of a current flowing circuit with the actual value of the inductors.

3.3.3 Current flowing shunt

The *current flowing shunt* multimodal controller was introduced for the first time in [Behrens 2003], and has as goal the introduction of multimodal contro using a single patch. This is achieved using multiple RL shunts on the same patch, allowing the current to flow only in selected branches of the circuit, for selected frequencies.
This is achieved in a simple way, by using a series capacitor-inductor circuit as shown in Figure 3.9. The series is tuned to the structural resonance frequency. The series capacitor-inductor C_i^*, L_i^* circuit appears to be a short circuit at the selected frequency and approximately open circuit for all other frequencies. The shunting branch L_i, C_i is also tuned to Ω_i. Therefore, each circuit branch, C_i^*, L_i^*, L_i, R_i is functional at its own frequency Ω_i, while being approximately open circuit at all other frequencies. Some level of interaction between modes that are closely spaced is expected. However, for modes that are widely spaced, this interaction will be minimal.

Since the two inductors L_i^* tuned with C_i^* and L_i tuned with C_r are in series, they can be replaced by a single inductor $\tilde{L}_i = L_i^* + L_i$, as showed in figure 3.10.

The admittance of the generalized shunt is then, for the r^{th} transducer:

$$Y_r(\Omega) = \sum_{i=1}^{M} \frac{j\Omega(1/L_i)}{-\Omega^2 + j\Omega(R_i/L_i) + 1/(C_i L_i)} \tag{3.62}$$

This expression does not depends on r, because the exactly the same circuit i replicated for each transducer. This circuit has the same behaviour of a RL shunt, and therefore the optimal value for the resistance is obtained in the same way.
The advantage of this circuit is the introduction of several electrical degrees of freedom using only one patch. When generalizing the controller for using more actuators, one can only replicate the circuit for each one of those. Being this circuit an extension of an RL series shunt, there is non need to proof its unconditional stability.

Remark 9. *The introduction of a capacitance in the shunt branch compromise the performances reducing the electromechanical coupling, and then its value must be small. This has as a counter effect that the resonant branch requires a very high value inductance end this exclude a purely passive realization of the circuit, even at high frequencies.*

3.3.4 RL network

From the analysis of the two previous systems, it is clear that for improving the performances of the controller the use of multiple patches is necessary. Moreover, the simple replica of the same circuit on each patch, while it permits the control of multiple modes, as for the multiple RL shunt, does not take advantage of the distribution of the patches over the structure. In fact, if the piezoelectric patches are optimally positioned and iterconnected, they can act simultaneously and coordinate the control effort over a target mode. A schematic example of a network of interconnected transducers is in figure 3.11.
This idea is at the basis of the design of the following control network, proposed in [Giorgio 2009]. As for the other control strategies the number of piezoelectric patches will be assumed equal to the number of target modes.
We start from the reduced modal model of the structure:

$$\ddot{\boldsymbol{y}} + \boldsymbol{\Omega}^2 \boldsymbol{y} - \boldsymbol{\Omega}\,\boldsymbol{\Gamma}\,\dot{\boldsymbol{\psi}} = \boldsymbol{f} \tag{3.63a}$$

$$\ddot{\boldsymbol{\psi}} + (\boldsymbol{\Omega}\,\boldsymbol{\Gamma})^{\mathrm{T}}\,\dot{\boldsymbol{y}} = \boldsymbol{\imath} \tag{3.63b}$$

Then the following linear transformation for the electric state variable is introduced

$$\boldsymbol{\psi} = \boldsymbol{U}\boldsymbol{\chi} \tag{3.64}$$

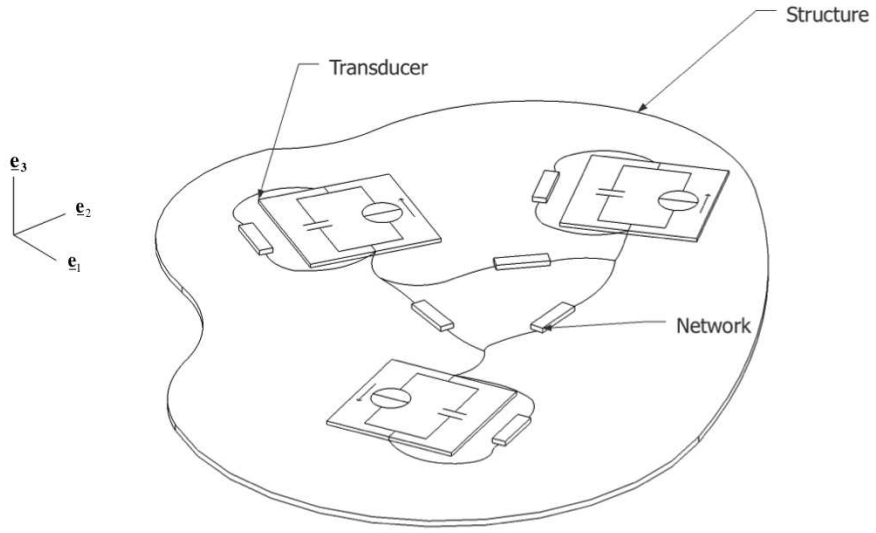

Figure 3.11: A schematic distribution of piezoelectric actuator for a multimodal shunt.

where $\boldsymbol{U}$ is an M-square matrix and it is the best transformation matrix that makes the normalized electro-mechanical coupling matrix in the new state space, $\mathscr{G} = \boldsymbol{\Gamma U}$, as diagonal as possible.

In this way, being the coupling matrix $\mathscr{G}$, a set of single mode piezoelectric shunting systems is obtained, in the new state space, as it was for the multiple RL shunt. In fact, the control law adopted represents a generalized parallel RL shunt circuit in the state space defined by the before mentioned transformation, in accordance with Wu's method [Wu 1996].
Thus, this network is an inductive-resistive, and the circuit obtained in the actual space is passive, for the constitutive matrices are symmetric and positive definite.
The new governing equations, assuming $\mathscr{G}$ diagonal, are represented by

$$\ddot{\boldsymbol{y}} + \boldsymbol{\Omega}^2 \boldsymbol{y} - \boldsymbol{\Omega}\mathscr{G}\dot{\boldsymbol{\chi}} = \boldsymbol{f}, \tag{3.65a}$$

$$\ddot{\boldsymbol{\chi}} + (\boldsymbol{\Omega}\mathscr{G})^{\mathrm{T}}\dot{\boldsymbol{y}} = \boldsymbol{z}, \tag{3.65b}$$

or in other words as n single mode piezoelectric shunting systems uncoupled. The vector $\boldsymbol{z} = \boldsymbol{U}^{\mathrm{T}}\boldsymbol{\imath}$ is a new control input.

Remark 10. *The matrix $\boldsymbol{U}$ does exist if the rows of $\boldsymbol{\Gamma}$ are mutually orthogonal, if not some terms out of the main diagonal will be different from zero. This can affect the performances of the system, especially if the modes are not sufficiently spaced in frequency.*

At this point, it is possible to define in according with Wu's method the generalised control vector $\boldsymbol{z}$ as

$$\boldsymbol{z} = -\mathscr{R}\,\dot{\boldsymbol{\chi}} - \mathscr{L}\,\boldsymbol{\chi}, \tag{3.66}$$

defining the diagonal matrices $\mathscr{R}_{hk} = (1/r_h)\delta_{hk}$ and $\mathscr{L}_{hk} = (1/\ell_h)\delta_{hk}$. The parameters r_h and ℓ_h are the generalized resistance and inductance respectively. Thus, the actual control law, $\boldsymbol{\imath}$, assumes the form

$$\boldsymbol{\imath} = -\mathcal{N}_R\,\dot{\boldsymbol{\psi}} - \mathcal{N}_L\,\boldsymbol{\psi}, \tag{3.67}$$

setting

$$\mathcal{N}_R = \boldsymbol{U}\mathscr{R}\,\boldsymbol{U}^{\mathrm{T}}, \quad \mathcal{N}_L = \boldsymbol{U}\mathscr{L}\,\boldsymbol{U}^{\mathrm{T}} \tag{3.68}$$

where $\mathcal{N}_R$ and $\mathcal{N}_L$ are control gain matrices. Because r_h and ℓ_h are strictly positive and the matrix $\boldsymbol{U}$ is orthogonal, it follows that the gain matrices $\mathcal{N}_R$ and $\mathcal{N}_L$ are *symmetric* and *positive definite*. The column vectors $\boldsymbol{u}_h$'s of the matrix $\boldsymbol{U}$ can be interpreted as their common eigenvectors, and $(1/r_h)$'s and $(1/\ell_h)$'s are the corresponding eigenvalues.

On the stability

The main question remaining is the nature of the gain matrices $\mathcal{N}_R$ and $\mathcal{N}_L$. To examine the requirement on these matrices, energy considerations are made, as already done for the multiple RL shunt.
In the same way, inserting the control law (3.67) in the governing equations (3.63), we obtain

$$\ddot{\boldsymbol{y}} + \boldsymbol{\Omega}^2\,\boldsymbol{y} - \boldsymbol{\Omega}\,\boldsymbol{\Gamma}\,\dot{\boldsymbol{\psi}} = \boldsymbol{f}, \tag{3.69a}$$

$$\ddot{\boldsymbol{\psi}} + \mathcal{N}_R\,\dot{\boldsymbol{\psi}} + \mathcal{N}_L\,\boldsymbol{\psi} + (\boldsymbol{\Omega}\,\boldsymbol{\Gamma})^{\mathrm{T}}\,\dot{\boldsymbol{y}} = \boldsymbol{0}. \tag{3.69b}$$

This system has the same structure of system (3.58), then, being for the selected transformatio, the matrices $\mathcal{N}_L$ and $\mathcal{N}_R$ positive definite, the same considerations on stability can be done. Multiplying on the left the first equation of the (3.69) by $\dot{\boldsymbol{y}}^{\mathrm{T}}$ and the second equation by $\dot{\boldsymbol{\psi}}^{\mathrm{T}}$ and rearranging, one obtains

$$\frac{d}{dt}\Bigg(\underbrace{\frac{1}{2}\dot{\boldsymbol{y}}^{\mathrm{T}}\dot{\boldsymbol{y}}}_{\text{Kinetic energy}} + \underbrace{\frac{1}{2}\boldsymbol{y}^{\mathrm{T}}\boldsymbol{\Omega}^2\boldsymbol{y}}_{\text{Potential energy}}\Bigg) = \underbrace{\dot{\boldsymbol{y}}^{\mathrm{T}}\boldsymbol{\Omega}\,\boldsymbol{\Gamma}\,\dot{\boldsymbol{\psi}}}_{\text{Converted energy}} \tag{3.70a}$$

$$\frac{d}{dt}\Bigg(\underbrace{\frac{1}{2}\dot{\boldsymbol{\psi}}^{\mathrm{T}}\dot{\boldsymbol{\psi}}}_{\text{Electric Energy}} + \underbrace{\frac{1}{2}\boldsymbol{\psi}^{\mathrm{T}}\mathcal{N}_L\boldsymbol{\psi}}_{\text{Magnetic energy}}\Bigg) = -\underbrace{\dot{\boldsymbol{\psi}}^{\mathrm{T}}\mathcal{N}_R\,\dot{\boldsymbol{\psi}}}_{\text{Dissipated energy}} - \underbrace{\dot{\boldsymbol{\psi}}^{\mathrm{T}}(\boldsymbol{\Omega}\,\boldsymbol{\Gamma})^{\mathrm{T}}\,\dot{\boldsymbol{y}}}_{\text{Converted energy}} \tag{3.70b}$$

The balance of power through the piezoelectric elements yields

$$\dot{\boldsymbol{y}}^{\mathrm{T}}\Omega\,\Gamma\,\dot{\boldsymbol{\psi}} - \dot{\boldsymbol{\psi}}^{\mathrm{T}}\,(\Omega\,\Gamma)^{\mathrm{T}}\,\dot{\boldsymbol{y}} = 0 \tag{3.71}$$

Then, with the use of equation (3.71), in system (3.70):

$$\frac{d}{dt}\left(\frac{1}{2}\dot{\boldsymbol{y}}^{\mathrm{T}}\dot{\boldsymbol{y}}+\frac{1}{2}\boldsymbol{y}^{\mathrm{T}}\Omega^{2}\boldsymbol{y}+\frac{1}{2}\dot{\boldsymbol{\psi}}^{\mathrm{T}}\dot{\boldsymbol{\psi}}+\frac{1}{2}\boldsymbol{\psi}^{\mathrm{T}}\mathcal{N}_{L}\boldsymbol{\psi}\right)=-\dot{\boldsymbol{\psi}}^{\mathrm{T}}\mathcal{N}_{R}\,\dot{\boldsymbol{\psi}} \tag{3.72}$$

This equation has the same structure as equation (3.61), and then the same reasoning can be followed, concluding, being the matrices $\mathcal{N}_L$ and $\mathcal{N}_R$ positive definite, that the unconditional stability of the system is assured.

3.3.5 Comparison

The comparison between these three control circuits will be the object of the last section of this chapter, sections 4.4.2, dedicated to the simulations. A preliminary comparison between the main characteristics of these circuits is in table 3.3.

3.4 Transducers positioning optimization for the control radiated sound power

The choice of transducer positioning is a crucial step when conceiving a smart structure. This because the position of the transducers influences the energy exchange between the mechanic and electric part of the circuit, and then affects the overall behaviour and efficacy of the controller. Since each piezoelectric patches is a co-located sensor/actuator pair, its positioning does not influence the stability of the system.
In the literature there exist several criterion for performing this optimization, depending on the nature of the structure and of the controller, and a number of articles focus on thin plates. These methods of optimization can be divided in two main categories:

Open loop optimizations Open loop methods consider the structure without any circuit connected to it. These methods are based on parameters that can be directly derived from the model, such as the electromechanic coupling coefficients or the strain energy.

Closed loop optimizations Closed loop methods consider the structure connected to the controller. These method often give a finer optimization, being the energy transfer between the mechanic and the optimized electric system, but they are often very expensive in terms of computational costs, since a numerical procedure must be used during the optimization.

The optimization method proposed in this section is essentially based

Multiple RL Shunt	Current Flowing	RL Network
✓Simple circuit ✓Good performances	✓Simple circuit ✓Multimodal control with one patch	✓Optimized multimodal control ✓Very good performances ✓Robustness
✗ High value of the inductors ✗ Mistuning ✗ Not optimized for multimodal control	✗ Medium performances ✗ Mistuning ✗ Very high value of the inductors	✗ Very complex circuit ✗ Needs an I/O real time system

Table 3.3: Comparison between differnt types of passive control circuits

on the open loop model of the structure, but takes also into account the nature of the controller. This because the RL control network needs a coupling matrix with the rows as mutally orthogonal as possible. In [Giorgio 2009] the optimization procedure for the piezoelectric positioning is obtained using a closed loop method, performing complex and long calculations. Without performing complicated and long calculations, a good result can be obtained exploiting the symmetries of she structure and the orthogonality of the eigenmodes, as shown later in this section.
Following the literature the concept of spatial $\mathscr{H}$ norm, useful to describe the spatial structural vibration response of the system in an average sense, see [Halim 2003], is used. This concept will be extended to the acoustic optimization using concepts of modal radiation efficiencies introduced in chapter 2

About the electromechanical coupling Consider a piezoelectric patch of dimensions L_{px} L_{py} bonded on a plate, as shown in figure 3.12.

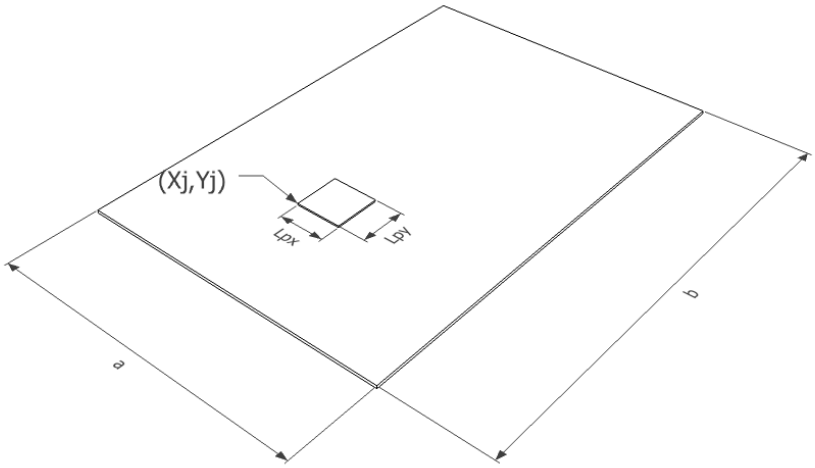

Figure 3.12: Plate with a piezoelectric element.

Assuming that one corner of the patch is located at (x_j, y_j) the value of the non-dimensional coupling coefficient $\gamma_{ir}(x_j, y_j)$ in function of the position of the transducer is, from equation (3.29):

$$\gamma_{ir}(x_j, y_j) = \frac{1}{S_t}\sqrt{\frac{\rho}{C_p}}\int_{x_j}^{x_j+L_{px}}\int_{y_j}^{y_j+L_{py}} e_r\phi_i \mathrm{d}x\mathrm{d}y \tag{3.73}$$

From equation (3.73) it is clear that the coupling between the $r-th$ transducer and the $i-th$ transducer depends on four factors:

- the positioning (x_j, y_j),
- the dimensions L_{px} L_{py},
- the material and the thickness of the transducer e_r,
- The modal shapes ϕ_i

Since the last three parameters are assumed to be fixed, the quantity that will be optimized is the placement (x_j, y_j). The cost function for the optimization will be a function only of the position (x_j, y_j).

About the cost function The objective of this optimization is the maximization of the controller authority over the radiated sound power, so that the efficacy of the controller is maximized, using a fixed number of transducers. To this end the concepts introduced in Chapter 2, and in particular the modal radiation efficiency, are used to choose the cost function.
The inputs of the optimization are then

- modal model of the host structure
- modal radiation coefficients
- piezoelectric transducers
- Maximum frequency of interest f_{max}, the same used for calculating the modal radiation coefficients.

The outputs will be:

- the minimum number of piezoelectric transducers to be used for an efficient reduction of the radiated sound power
- the optimal location for the transducers

in order to do this a mixed optimization method, based on the open loop model of the structure corrected with some informations about the controller behaviour, will be used.

3.4.1 Choosing the number of transducers

The first step is to determine the number of transducers to be used. Since the control circuit uses a number of patches equal to the number of modes that have to be controlled, it is crucial to determine the most radiating modes within in the frequency range of interest, that is for $f < f_{max}$. To this end

the modal radiation coefficients $\overline{\eta}_i$ introduced in section 2.2.2 are used, along with the consideration about the sensitivity of the human ear.
In fact, as shown in section 2.4, since the human ear less sensitive at low frequency, some modes can be neglected, being their contribution to the perceived sound is too low.
In order to do this the A-weighing, introduced as well in section 2.4, is considered. The function $A(f)$ defined by the equation (2.116) is normalized for having a value of zero dB when it has its maximum. In this way the value $A(f_i)$ gives an absolute value of how different a sound with the same intensity is perceived. The set of indices ξ_C which identifies the modes that have to be controlled can be then identified, for instance, using the following definition:

$$\xi_C := \forall i / \left(f_i < f_{max}\right) \left(A(f_i) < \tau\right) \left(\overline{\eta}_i > 0.1\right), \tag{3.74}$$

where τ is a pre-defined threshold. In common application the value of τ can be fixed around $-20dB$, which corresposds, as shown in figure 3.13, in neglecting the modes below $100Hz$.

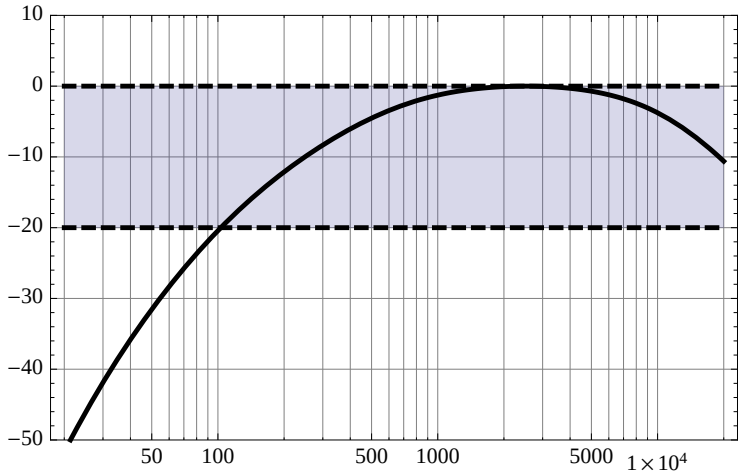

Figure 3.13: A-weighting courbe with the range of the treshold $\tau = -20dB$ highlighted.

Optimization of the positioning, the notion of spatial $\mathscr{H}_2$ norm

The main difficulties in optimizing the positioning of piezoelectric transducers lies in choosing a cost function that really represents the controller authority over the acoustic radiation of the system, in an average sense.
In vibration mechanics the cost function is usually based on some norm of the transfer function form the $r-th$ transducer voltage to the transverse velocity of the plate in a point $j\Omega w_0(x, y)$. Form the modal decomposition (3.23) the

transfer function takes the form

$$G_r(x,y,\Omega) = \frac{j\Omega w_0(x,y\Omega)}{V_r(\Omega)} = \sum_{i=1}^{N} \frac{j\Omega\eta_i(\Omega)\Phi_i(x,y)}{V_r(\Omega)} \tag{3.75}$$

From the modal equations (3.31) is:

$$G_r(x,y,\Omega) = \sum_{i=1}^{N} \frac{j\Omega\gamma_{ir}\Phi_i}{-\Omega^2+\Omega_i^2+2j\Omega\Omega_i\zeta_i} \tag{3.76}$$

where we added the structural damping ζ_i. The $\mathscr{H}_2$ norm of $G_r(x,y,\Omega)$ is defined as follows:

$$\|G_r(x,y,\Omega)\|_2^2 = \int_{-\infty}^{\infty} \text{trace}\left\{G_r(x,y,\Omega) * G_r(x,y,\Omega)\right\} \mathrm{d}\Omega \tag{3.77}$$

The $\mathscr{H}_2$ norm of $G_r(x,y,\Omega)$ can be used to obtain the response characteristics at the point (x,y). However, it does not give any information on the responses of other parts of the structure, because it only considers reaction a specific location on the plate. To overcome the difficulty in obtaining the response characteristics of the entire structure, the notion of Spatial $\mathscr{H}_2$ norm was introduced in [Halim 2003, Moheimani 1999]. The Spatial $\mathscr{H}_2$ norm of $G(x,y,\Omega)$ is then defined as

$$\langle\langle G_r(x,y,\Omega)\rangle\rangle_2^2 = \frac{1}{2\pi}\int_{-\infty}^{\infty}\int_S \text{trace}\left\{G_r(x,y,\Omega) * G_r(x,y,\Omega)\right\} \mathrm{d}r\mathrm{d}\omega. \tag{3.78}$$

where $r \in S$ are all the points of the plate. For the orthonormality properties of the eigenfunctions, and supposing that the modes are sufficiently spaced in frequency, the expression can be simplified in this way

$$\langle\langle G_r(x,y,\Omega)\rangle\rangle_2^2 = \sum_{i=1}^{N} \left\|\tilde{G}_{ir}\right\|_2^2 \tag{3.79}$$

where

$$\tilde{G}_{ir} = \frac{j\Omega\gamma_{ir}}{-\Omega^2+\Omega_i^2+2j\Omega\Omega_i\zeta_i}$$

Since it involves the integration over the entire structure, the spatial $\mathscr{H}_2$ norm gives information on the response of all points of the plate.

Modal Controllability and Spatial Controllability

Modal controllability and Spatial controllability are defined in this way: the modal controllability is a measure of controller authority over each mode, while the spatial controllability represents controller authority over the entire structure, or a number of selected modes, in an average sense.

Form equation (3.78) it is clear that the global response of the system is due to the sum of the contribution of each mode. To this end, assuming that one corner of the r^{th} piezoelectric patch is located at the point $(x_n, y_n) \in B$, the function $\kappa_{in}(x_n, y_n)$ is defined as follow:

$$\kappa_{in}(x_n, y_n) = \left\| \tilde{G}_{ir} \right\|_2 . \tag{3.80}$$

Then the modal controllability is defined as

$$\mathscr{M}_{in}(x_n, y_n) = \frac{\kappa_{in}(x_n, y_n)}{\max_{i=1...N}(\kappa_{in}(x_n, y_n))}, \tag{3.81}$$

and it represents the control authority of a patch placed in (x_n, y_n) over the i^{th} mode. Optimizing the modal controllability $\mathscr{M}_{inr}(x_n, y_n)$ means finding the point $(x_n, y_n) \in B$ which maximizes the coupling between the r^{th} patch and the i^{th} mode. This can be enough when considering single degree of freedom electrical controller, such as a RL shunt, but it is clearly insufficient when considering control strategies in which every patch has to be coupled with several modes.
Hence there is the need of introducing a quantity that represents the controller authority over the entire structure, or a number of selected modes, in an average sense. The spatial controllability is defined as follows:

$$\mathscr{S}_n(x_n, y_n) = \frac{1}{\beta_n} \sqrt{\sum_i^N \kappa_{in}(x_n, y_n)^2} \tag{3.82}$$

where $\beta_n = \max_{(x_n,y_n)\in R} \sqrt{\sum_i^N \kappa_{in}(x_n, y_n)^2}$.
A classical constrained problem consist in maximizing the spatial controllability, while maintaining the modal controllability of each mode i over a certain threshold b_i

$$\max_{(x_n,y_n)\in R} \mathscr{S}_n(x_n, y_n) \quad \text{subject to } \mathscr{M}_{inr}(x_n, y_n) \geqslant b_i, \quad i = 1...N \tag{3.83}$$

3.4.2 Acoustic controllability

In the literature the spatial $\mathscr{H}_2$ norm is used to introduce the concepts of spatial controllability and modal controllability But, since the radiated sound power is a quadratic function of the velocity, can be used also for an acoustic based optimization. The concept of Acoustic Controllability can then be introduced as the controller authority over the radiated sound power, in an average sense.
Then, from the concept described in section 3.4.1 it is possible to formulate another cost function for acoustic purposes. Being the number of piezoelectric patches limited, and given the chosen control strategy uses one transducer for

each mode that has to be controlled, only a selected number of modes are selected among the most radiating ones. These selected modes are identified by the set of indices ξ_C and determined with the use of equation (3.74).

A new cost function, the acoustic controllability $\mathscr{A}_n$, is then defined starting from modal controllability, introducing in the definition of spatial controllability the normalized modal efficiency $\eta_i^{norm} = \overline{\eta}_i / \max \eta_i$ as defined in Chapter 2:

$$\mathscr{A}_n(x_n, y_n) = \frac{1}{\tilde{\beta}_n} \sqrt{\sum_{i \in \xi_C} \eta_i^{norm} \kappa_{in}(x_n, y_n)^2} \tag{3.84}$$

where $\tilde{\beta}_n = \max_{(x_n,y_n)\in R} \sqrt{\sum_{i\in\xi} \eta_i^{norm} \kappa_{in}(x_n, y_n)^2}$.
The optimization of the acoustic controllability $\mathscr{A}$ gives then the point $(x_n, y_n) \in S$ which maximize the control authority over the acoustic radiation in the selected band.

3.5 Simulations

In this section the modelling flow described in the previous sections will be applied to a case study. The first step will be the modal analysis and the acoustic characterization of the plate is performed,, in order to derive the modal radiation efficiency needed for optimizing the controller. The last step will be the optimization of the piezoelectric patches placement, following the method introduced in section 3.4. Then the system is connected with the control networks described in section 3.3.

3.5.1 Modal analysis and acoustic characterization of the structure

The structure selected for the case study is a simply supported aluminium plate, whose characteristics are resumed in table 3.4, in an infinite baffle, radiating into an infinite halfspace filled with air.

Parameter	Value
Length	30 cm
Width	21 cm
Thickness	2 mm

Table 3.4: Host plate parameters.

Being the plate simply supported, the eigenvalue problem

$$\nabla^4 \phi_{mn} = \lambda_{mn}^2 \phi_{mn},$$

has analytical solutions in the form:

$$\phi_{mn} = \frac{1}{\sqrt{ab}} \sin\left(\frac{m\pi}{a}x\right) \sin\left(\frac{n\pi}{b}y\right),$$

$$\lambda_{mn} = \sqrt{\frac{S}{\rho}\left(\left(\frac{m\pi}{a}\right)^2 + \left(\frac{n\pi}{b}\right)^2\right)}.$$

Then the indexes (m, n) are replaced by the index i, ordering the eigenvalues from the lowest to the highest. The first ten modal shapes calculated for the plate are plotted in figure 3.14 and the corresponding natural frequencies are listed in table 3.5.

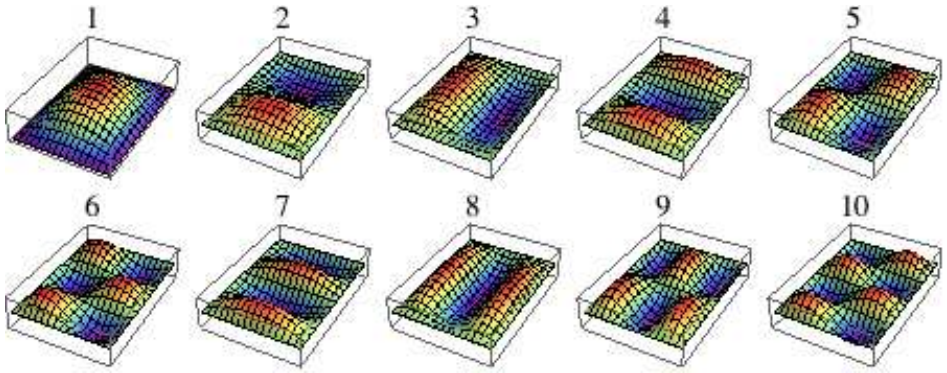

Figure 3.14: Modal shapes

Following the procedure described in section 2.2, the structure is decomposed in a matrix of 12×12 elementary elements radiating as pistons. The maximal frequency of interest has been chosen equal to $f_{max} = 1300$, in order to consider the first ten modes. The obtained modal radiation coefficients are listed in table 3.5 and in figure 3.15. The modal radiation coefficients show how the most radiated modes are the odd ones, and this is in agreement with the literature [Cremer 1973] and it is due to the antisymmetric distribution of the velocity field.
The set ξ_C of modes that have to be controlled are then distinguished with the aid of equation 3.74, and it is:

$$\xi_C = \{1, 4, 8\} \tag{3.85}$$

3.5.2 Piezolectric patches placement optimization

In this section the concepts introduced in section 3.4 will be applied to the considered structure. Several piezo-elements will be connected in parallel, as done in section 3.4, in order to obtain a coupling matrix as orthogonal as possible and in order to uncouple even modes. Since the number of modes

mode	type	frequency (Hz)	$\overline{\eta}_i$
1	(1,1)	162.38	0.12
2	(1,2)	322.58	0.00
3	(2,1)	489.32	0.00
4	(1,3)	589.58	0.22
5	(2,2)	649.52	0.00
6	(2,3)	916.51	0.00
7	(1,4)	963.38	0.00
8	(3,2)	1034.21	1.00
9	(3,1)	1194.41	0.00
10	(2,4)	1290.31	0.00

Table 3.5: Resonance frequencies of the plate.

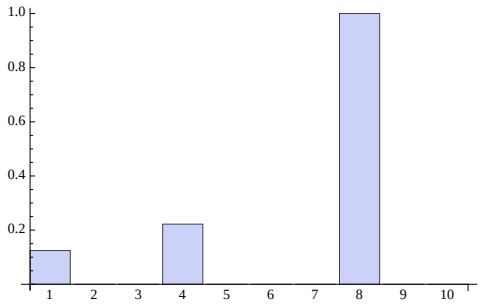

Figure 3.15: Normalized modal radiation coefficents η_i^{norm}

to be controlled is equal to three, there will be three groups transducers, each one composed by four piezoelectric patches connected in parallel. The dimensions of the considered piezo elements are listed in the appendix.
The modal controllabilities $\mathscr{M}_{in}(x_n, y_n)$ in function of the positioning of the patch for the considered vibrational modes is plotted in figure 3.16.

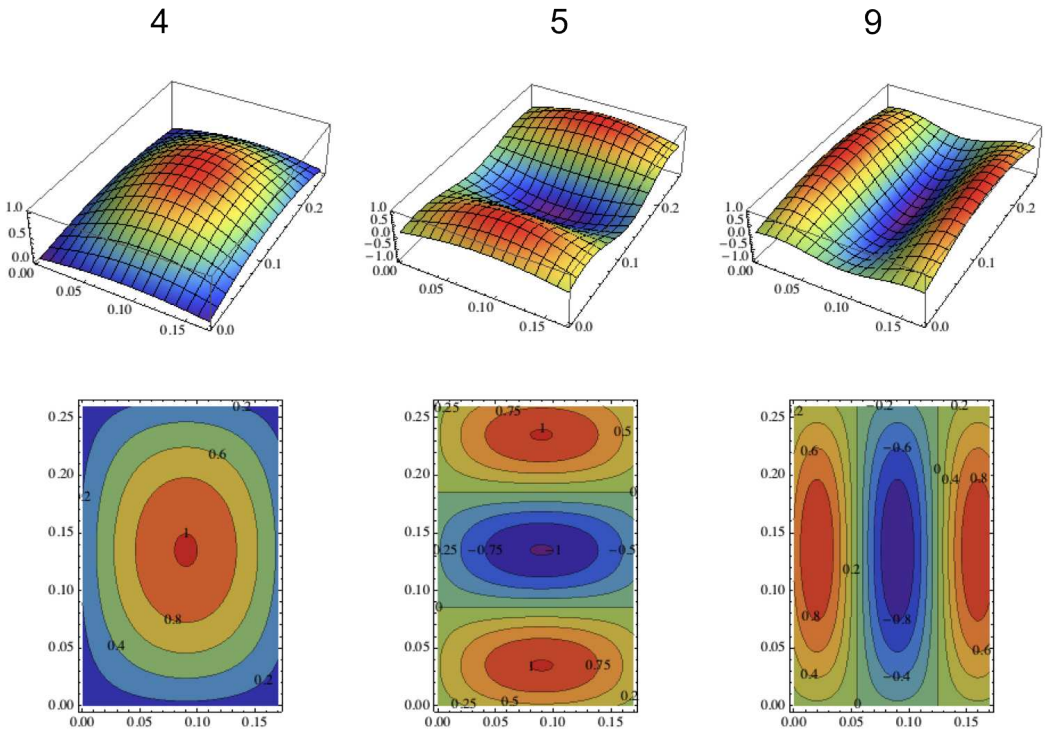

Figure 3.16: Modal Controllability $\mathscr{M}_{in}$ for the selected modes of a simply supported plate

The spatial controllability $\tilde{\mathscr{S}}_{in}$ and the acoustic controllability $\mathscr{A}_n$ for the simply supported plate and for the selected modes are plotted in figures 3.17 and 3.18 respectively.

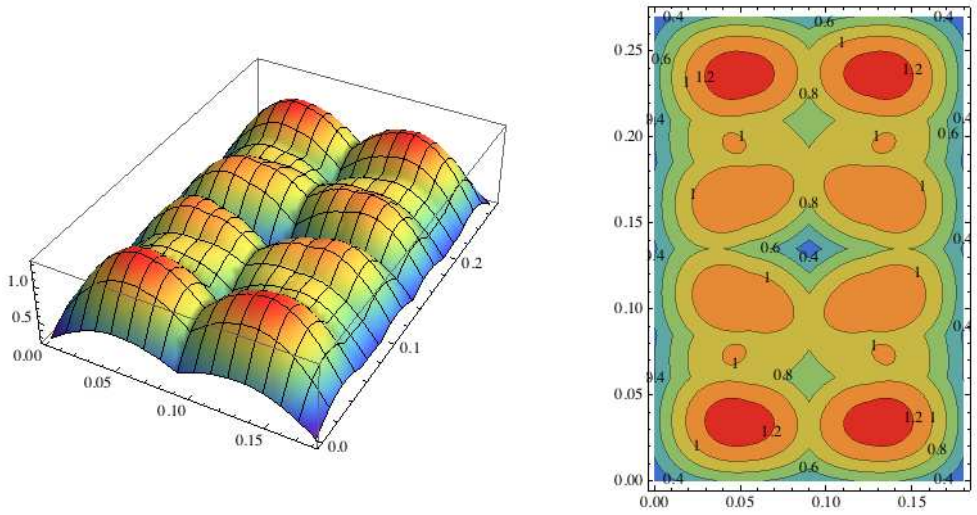

Figure 3.17: Reduced spatial controllability $\tilde{\mathscr{S}}_{in}$ of a simply supported plate

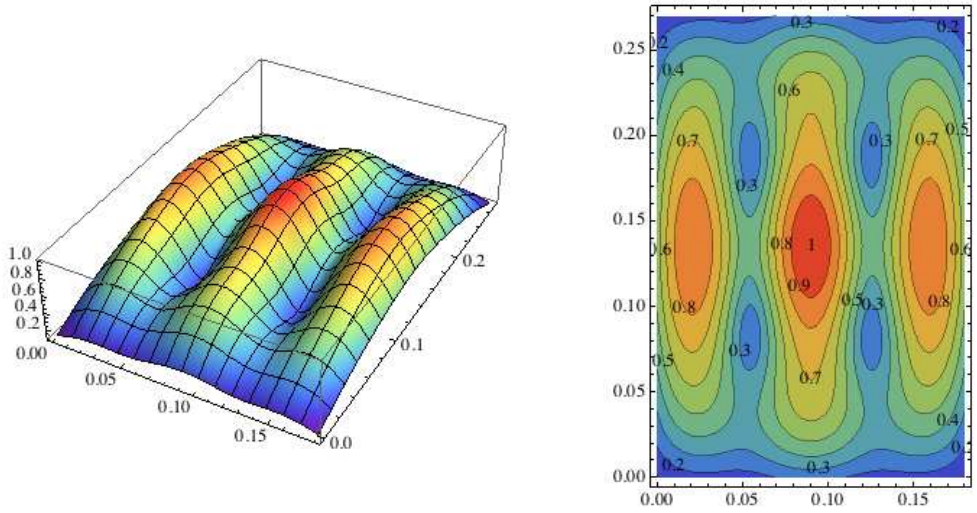

Figure 3.18: Acoustic controllability $\tilde{\mathscr{A}}_{in}$ of a simply supported plate

Obtaining a coupling matrix with rows as orthogonal as possible As stated in section 3.3.4, the *RL* network needs, for being performant, a coupling matrix $\mathbf{\Gamma}$ with the rows mutually orthogonal. In order to obtain this result without performing long and complex calculations, one can exploit the orthogonality of the vibration modes that have to be controlled and the symmetry of the structure. This can be done by optimizing the positioning of the transducers on a quarter of the plate, and then replicating this structure on the rest of the structure, connecting the corresponding patches in parallel. To this end small square piezoelectric patch will be considered for the optimization.

The constrained optimization procedure is:

$$\max_{(x_n,y_n)\in R^*} \mathscr{A}_n(x_n, y_n)$$
$$\text{subjected to } \mathscr{M}_{inr}(x_n, y_n) \geqslant .8, \text{ for at least one } i \in \chi_C$$

where R^* represents a quarter of a plate.
With this procedure we maximize the acoustic controllablity, while the modal controllability of each target mode is manteined over 80%.

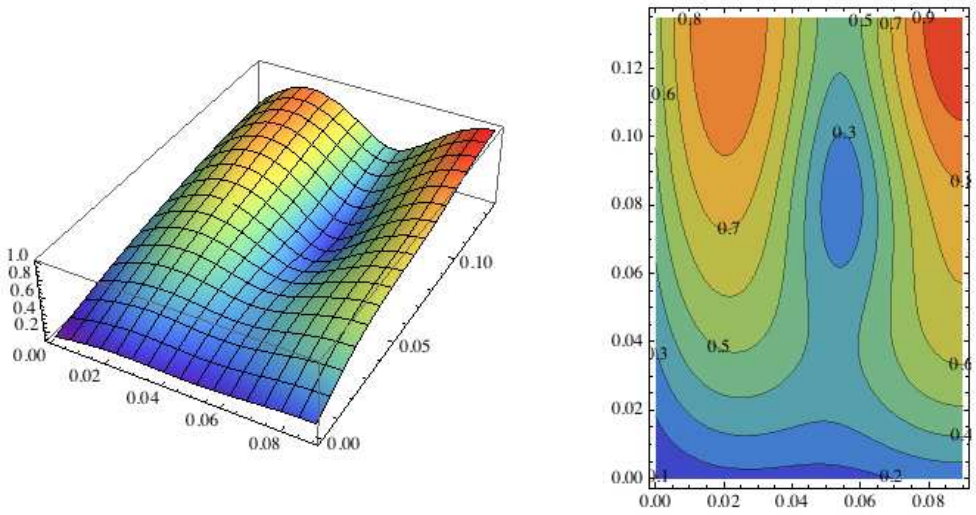

Figure 3.19: Acoustic controllability $\tilde{\mathscr{S}}_{in}$ of a simply supported plate limited to the set of points R^*

And the optimal placements, with respective values for the acoustic controllability and modal controllability are listed in table 3.6.

Patch	(x_n, y_n)	$\mathscr{A}_n$	$\mathscr{M}_{1n}$	$\mathscr{M}_{4n}$	$\mathscr{M}_{8n}$
1	$(0.0899, 0.1349)$	1.00	1.00	-1.00	-1.00
2	$(0.0899, 0.5548)$	0.67	0.67	0.80	-0.67
3	$(0.0211, 0.1349)$	0.89	-0.51	-0.51	0.99

Table 3.6: Optimal positioning and values of the Acoustical and Modal controllability.

As discussed in section, for optimizing the RL network control behaviour the patches are symmetrically disposed along the structure and connected in parallel,as shown in figure 3.20. This is the simplest way to assure a good condition for the diagonalization of the matrix of the couplings. A rendering of the final structure with the connections is in figure 3.21

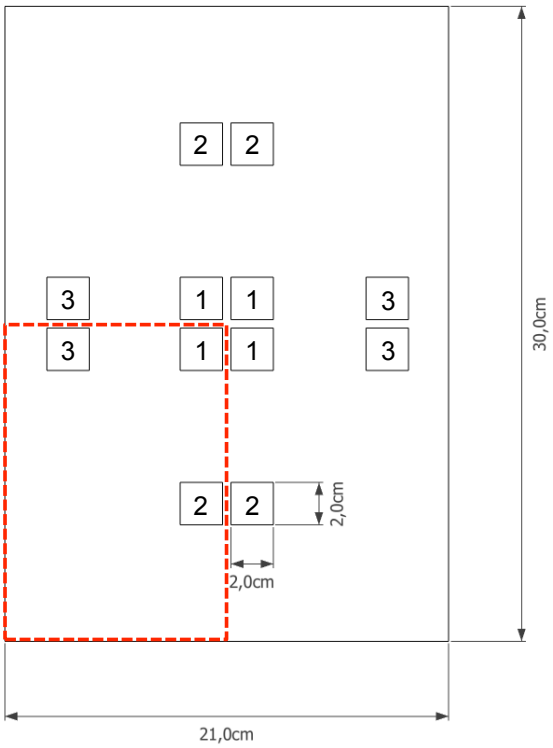

Figure 3.20: Optimal positioning for the piezoelectric patches groups

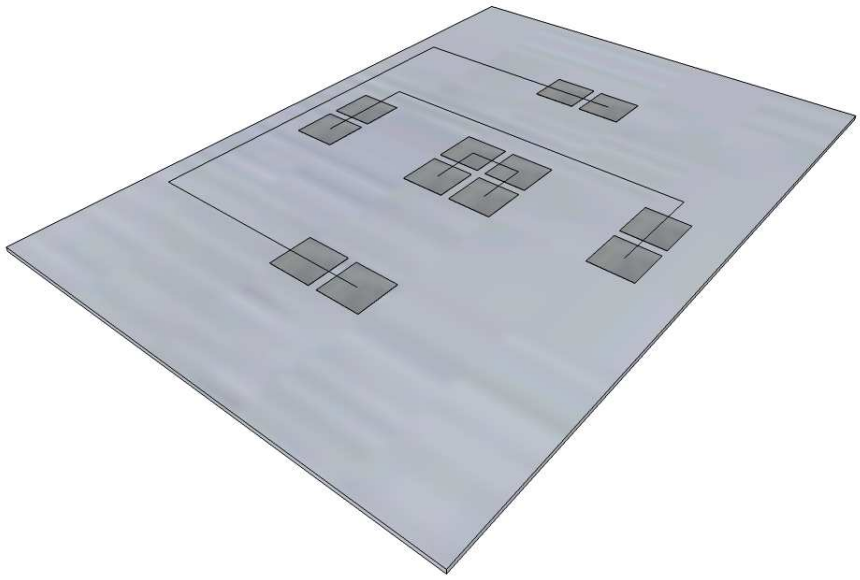

Figure 3.21: Rendering of the assembled structure.

3.5.3 Coupling coefficients

Using equation (3.73) and considering the optimal positions listed in table 3.6, the matrix of the normalized electromechanical couplings has this form:

$$\mathbf{\Gamma} = \begin{bmatrix} 0.16 & 0 & 0 & -0.16 & 0 & 0 & -0.150 & 0 & 0 \\ 0.11 & 0.16 & 0 & 0.13 & 0 & 0 & -0.10 & 0 & 0 \\ 0.08 & 0 & 0.14 & -0.08 & 0 & -0.14 & 0.150 & -0.10 & 0 \end{bmatrix}. \quad (3.86)$$

Since the target modes are only three, the reduced coupling matrix $\tilde{\mathbf{\Gamma}}$ that will be used for determining the controller is

$$\tilde{\mathbf{\Gamma}} = \begin{bmatrix} 0.16 & -0.16 & -0.15 \\ 0.11 & 0.13 & -0.10 \\ 0.08 & -0.08 & 0.150 \end{bmatrix}. \quad (3.87)$$

The best transformation matrix $\boldsymbol{U}$ to make $\mathscr{G} = \mathbf{\Gamma}\boldsymbol{U}$ is

$$\boldsymbol{U} = \begin{bmatrix} 0.6580 & -0.7384 & -0.1475 \\ 0.7266 & 0.5712 & 0.3817 \\ 0.1976 & 0.3583 & -0.9124 \end{bmatrix}, \quad (3.88)$$

and then the couplong matrix in the transformed space is

$$\mathscr{G} = \begin{bmatrix} 0.2010 & -0.0266 & -0.0546 \\ -0.0339 & 0.1580 & 0.1424 \\ -0.0557 & 0.1141 & 0.1972 \end{bmatrix}. \quad (3.89)$$

As expected, the matrix $\mathscr{G}$ is not diagonal, but the diagonal terms are one order of magnitude higher than most of the other terms, and this is sufficient for having good performances with the RL network.
The optimization of the RL network, and of all the other ciruits is based on the fixed point method. The parameters of all the circuits are listed in the appendix.

3.6 Results

In this section the results of the simulations are presented. The simulations have been realized using a Simulink model of the structure with the different types of control. All the FRF are calculated exciting the structure with an impact in a random point. The position of the point for measuring the velocity is chosen to excite and observe all modes in the frequency range of interest by avoiding nodal lines as more as possible. The impulse has a peak value F_0 of $1N$. The time of simulation T is equal to 5.24 s, thus the frequency resolution df is 0.1907 Hz. The simulation step size is set equal to 1/12500 s to avoid computation errors.

The first analysis that is performed concerns the velocity, and this is done in order to verify that the control systems are acting as expected. The FRF plots of the velocity is in figure 3.22. From the analysis of this first result it is clear how the RL network behaves better than the other control strategies, providing an average damping of more than $30dB$ on the controlled modes. The less per formant is the Current Flowing circuit, due to the presence of the additional capacity in the shunt, providing an average damping of $10dB$. The multiple RL shunt performs a trade off between the two other control strategies, providing a mean damping of $26dB$, close to the performances of the RL network.

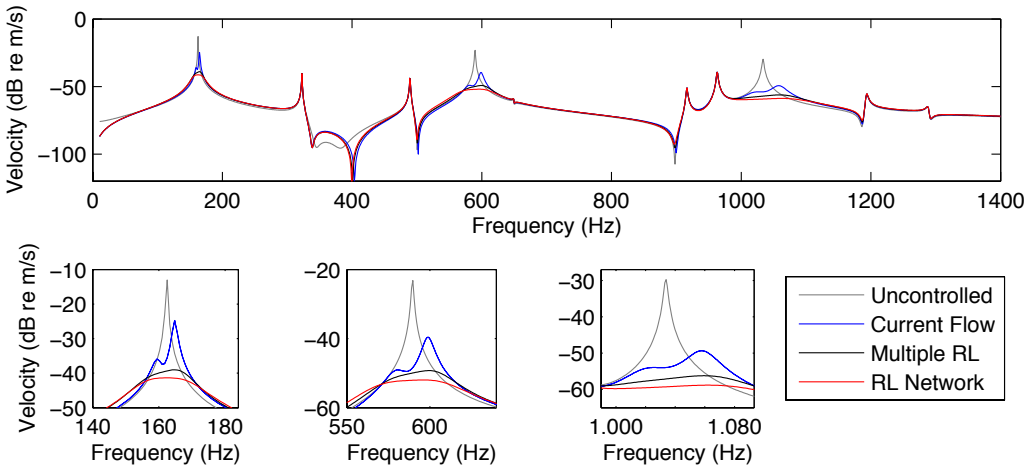

Figure 3.22: FRF of the velocity with different types of control.

The FRF plots of the mean pressure and sound power are plotted in figures 3.23 and 3.24 respectively. These two plots show that the prediction of the most radiating modes was correct, and shows the effectiveness of the controllers, in agreemment with the results obtained for the velocity field.

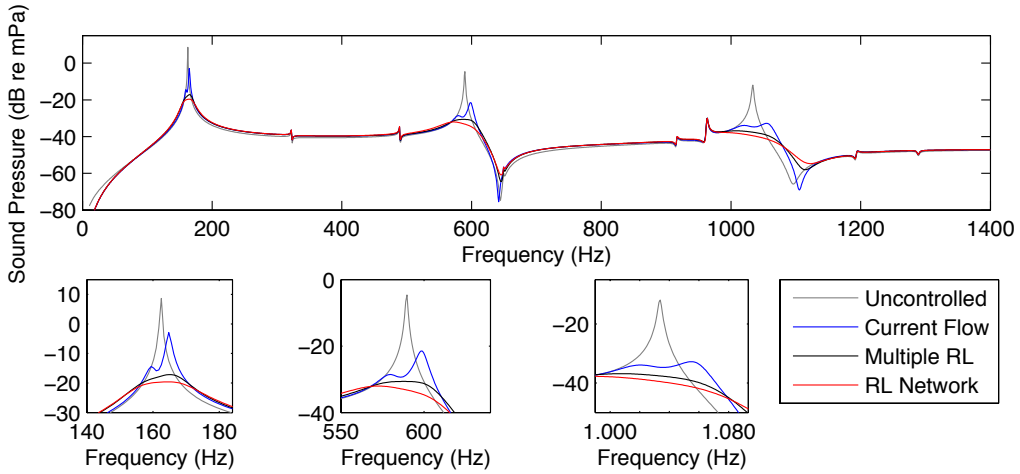

Figure 3.23: *FRF* of the radiated far field pressure with different types of control.

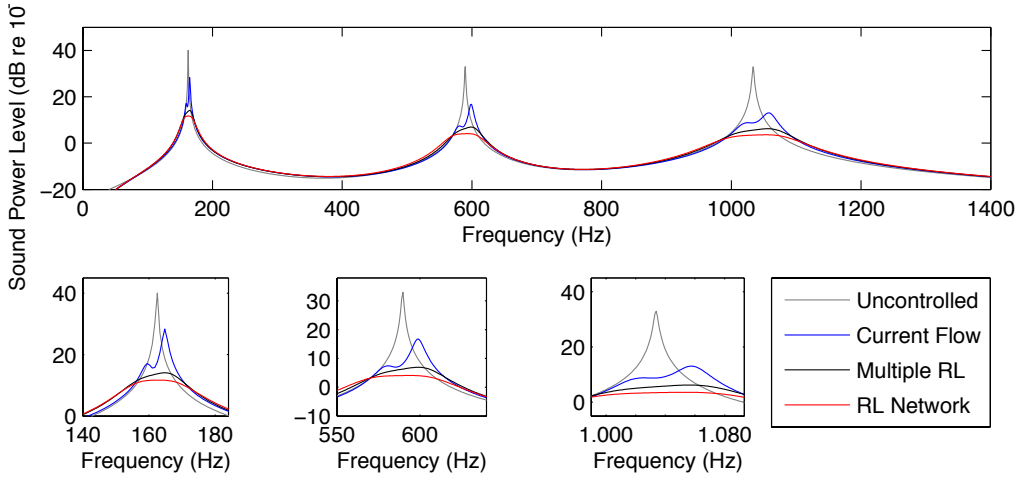

Figure 3.24: *FRF* of the radiated sound power with different types of control.

Remark 11. *The RL network is connected to all the transducers, and uses the ensemble of patch for damping each mode. On the contrary a multiple RL shunt is composed by independent circuit, each one connected to a single transducer. This means that if there is a problem with one piezo element, the multiple RL controller can entirely loose the control authority over a mode. For this reason too, the use of the RL network control system is then preferable.*

In order to show how well the mean far field sound pressure level is reduced, the transient response of the system is plotted in figure 3.25.

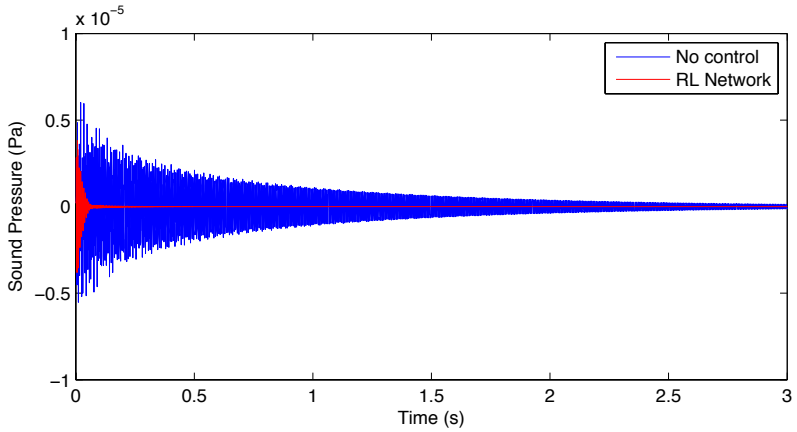

Figure 3.25: Mean far field sound pressure with RL network control

3.7 Conclusions

In this chapter the modelling and optimization of a piezoelectric smart plate is presented. This optimization is focused to the development of a smart structure for sound radiation and transmission control. Several different type of passive control techniques are presented, and a multi-modal technique is selected as the most convenient for the control purposes.
A novel optimization technique of the piezoelectric positioning, based on the control of the radiated sound power is also presented.
Resuming, the results obtained in this chapter are the following:

- a variational method for obtaining the modal equation of the structure is introduced
- the RL network has been chosen as the best one for passive control
- an optimization procedure for pzt transducer positioning and connection has been introduced

Chapter 4

Distributed control networks

Contents

Object of the Chapter

The object of this chapter is the application of distributed piezoelectric control network to the reduction of the sound radiation transmitted through and radiated by an aluminium panel immersed in a light fluid. An innovative Piezoelectric Resistive Electrode plate is modelled and optimized here. This structure consists of an aluminium plate entirely covered by two piezoelectric layers with a controlled resistivity electrode bonded on each free piezoelectric surface. The modelling, design and optimization of this structure is described in detail, and its acoustic behaviour is compared with that of different multi-modal distributed passive controllers.

4.1 Introduction and literature review

This chapter is about the application of distributed piezoelectric control system to the reduction of the sound power radiated and transmitted by thin plates. Different passive distributed control systems will be compared.

In section 4.2 the equations of motion for the piezoelectric plate will be derived, starting from kinematics of each layer, using the principle of virtual work and introducing the constitutive equations. Sections 4.3 and 4.4will be devoted to the optimization of the parameters in order to maximize the performances of the structure. The application of this novel system to the sound radiation and transmission control will be the object of the final part of this paper.

4.1.1 Literature review

A distributed circuit, or more in general a distributed control system, has the advantage of having an homogeneous spatial distribution, which can be exploited for conceiving a broad-band controller. In fact the most important problem when designing a localized controller, is the limited number of modes that can be controlled.

When considering a distributed approach it is still possible to distinguish from active and passive, or semi-passive, techniques. Active distributed systems are usally introduced for controlling large scale structures, with the aim of optimizing the way the system can detect the disturbance and counteract it. Several examples of this technique can be found in the literature [Baumann 2007, Elliott 1990, Elliott 2002, Elliott 2004, Elliott 2005, Frampton 2006, Serrand 2000, Gardonio 2005, Gardonio 2004]. However this is mainly an extension of the concepts used for localized control, and has the already cited problems of an active controller, expecially in terms of stability and power requirements.
A completely different approach for exploiting the uniform spatial distribution of sensors and actuators permits to have, with optimized electrical parameters, the duality between the electrical circuit and the mechanical structure. This duality traduces in the superposition of the electric and mechanic eigenfrequencies and in an optimal energy flow. This passive technique assures stability and optimized broadband control. Applications of this technique can be found in [Maurini 2005, dell'Isola 2003, Alessandroni 2004, Alessandroni 2002, Alessandroni 2005].

When considering discrete distributed systems, it is known from the literature [Maurini 2004] that there exist several optimal configurations for the electric circuit for optimizing the vibration damping through piezoelectric coupling. Being the piezoelectric transducers modelled as a capacitor in parallel with a current generator, inductors permit to have resonances in the

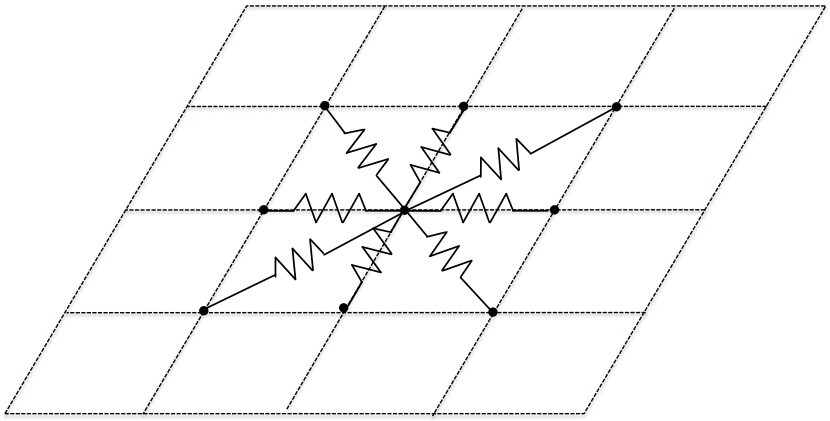

Figure 4.1: Optimal purely resistive interconnection for discrete distributed systems

electric circuit, but as the optimal value to assure the tuning is often too big for a passive realization, or even negative, they have to be simulated with active circuits. The use of purely resistive network can be a solution, by usually the coupling coefficient of the matrix of transducers is too low for having good results. The advantage in using distributive networks is that the spatial distribution of the electric elements makes the circuit able to adapt, in our case, the energy dissipation. Usually this optimal network is synthetized interconnecting a matrix of piezoelectric actuators with a passive network of resistors (figure 4.1). For the dimensions of the transducers smaller than the wavelength of the vibration propagating into the structure, this discrete system can be homogenized.

4.1.2 Objectives

The objectives of this chapter are

- model a distributed circuit that uses the principle of the "optimized resistance"
- optimization of the system
- test the performances in terms of sound radiation and transmission control

4.2 The model of PRE plate

The aim of this section is to derive the model of the PRE plate using a variational principle. We will start considering the geometry and the kinematics of the structure, then we will formulate the virtual work principle. Next we

will derive the constitutive equations for the PRE plate and, finally, obtain the equations of motion.

4.2.1 Geometry

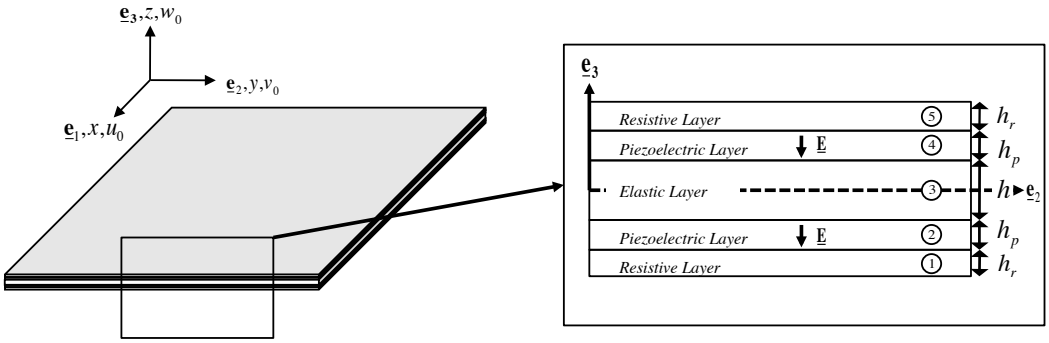

Figure 4.2: Geometry of the PRE plate

We consider a Kirchhoff-Love (K-L) plate with piezoelectric layers bonded on the two sides. The free surface of each piezoelectric layer is covered by a resistive layer, the other electrode is the aluminium plate itself. A schematic representation of the system is in figure 4.2. We assume that the plate is composed of a homogeneous and transversely isotropic material. Piezoelectric elements are polarized along the thickness. We identify the plate by its reference shape B. Let S be a flat surface, $\underline{e}_3$ the corresponding normal unit vector, $\underline{r}$ a generic vector in the plane of the plate and I an interval corresponding to the plate thickness.

We assume that

$$B = \{\underline{r} + z\underline{e}_3, \underline{r} \in S, z \in I\}.$$

Since the plate, figure 4.2, is composed of five layers we have that the interval I is naturally partitioned as $I = \bigcup_i I_i$. Consequently B is decomposed as $B = \bigcup_i B_i$, where B_3 is the elastic layer, B_2 and B_4 are piezoelectric layers, whilst B_1 and B_5 are resistive layers.
The following sets of indexes are considered:

$$i = \{1, 2, 3, 4, 5\}, \qquad l = \{2, 4\}, \qquad r = \{1, 5\}.$$

The value of intervals is (see figure 4.2 for the layer thickness definitions)

$$I_1 = \left[-\frac{h}{2} - h_p - h_r, -\frac{h}{2} - h_p\right], \qquad I_2 = \left[-\frac{h}{2} - h_p, -\frac{h}{2}\right],$$
$$I_3 = \left[-\frac{h}{2}, \frac{h}{2}\right], \qquad I_4 = \left[\frac{h}{2}, \frac{h}{2} + h_p\right],$$
$$I_5 = \left[\frac{h}{2} + h_p, \frac{h}{2} + h_p + h_r\right].$$

The boundary of B can be decomposed in the lateral boundary $\partial S \times I$ and in the upper and lower faces $S \times I^+$ and $S \times I^-$. Where $I^+ = \max[I_5]$ and $I^- = \min[I_1]$.

4.2.2 Kinematics

In this section the kinematic restrictions for each kind of layer will be introduced.

Kinematic restrictions for the elastic layer

According to the K-L plate theory, the following assumption for the displacement field is considered:

$$\underline{u}(x,y,z,t) = \underline{u}_0\,(x,y,t) + w_0(x,y,t)\underline{e}_3 - z\nabla w_0(x,y,t)$$

where w_0 is the transverse displacement,

$$\underline{u}_0\,(x,y,t) = u_0\,(x,y,t)\,\underline{e}_{\mathbf{1}} + v_0\,(x,y,t)\,\underline{e}_{\mathbf{2}}$$

is the displacement of the middle plane and the differential operator is defined as follows

$$\nabla = \frac{\partial}{\partial x}\underline{e}_{\mathbf{1}} + \frac{\partial}{\partial x}\underline{e}_2.$$

The corresponding strain field is

$$\mathbf{S}(\underline{u}_0, w_0) = \mathbf{S}_0(\underline{u}) - z\mathbf{S}_1(w_0),$$

where

$$\mathbf{S}_0(\underline{u}_0) = sym(\nabla \underline{u}_0), \quad \mathbf{S}_1(w_0) = sym(\nabla^2 w_0).$$

Kinematic restrictions for the piezoelectric layers

In each piezoelectric layer the assumptions for the electric potential $\varphi^{(l)}\,(x,y,z,t)$ and electric field $\underline{E}^{(l)}\,(x,y,z,t)$ are

$$\varphi^{(l)}\,(x,y,z,t) = \varphi_0^{(l)}\,(x,y,t) + z\varphi_1^{(l)}\,(x,y,t)\,, \tag{4.1}$$

$$\underline{E}^{(l)}\,(x,y,t) = -\text{grad}(\varphi^{(l)}) = -\frac{d\varphi^{(l)}}{dz}\underline{e}_3. \tag{4.2}$$

These conditions imply that, being $V^{(l)}$ the voltage at the interfaces between the piezoelectric and resistive layer, and being $\psi^{(l)} = \int V^{(l)} dt$ the flux linkage at the interfaces, the electric field is constant along the thickness and its value is

$$\underline{E}^{(l)} \cdot \underline{e}_{\mathbf{3}} = E_3^{(l)} = \varpi^{(l)} \frac{V^{(l)}}{h_p} = \varpi^{(l)} \frac{\dot{\psi}^{(l)}}{h_p}, \tag{4.3}$$

where the value of $\varpi^{(l)}$ depends on the polarization of the $l-th$ layer. As shown in figure 4.2 it is $\varpi^{(2)} = -1$ and $\varpi^{(4)} = 1$. A schematic diagram of voltage distribution along the thickness is displayed in figure 4.3.

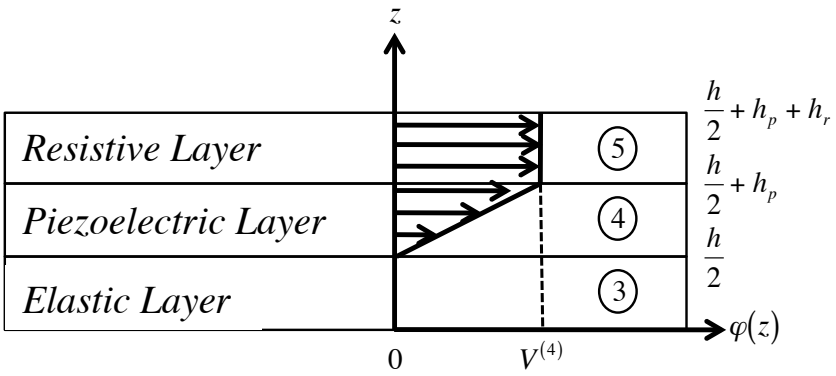

Figure 4.3: Voltage distribution along the thickness.

Kinematic restrictions for the resistive layers

For the resistive layer we suppose that the value of the voltage $V^{(l)}$ is constant along the thickness, so that $\partial V^{(r)}/\partial z = 0$. The kinematic at the interfaces between the elastic and piezoelectric layer are

$$V^{(1)} = V^{(2)}, \qquad V^{(4)} = V^{(5)},$$

and then

$$\dot{\psi}^{(1)} = \dot{\psi}^{(2)}, \qquad \dot{\psi}^{(4)} = \dot{\psi}^{(5)},$$

where $\dot{\square}$ denotes a partial time derivative.

4.2.3 Principle of virtual work and balance equations

According to the kinematic conditions introduced in section 4.2.2, in this section, a variational principle will be applied to the structure, in order to obtain balance equations and well-posed boundary conditions.

Internal work

In order to apply principle of virtual work a suitable expression for the internal energy must be found. Introducing $\mathbf{T}$, $\underline{D}$ and $\underline{J}$, as the stress tensor, the electric displacement vector and the current density vector, and defining by $\widetilde{\square}$ a virtual quantity, we can write the internal work L_{int} as

$$L_{int} = \underbrace{\delta E^m(\mathbf{T}(\underline{u}_0, w_0), \mathbf{S}(\tilde{\underline{u}}_0, \tilde{w}_0))}_{\text{Elastic energy}} + \underbrace{\delta E^e(\underline{D}(\psi), \tilde{\underline{E}}(\tilde{\psi}))}_{\text{Electric energy}} + \underbrace{L^d(\underline{J}(\psi), \nabla\tilde{\psi})}_{\text{Dissipated energy}}. \quad (4.4)$$

In equation (4.4) there are two conservative terms, the variation of elastic energy δE^m and the variation of the electric energy δE^e, and a non-conservative term L^d of the energy dissipated into each resistive layer by Joule heat. For the kinematic conditions introduced in each layer we have

$$\delta E^m = \int_S \int_I \mathbf{T}_\varphi : sym\left[\nabla\tilde{\underline{u}}_0 - z\nabla^2\tilde{w}_0\right], \quad (4.5)$$

$$\delta E^e = \int_S \int_I \frac{\underline{D} \cdot \underline{e}_3}{h_p} \tilde{V}, \tag{4.6}$$

$$L^d = \int_S \left(\sum_r \underline{J}^{(r)} \cdot \nabla \tilde{\psi} \right) h_r, \tag{4.7}$$

where $\mathbf{T}_\wp = \mathbf{T}\ (\mathbf{I} - \underline{e}_3 \otimes \underline{e}_3)$ is the projection of $\mathbf{T}$ on the plane perpendicular to $\underline{e}_3$. Introducing the terms

$$\mathbf{N} = \int_I \mathbf{T}_\wp, \qquad \mathbf{M} = \int_I -z\mathbf{T}_\wp, \qquad q = \int_I \frac{\underline{D} \cdot \underline{e}_3}{h_p},$$

we can write the final form for the internal energy

$$L_{int} = \underbrace{\int_S \mathbf{N} : sym(\nabla \tilde{\underline{u}}_0)}_{(a)} + \underbrace{\int_S \mathbf{M} : \nabla^2 \tilde{w}_0}_{(b)} + \underbrace{\int_S q\tilde{V}}_{(c)} + \underbrace{\int_S \sum_r \underline{J}^{(r)} \cdot \nabla \tilde{\psi} h_r}_{(d)}. \tag{4.8}$$

where (a) is the virtual work of the forces acting on the plane $(\mathbf{I} - \underline{e}_3 \otimes \underline{e}_3)$, (b) that of the bending moments, (c) that of the electric forces and (d) is the non conservative energy dissipated within each resistive layer.

External work

In order to apply the principle of virtual work we now have to define the work done by the external forces and electric entities on the virtual displacements. Introducing $\underline{b}$ and $\underline{f}$ as the body and surface forces acting on B including the acceleration forces we can write for the virtual work of a generic virtual displacement

$$L_{ext} = \int_B \underline{b} \cdot \tilde{\underline{u}} + \int_{\partial B} \underline{f} \cdot \tilde{\underline{u}}. \tag{4.9}$$

We now decompose the forces and the displacements in their respective conjugate quantities, this decomposition is summarized in table 4.1. With these

Table 4.1: Decomposition of external forces with respect to the conjugate virtual quantities.

	Force	Conjugate
Body	$\underline{b}_p = \sum_i \int_{I_i} \underline{b}$	$\tilde{\underline{u}}_0$
	$b_w = \sum_i \int_{I_i} \underline{b} \cdot \underline{e}_3$	$\tilde{w}_0$
	$\underline{b}_m = -\sum_i \int_{I_i} z\underline{b}$	$\nabla \tilde{w}_0$
Surface	$\underline{f}_p = \sum_i \int_{I_i} \underline{f}$	$\tilde{\underline{u}}_0$
	$f_w = \sum_i \int_{I_i} \underline{f} \cdot \underline{e}_3$	$\tilde{w}_0$
	$\underline{f}_m = \sum_i \int_{I_i} z\underline{f}$	$\nabla \tilde{w}_0$

assumptions the expression of the external work is

$$L_{ext} = \int_S [\underline{b}_p \cdot \underline{\tilde{u}}_0 + b_w \tilde{w}_0 + \underline{b}_m \cdot \nabla \tilde{w}_0] + \int_{\partial B} [\underline{f}_p \cdot \underline{\tilde{u}}_0 + f_w \tilde{w}_0 + \underline{f}_m \cdot \nabla \tilde{w}_0]. \quad (4.10)$$

Balance equations

The principle of virtual work states that

$$L_{int} = L_{ext}. \quad (4.11)$$

Considering equations (4.8) and (4.10), the balance equations on S can be obtained, preforming some integrations by parts, as

$$\nabla \cdot \mathbf{N} + \underline{b}_p = 0 \quad (4.12a)$$

$$\nabla^2 : (\mathbf{M}) + \nabla \cdot (\underline{b}_m) - b_w = 0, \quad (4.12b)$$

$$\dot{q}^{(2)} - \nabla \cdot \left(\underline{J}^{(1)} \right) h_r = 0, \quad (4.12c)$$

$$\dot{q}^{(4)} - \nabla \cdot \left(\underline{J}^{(5)} \right) h_r = 0, \quad (4.12d)$$

along with all boundary conditions on ∂B and $\partial (\partial B)$.

4.2.4 Constitutive equations

In this section the constitutive equations of each material used for building the plate are investigated. The aim is to derive the constitutive equations for the plate itself, that is $\mathbf{M}$, $\mathbf{N}$, $q^{(l)}$ as functions of the reduced strain parameters and the electric field.

Elastic plate constitutive equations

From the linear theory of elasticity we have, for the elastic layer

$$\mathbf{T} = \mathbb{C}\, \mathbf{S} \quad (4.13)$$

where $\mathbb{C}$ is the fourth order tensor of elasticity.

Piezoelectric constitutive equations

As for in section 3.2.3, and according to [IEEE 1987] the constitutive equations for a piezoelectric material are

$$\mathbf{T}_p = \mathbb{C}_p^E \mathbf{S}_p - \mathbf{e} \underline{E}, \quad (4.14a)$$

$$\underline{D} = \mathbf{e}^t \mathbf{S}_p + \varepsilon^S \underline{E}. \quad (4.14b)$$

Another equivalent form is obtained from the last equations

$$\mathbf{S}_p = \left(\mathbb{C}_p^E \right)^{-1} \mathbf{T}_p - \mathbf{d}\, \underline{E}, \quad (4.15a)$$

$$\underline{D} = \mathbf{d}^t\, \mathbf{S}_p + \varepsilon^T \underline{E}, \quad (4.15b)$$

where

$$\mathbf{e} = \mathbb{C}_p^E \mathbf{d}.$$

We will use these constitutive equations in the hypothesis of thin plates in plane stress and plane strain

Resistive electrode constitutive equations

In each resistive layer we have

$$\underline{J}^{(r)} = \sigma_r \underline{E}^{(r)},$$

the local form of the Ohm Law, in which σ_r is the specific conductivity $[\Omega^{-1}/m]$.
For the kinematic assumptions we have

$$\underline{E}^{(r)} = -\nabla V^{(r)},$$

and then

$$\underline{J}^{(r)} = -\sigma \nabla \dot{\psi}^{(r)} = -\frac{1}{\varrho_r} \nabla \dot{\psi}^{(r)}.$$

where ϱ_r is the specific resistivity $[\Omega m]$ of the material used for building the electrode.

PRE plate constitutive equations

In section 4.2.3 we defined the quantities $\mathbf{N}$, $\mathbf{M}$, q, $\underline{J}$. Now that we have introduced constitutive equations for each layer, we can find the PRE plate constitutive equations.

$$\mathbf{N} = \mathbb{K}_{Nu} \nabla \underline{u}_0 + k_{N\psi} \left(\dot{\psi}^{(4)} - \dot{\psi}^{(2)} \right), \tag{4.16a}$$

$$\mathbf{M} = \mathbb{K}_{Mw} \nabla^2 w_0 + \Gamma \left(\dot{\psi}^{(2)} + \dot{\psi}^{(4)} \right), \tag{4.16b}$$

$$q^{(2)} = -k_{N\psi} \nabla(\underline{u}_0) - \Gamma \nabla^2 (w_0) + C_p \dot{\psi}^{(2)}, \tag{4.16c}$$

$$q^{(4)} = k_{N\psi} \nabla(\underline{u}_0) - \Gamma \nabla^2 (w_0) + C_p \dot{\psi}^{(4)}, \tag{4.16d}$$

$$\underline{J}^{(1)} = -\frac{1}{\varrho_r} \nabla \dot{\psi}^{(2)}, \tag{4.16e}$$

$$\underline{J}^{(5)} = -\frac{1}{\varrho_r} \nabla \dot{\psi}^{(4)}, \tag{4.16f}$$

or in compact form

$$\begin{bmatrix} \mathbf{N} \\ \mathbf{M} \\ q^{(2)} \\ q^{(4)} \\ \underline{J}^{(1)} \\ \underline{J}^{(5)} \end{bmatrix} = \begin{bmatrix} \mathbb{K}_{Nu} & 0 & -k_{N\psi} & k_{N\psi} & 0 & 0 \\ 0 & \mathbb{K}_{Mw} & \Gamma & \Gamma & 0 & 0 \\ -k_{N\psi} & -\Gamma & C_p & 0 & 0 & 0 \\ k_{N\psi} & -\Gamma & 0 & C_p & 0 & 0 \\ 0 & 0 & 0 & 0 & -\frac{1}{\varrho_r} & 0 \\ 0 & 0 & 0 & 0 & 0 & -\frac{1}{\varrho_r} \end{bmatrix} \begin{bmatrix} \nabla(\underline{u}_0) \\ \nabla^2(w_0) \\ \dot{\psi}^{(2)} \\ \dot{\psi}^{(4)} \\ \nabla \dot{\psi}^{(2)} \\ \nabla \dot{\psi}^{(4)} \end{bmatrix} \tag{4.17}$$

where the coefficients are listed in table 4.2 and where we introduced $\xi_p = h_p/h$ as the ratio between the thickness of the piezoelectric layer and that of the elastic layer and

$$\alpha = 8\xi_p^3 + 12\xi_p^2 + 6\xi_p.$$

This parameter α which is related to the ratio between the thickness of the piezoelectric layer and the host plate will also appear in the stiffness terms of the PRE plate equations.

Table 4.2: Coefficients in Constitutive Equations

Coefficient	Value	Description
$\mathbb{K}_{Mw}$	$\frac{h^3}{12}\left[\mathbb{C}^E + \alpha\mathbb{C}_p^E\right]$	Bending Stiffness
Γ	$\frac{d_{31}Y_{pzt}h(\xi_p+1)}{2(1-\nu_p)}$	Bending Coupling
$\mathbb{K}_{Nu}$	$h(\mathbb{C}^E + 2\xi_p\mathbb{C}_p^E)$	Extensional Stiffness
$k_{N\psi}$	$\frac{d_{31}Y}{(1-\nu)}$	Extensional Coupling
C_p	$\frac{\varepsilon_{33}^S}{h_p}$	Capacitance

4.2.5 Equations of motion

From equations (4.12) and using equations (4.16) we have the complete form of the PRE plate equations

$$\mathbb{K}_{Nu}\nabla^2\underline{u}_0 + \nabla k_{N\psi}\left(\dot{\psi}^{(2)} - \dot{\psi}^{(4)}\right) + \underline{b}_p = 0, \tag{4.18a}$$

$$\mathbb{K}_{Mw}\nabla^4 w_0 + \Gamma\nabla^2\left(\dot{\psi}^{(2)} + \dot{\psi}^{(4)}\right) + \nabla\underline{b}_m - b_w = 0, \tag{4.18b}$$

$$-k_{N\psi}\nabla(\dot{\underline{u}}_0) - \Gamma\nabla^2\dot{w}_0 + C_p\ddot{\psi}^{(2)} - \frac{h_r}{\varrho_r}\nabla^2\dot{\psi}^{(2)} = 0, \tag{4.18c}$$

$$k_{N\psi}\nabla(\dot{\underline{u}}_0) - \Gamma\nabla^2\dot{w}_0 + C_p\ddot{\psi}^{(4)} - \frac{h_r}{\varrho_r}\nabla^2\dot{\psi}^{(4)} = 0. \tag{4.18d}$$

In common applications one can neglect $\underline{b}_m$, and then introduce the other forcing terms as

$$b_w = -\rho_t\ddot{w}_0 + f_{ext}, \tag{4.19}$$

$$\underline{b}_p = -\rho_t\ddot{\underline{u}}_0, \tag{4.20}$$

where the ρ_t is the overall surface mass density, calculated from the volume densities ρ_{pl} of the plate and ρ_{pz} of the piezoelectric material as follows:

$$\rho_t = \rho_{pl}h + \rho_{pz}h_p. \tag{4.21}$$

Moreover introducing the overall bending stiffness S_t as

$$S_t = \frac{h^3}{12}\left[\frac{Y}{1-\nu^2} + \alpha\frac{Y_p}{1-\nu_p^2}\right],$$

we have

$$\mathbb{K}_{Nu}\nabla^2\underline{u}_0 + \rho_t\ddot{\underline{u}}_0 + k_{N\psi}\nabla\left(\dot{\psi}^{(4)} - \dot{\psi}^{(2)}\right) = 0, \tag{4.22a}$$

$$S_t\nabla^4 w_0 + \rho_t\ddot{w}_0 + \Gamma\nabla^2\left(\dot{\psi}^{(4)} + \dot{\psi}^{(2)}\right) = f_{ext}, \tag{4.22b}$$

$$C_p\ddot{\psi}^{(2)} - \frac{h_r}{\varrho_r}\nabla^2\dot{\psi}^{(2)} - \Gamma\nabla^2(\dot{w}_0) - k_{N\psi}\nabla(\dot{\underline{u}}_0) = 0, \tag{4.22c}$$

$$C_p\ddot{\psi}^{(4)} - \frac{h_r}{\varrho_r}\nabla^2\dot{\psi}^{(4)} - \Gamma\nabla^2(\dot{w}_0) + k_{N\psi}\nabla(\dot{\underline{u}}_0) = 0. \tag{4.22d}$$

If we consider only bending vibration we have

$$\nabla^2 u_0 + \rho_{pz}\ddot{\underline{u}}_0 = 0$$

and so

$$\dot{\psi}^{(4)} = \dot{\psi}^{(2)} = \dot{\psi}. \tag{4.23}$$

This derives from the symmetry of the structure with respect to its mean plane, the so called bimorph configuration for the piezoelectric patches, and means that the extensional vibrations are uncoupled from the flux linkage. Then from additional equations, (4.22c) and (4.22d), and considering equation (4.23), the final form for the governing equations in terms of the transverse displacement and of the flux linkage is

$$S_t\nabla^4 w_0 + \rho_t\ddot{w}_0 + 2\Gamma\nabla^2(\dot{\psi}) = f_{ext}, \tag{4.24a}$$

$$C_p\ddot{\psi} - \frac{h_r}{\varrho_r}\nabla^2\dot{\psi} - \Gamma\nabla^2(\dot{w}_0) = 0. \tag{4.24b}$$

4.3 Dynamical Analysis

4.3.1 Wave propagation in a PRE plate

In order to investigate the electromechanical behaviour of the PRE plate, it is crucial to study the propagation of electrical and vibrational waves in the structure. This kind of analysis is the best way of determining how the smart structure is reacting to a mechanical input, such as a bending vibration, and how it changes its mechanical properties. To this end we suppose that the plate is infinite and that a bending wave with wave vector $\underline{k_r}$ is propagating in the plate. We can then easily decompose the state variables $w_0(x,y,t)$ and $\psi(x,y,t)$ as

$$\begin{bmatrix} w_0(x,y,t) \\ \psi(x,y,t) \end{bmatrix} = \begin{bmatrix} W(t) \\ \Psi(t) \end{bmatrix} e^{j\underline{k_r}\cdot\underline{r}}.$$

The system is then reduced as follows

$$S_t k_r^4 W + \rho_t \ddot{W} - 2\Gamma k_r^2 \left(\dot{\Psi}\right) = 0, \tag{4.25a}$$

$$C_p \ddot{\Psi} + \frac{h_r}{\varrho_r} k_r^2 \dot{\Psi} + \Gamma k_r^2 \dot{W} = 0, \tag{4.25b}$$

where $k_r = |\underline{k}_r|$.
A non-dimensional form of this system, where $\overline{\square}$ is a non dimensional quantity, is

$$\overline{W} + \ddot{\overline{W}} - 2\gamma \dot{\overline{\Psi}} = 0, \tag{4.26a}$$

$$\ddot{\overline{\Psi}} - \delta \dot{\overline{\Psi}} + \gamma \dot{\overline{W}} = 0. \tag{4.26b}$$

The non dimensional state variables in equations (4.26) are

$$\overline{W} = \frac{W}{l_0} \quad \overline{\Psi} = \frac{\Psi}{\psi_0}$$

where ψ_0 and $_0$ are the scaling flux linkage and the scaling displacement, and

$$\psi_0 = l_0 \sqrt{\frac{\rho_t}{C_p}}. \tag{4.27}$$

The non-dimensional electromechanical coupling γ and damping coefficient δ appearing in equations (4.26) are

$$\gamma = \frac{2\Gamma}{\sqrt{C_p S_t}}, \qquad \delta = \frac{h_r}{\varrho_r C_p} \sqrt{\frac{\rho_t}{S_t}}, \tag{4.28}$$

From equation (4.28) we can conclude that δ is independent of the wavenumber k_r.

4.3.2 Modal model for a simply supported plate

In this section a modal solution for the PRE plate equations (4.24) will be developed using Galerkin method. The electromechanical fields $w_0(x, y, t)$ and $\psi(x, y, t)$ are given by:

$$w_0(x, y, t) = \sum_{i=1}^{N} \eta_i(t) \phi_i(x, y), \tag{4.29a}$$

$$\psi(x, y, t) = \sum_{i=1}^{N} \chi_i(t) \phi_i(x, y), \tag{4.29b}$$

where $\eta_i(t)$ and $\chi_i(t)$ are Fourier coefficients of the eigenfunctions $\phi_i(x, y)$ defined by the eigenvalue problem

$$\nabla^4 \phi_i = \lambda_i^2 \phi_i, \tag{4.30}$$

along with proper boundary conditions for the displacement field and for the flux linkage.

It is important to underline that, in order to keep the electromechanical analogy, the boundary conditions for the electric field must be the analog of the mechanical ones. This implies that the potions of piezoelectric material close to constrained edges of the PEM plate, must be suitably shunted. From equation (4.30) we obtain the values for natural frequencies

$$\omega_i = \lambda_i \sqrt{\frac{S_t}{\rho_t}}.$$

Substituting equations (4.30) and (4.29) into equations (4.24), projecting on the given basis a non-dimensional modal form for equations (4.24), denoting with $\hat{\square}$ a quantity in frequency domain we obtain

$$\Omega_i^2 \hat{\eta}_i - \Omega^2 \hat{\eta}_i - j2\gamma\Omega\Omega_i \hat{\chi}_i = \hat{f}_i, \tag{4.31a}$$

$$-\Omega^2 \hat{\chi}_i + j\delta\Omega\, \hat{\chi}_i + j\gamma\Omega\Omega_i \hat{\eta}_i = 0. \tag{4.31b}$$

where the non-dimensional coupling and damping coefficients are the same as in equations 4.28 and circular frequencies Ω and Ω_i are given by

$$\Omega = \frac{\omega}{\Omega_0}, \quad \Omega_i = \frac{\omega_i}{\Omega_0} \tag{4.32}$$

where Ω_0 is a scaling circular frequency.

The non-dimensional state variables and forcing term in equations (4.31) are given by

$$\hat{\eta} = \frac{\eta}{l_0}, \quad \hat{\chi} = \frac{\chi}{\psi_0}, \quad \hat{f}_i = \frac{f_i}{F_0}.$$

with the scaling force given by

$$F_0 = l_0 \Omega_0^2 \rho_t. \tag{4.33}$$

From the second equation of system (4.31) we can obtain

$$\hat{\chi}_i = \frac{j\gamma\Omega\Omega_i}{\Omega^2 - j\delta\Omega\Omega_i} \hat{\eta}_i$$

and then, substituting into the first equation of system (4.31), we have

$$\Omega_i^2 \hat{\eta}_i - \Omega^2 \hat{\eta}_i + \frac{j\gamma\Omega\Omega_i}{\Omega^2 - j\delta\Omega\Omega_i} \hat{\eta}_i = \hat{f}_i.$$

Finally we have the expression of the Fourier coefficients $\hat{\eta}_i$ and $\hat{\chi}_i$

$$\hat{\eta}_i = \frac{\hat{f}_i}{\Omega_i^2 - \Omega^2 + \frac{j\gamma\Omega\Omega_i}{\Omega^2 - j\delta\Omega\Omega_i}},$$

$$\hat{\chi}_i = \frac{j\gamma\Omega\Omega_i \hat{f}_i}{(\Omega^2 - j\delta\Omega\Omega_i)\left(\Omega_i^2 - \Omega^2 + \frac{j\gamma\Omega\Omega_i}{\Omega^2 - j\delta\Omega\Omega_i}\right)}.$$

4.3.3 Optimization

When studying the behaviour of the system it is necessary to analyse both the transient response and the forced response. In order to do this we will introduce two different quantities: the decay rate $D(\delta, \gamma)$ for the transient response and the mobility function $H(\hat{\omega}, \delta, \gamma)$ for the forced response, defined as

$$D(\delta) = \min_{i=1,2,3} \left(\left| \mathrm{Re}\left(\lambda_i\right) \right| \right), \tag{4.34}$$

$$H(\Omega, \delta, \gamma) = \frac{j\Omega\hat{\eta}_i(\Omega, \delta, \gamma)}{\hat{f}_i}. \tag{4.35}$$

The parameter that will be optimized is the damping δ and the resulting value δ_{opt} will be used in equation (4.28) to determine the optimal value for the specific resistivity for a given thickness of the electrode.The piezoelectric layer thickness has been optimized maximizing the coupling coefficient γ with a total added mass constraint of 40%.

Transient response

In order to maximize the damping efficiency, a pole placement criterion will be used for finding the optimal value for δ_{opt} that maximizes $D(\delta)$. The system (4.26) is homogeneous, thus it admits exponential solutions

$$\begin{bmatrix} \overline{W} \\ \overline{\Psi} \end{bmatrix} = \begin{bmatrix} \overline{\overline{W}} \\ \overline{\overline{\Psi}} \end{bmatrix} e^{\lambda t}. \tag{4.36}$$

The Pole Placement criterion consists in finding the roots λ of system (4.26) imposing the wave solution (4.36) and then finding the value of δ which maximizes the decay rate. In order to maximize the damping efficiency a pole placement criterion will be used for finding the optimal value for δ.
Then, substituting into system (4.26):

$$\begin{bmatrix} 1+\lambda^2 & -\lambda\gamma \\ \lambda\gamma & \delta\lambda+\lambda^2 \end{bmatrix} \begin{bmatrix} \overline{\overline{W}} \\ \overline{\overline{\Psi}} \end{bmatrix} e^{\lambda t}$$

then the characteristic polynomial is

$$\lambda^4 + \delta\lambda^3 + \left(1+\gamma^2\right)\lambda^2 + \delta\lambda = 0. \tag{4.37}$$

The three roots of this polynomial, neglecting the trivial solution $\lambda = 0$, are a non-positive real root ($\lambda_1 = -c \leq 0$) and a pair of complex conjugate roots ($\lambda_{2,3} = -a \pm jb,\ a \geq 0$) functions of the electric parameter δ. It is now possible to define the decay rate as

$$D(\delta) = \min_{i=1,2,3} \left(\left| \mathrm{Re}\left(\lambda_i\right) \right| \right)$$

With these assumpitons the characteristic polynomial is then

$$\lambda^3 + (2a + c)\,\lambda^2 + \left(a^2 + b^2 + 2ac\right)\lambda + \left(a^2 + b^2\right)c = 0 \tag{4.38}$$

Then, imposing the form (4.38) to equation (4.37) we obtain

$$2a + c = \delta \tag{4.39a}$$
$$\left(a^2 + b^2 + 2ac\right) = \left(1 + \gamma^2\right) \tag{4.39b}$$
$$\left(a^2 + b^2\right)c = \delta \tag{4.39c}$$

The elimination of b and δ leads to

$$a = \gamma^2 \frac{c}{2\left(1 + c^2\right)} < c$$

where the inequality holds because $\gamma \leq 1$, [Maurini 2005]. This means that the minimization of the decay rate is equivalent to the minimization of a Then eliminating b and c from the system (4.39) leads to

$$F(a, \delta) = 2a\left(1 + 4a^2 + \gamma^2 + \delta^2\right) - \left(8a^2 + \gamma^2\right)\delta = 0 \tag{4.40}$$

Applying the implicit function theorem, the derivative of a in function of δ can be calculated as

$$\frac{da}{d\delta} = -\frac{F_\delta(a, \delta)}{F_a(a, \delta)} = \frac{8a^2 + \gamma^2 - 4a\delta}{16a^2 - 16a\delta + 2\left(1 + 4a^2 + \gamma^2 + \delta^2\right)}.$$

It is now possible to find the maximum of a in function of δ:

$$\frac{8a^2 + \gamma^2 - 4a\delta}{16a^2 - 16a\delta + 2\left(1 + 4a^2 + \gamma^2 + \delta^2\right)} = 0,$$

for

$$a_{\max} = \frac{1}{4}\left(\delta_{opt} - \sqrt{-2\gamma^2 + \delta_{opt}^2}\right).$$

Substituting this value into equation (4.40) the optimum value for δ is obtained:

$$\delta_{opt}^{PP} = 1 + \frac{\gamma^2}{2},$$

for which it is

$$D_{opt} = \frac{\gamma^2}{4}.$$

Since δ is independent of the wavenumber k_r, the optimal damping condition

holds for each wavenumber, and leads to the optimal value for the resistance

$$\varrho_{opt} = \frac{h_r}{C_p}\sqrt{\frac{\rho_t}{S_t}}.$$

Forced response

Using the results obtained in section (4.3.2) it is easy to determine the mobility function , defined as

$$H(\Omega,\delta,\gamma)=\frac{j\Omega}{\Omega_i^2-\Omega^2+\frac{j\gamma\Omega\Omega_i}{\Omega^2-j\delta\Omega\Omega_i}},.$$

For optimizing the forced response a widely adopted approach consists in minimizing the $\infty-norm$ of the mobility function, defined as

$$||H(\Omega,\delta,\gamma)||_\infty=\sup_{\Omega\in R}|H(\Omega,\delta,\gamma)|.$$

It is known in the literature, see [Den Hartog 1956], that in coupled systems there exists a so-called fixed point $F=(\Omega_F,|H(\Omega_F,\delta,\gamma)|)$ defined as follows

$$\forall\overline{\gamma}\in R^+\quad\exists\,\Omega_F\;/\;\forall\delta_1,\delta_2\in R^+\quad|H(\Omega_F,\delta_1,\overline{\gamma})|=|H(\Omega_F,\delta_2,\overline{\gamma})|. \tag{4.41}$$

This point corresponds to the circular frequency

$$\Omega_F(\gamma)=\sqrt{1+\frac{\gamma^2}{2}}.$$

Imposing that the maximum of $|H(\Omega,\delta,\gamma)|$ is at Ω_F we find the optimal value for δ:

$$\frac{\partial}{\partial\Omega}|H(\Omega_F,\delta,\gamma)|\bigg|_{\Omega=\Omega_F}=0\Rightarrow\delta_{opt}^{FP}=\sqrt{\frac{8+10\gamma^2+3\gamma^3}{8+2\gamma^2}}\simeq 1+\frac{\gamma^2}{2}.$$

The last approximation holds because γ is small, in practical situations it is

$$0<\gamma<0.3. \tag{4.42}$$

As expected, $\delta_{opt}^{PP}\simeq\delta_{opt}^{FP}$ so the two criteria give the same result.

Effect of parameter variations

The plots in figure 4.4 show the decay rate and mechanical mobility as functions of the percentage variations of the parameter δ with respect to the optimum value δ_{opt}. Both plots show that relatively high variations of δ near the optimum value do not affect very much the overall behaviour and the damping performances of the structure. This because, as shown in the plots, the derivatives of both curves calculated for $\Delta\delta/\delta_{opt}$ are horizontal.

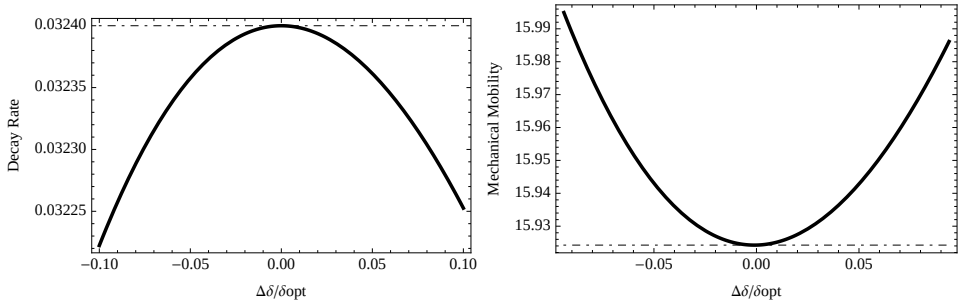

(a) Decay Rate (b) Mechanical Mobility $||H||_\infty$

Figure 4.4: Plot of the performance indexes of the two optimization methods as a function of damping δ.

4.4 Acoustic Analysis

4.4.1 Acoustic performance indices

As a complement of what done in chapter 2, the main performance indices for testing the acoustic properties of a thin structure are here resumed.
Let us consider an Euclidean space with its basis $(\underline{e}_1, \underline{e}_2, \underline{e}_3)$. We denote a generic point of the plate by $\underline{r} = x\underline{e}_1 + y\underline{e}_2$ and a generic point in the space as $\underline{p} = x\underline{e}_1 + y\underline{e}_2 + z\underline{e}_3$. The plate separates two identical light fluid media with density ρ.

Far Field Pressure The pressure $\widehat{p}(\underline{p}, \omega)$ in the generic point of the space due to the motion of a portion S of the plate can be calculated using the Rayleigh formula:

$$\widehat{p}(\underline{p}, \omega, S) = \frac{j\omega\rho}{2\pi} \int_S \frac{e^{-jk(\underline{p}-\underline{r})}}{\underline{p}-\underline{r}} \widehat{w}_0(\underline{r}, \omega) dS, \tag{4.43}$$

as explained in [Cremer 1973, Fahy 2001, Filippi 1984].
This is a very important performance index, since it is related to a physical quantity that can be easily measured, such as the pressure. In the literature there exists a standard method for measuring this quantity, see [ISO 3745 1977].

Radiated power at the plate level The radiated power π_r at the plate level can be expressed by the surface integral of the product between the pressure in each point of the plate, calculated with equation (4.43), multiplied by its velocity:

$$\pi_r(\omega, S) = \frac{1}{2} \int_S Re\left\{(\hat{p}(\underline{r}, \omega)|_{z=0}) \cdot (j\omega\hat{w}_0(\underline{r}, \omega))^*\right\} dS, \tag{4.44}$$

where $\square^*$ is a conjugate quantity.
This is a global parameter that gives us different informations with respect to the far field pressure, since it involves also the near field, but it is not a measurable quantity.

Sound Reduction Index Sound transmission through a panel is usually studied in the literature by considering an infinite plate, see [Cremer 1973, Fahy 2001, Filippi 1984]. This approximation is based on the fact that for higher frequencies the wavelength of the bending vibrations is much smaller than the characteristic dimension of the structure. Then we consider two semi-infinite sound media separated by an infinite plate placed at $z = 0$.
The wave propagating in the two media must satisfy the wave equation

$$\nabla^2 \hat{p}_n(\underline{r}, z, \omega) + \frac{1}{c^2}\hat{p}_n(\underline{r}, z, \omega) = 0, \quad n = 1, 2, \tag{4.45}$$

where c is the speed of sound in the medium.
We now introduce the incident power on a surface S as

$$\pi_i(\theta, \omega, \phi, S) = \frac{1}{2}\int_S Re\left\{(\hat{p}_1(\underline{p}, \omega)|_{z=0}) \cdot (j\omega\hat{w}_0(\underline{r}, \omega))^*\right\} dS, \tag{4.46}$$

where θ and ϕ the angles that the wave vector of the incident wave forms with $\underline{e}_1$ and $\underline{e}_2$, respectively; for the sake of simplicity we will consider $\phi = 0$ without loss of generality. We can define, using equation (4.44), the transparence function by

$$\tau(\theta, \omega) = \frac{\pi_t}{\pi_i}. \tag{4.47}$$

This function represents the fraction of the incident power that actually passes through the plate. When testing the acoustical behaviour of a structure, a standard parameter used is the Sound Reduction Index:

$$SRI(\theta, \omega) = 10 \log\left(\frac{1}{\tau(\theta, \omega)}\right). \tag{4.48}$$

4.4.2 Simulations

In this section some numerical simulations are considered, in order to show the performances of the control system, compared with two other passive control strategies: a plate with an attached viscoelastic layer and a Piezo Electro Mechanical (PEM) plate.
The viscoelastic plate is composed by an aluminium plate with an attached viscoelastic layer. Following [Cremer 1973], the thickness of the viscoelastic layer has been chosen equal to h. The material used in simulations is a 3M ISD 112. This structure represents the most simple way to introduce frequency independent damping.
The PEM plate is a smart structure composed by an aluminium plate

with a distributed matrix of piezoelectric transducers, interconnected by a passive modular network of inductors and resistors which assures a frequency independent damping. An accurate description of the system is in [Alessandroni 2004] and the system is described by the following system of equations:

$$S_t^{PEM}\nabla^4 w_0 + \rho_t^{PEM}\ddot{w}_0 + 2\Gamma^{PEM}\nabla^2(\dot{\psi}) = f_{ext}, \tag{4.49a}$$

$$\beta^{PEM}\nabla^4\psi + C_p^{PEM}\ddot{\psi} - \delta^{PEM}\nabla^2\dot{\psi} - \Gamma^{PEM}\nabla^2(\dot{w}_0) = 0. \tag{4.49b}$$

where β is a tuning coefficient due to the presence of the inductors. As we can see form equations (4.49) there is the duality between the mechanical and electrical equations, since both equations have the same differential poerators.
This structure uses the equivalent amount of piezoelectric material as a PRE plate. It is important to denote that, being the PEM plate a discrete structure, the size of each transducer must be smaller than the considered wavelengths. Consequently the number of connections needed increases with the maximum frequency of interest, that is the main trade off of this control technique, along with the problems related to mistuning.
All plots presented in previous sections have been realized considering a rectangular plate made of aluminium having the characteristics presented in appendix A.2.

Far Field Pressure According to [ISO 3745 1977] the far field sound pressure can be estimated using the pressure calculated in 10 points optimally placed in an hemisphere. We can use equation (4.43) to determine the sound pressure on these points, and then we consider the mean value in order to have a global parameter for the far field sound radiation. A numerical method is proposed in [Bai 2002] and will be applied to calculate the sound pressure. In figure 4.5 the mean pressure field radiated by a PRE plate is compared with those of an aluminium plate without control, a viscoelastic plate and a PEM plate. The PRE plate provides a considerable reduction of the mean value of the far field pressure near the peaks introduced by the most radiating structural modes and introduces more damping than a viscoelastic plate. The PEM plate is more efficient, and this was to be expected since it introduces electrical resonances for each mode maximizing the dissipated energy.

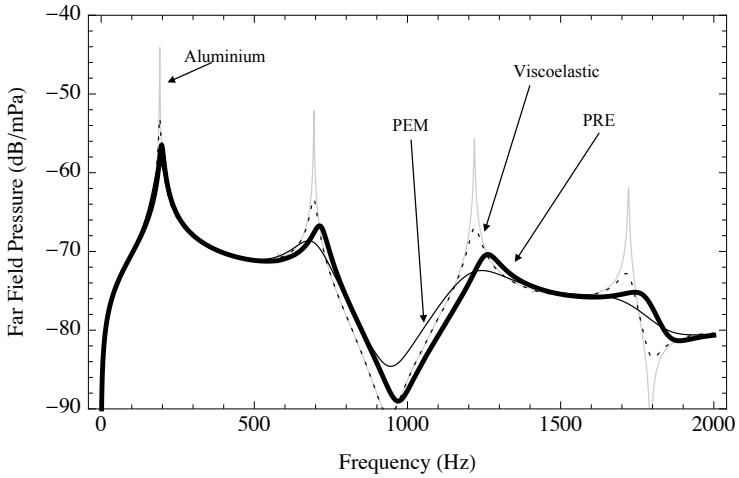

Figure 4.5: Far Field Pressure of an Aluminium plate, a PRE Plate, a PEM plate and a plate with viscoelastic treatment.

Radiated power at the plate level This analysis is performed on a finite simply supported plate. The acoustic power W on the surface of the plate can be expressed equation (4.44). Since from the modal model, section 4.3.2, we know the distribution of the velocity field in each point of the structure we can use equation (4.43) to obtain an expression of the radiated power which depends only on that known velocity field.
This integral will be calculated in a numerical way, using the method introduced in [Elliott 1993] and then slightly modified in [Bai 2002] with the results from [Borgiotti 1994]. The idea is to divide the structure into a matrix of $M = n \times n$ elementary elements, radiating as pistons, in order to extract from the geometry of the structure some of its acoustic properties. In figure 4.6 the radiated sound power plot for a finite simply supported plate is shown. Also with this performance parameter we can see how the control system is optimized for each radiating structural modes and the results are in line with those obtained for the far field sound pressure.

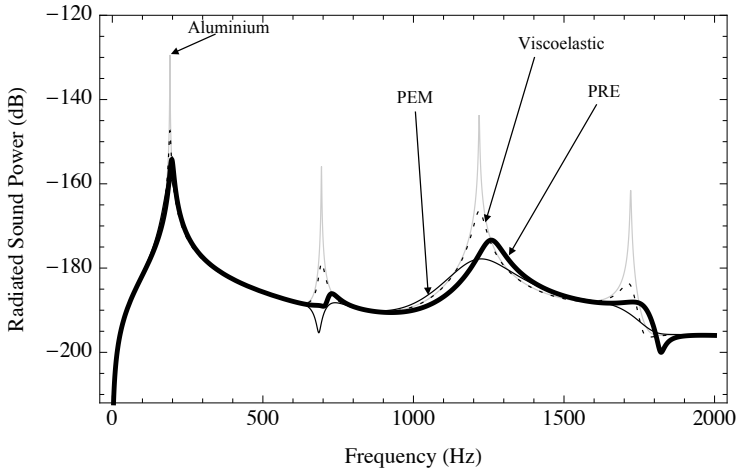

Figure 4.6: Radiated sound power of an Aluminium plate, a PRE Plate, a PEM plate and a plate with viscoelastic treatment.

Sound Reduction Index For finding the SRI we need the solution of equations (4.45) together with equations (4.24) when considering $f_{ext} = p_1 - p_2$ and the following continuity conditions

$$\frac{\partial p_n}{\partial z}|_{z=0} = -\rho \ddot{w}_0, \quad n = 1, 2. \tag{4.50}$$

The scaling quantities are listed in the Appendix. As discussed in section 4.3.1 we can use the wave equation as solution of this coupled system, in the form

$$\begin{bmatrix} \hat{w}_0(\underline{r}, \Omega) \\ \hat{\psi}(\underline{r}, \Omega) \\ \hat{p}_1(\underline{r}, z, \Omega) \\ \hat{p}_2(\underline{r}, z, \Omega) \end{bmatrix} = \begin{bmatrix} \hat{W}(\Omega) & 0 & 0 \\ \hat{\Psi}(\Omega) & 0 & 0 \\ 0 & \hat{P}_i(\Omega) & \hat{P}_r(\Omega) \\ 0 & \hat{P}_t(\Omega) & 0 \end{bmatrix} \begin{bmatrix} 1 \\ e^{-j\hat{k}_z \hat{z}} \\ e^{j\hat{k}_z \hat{z}} \end{bmatrix} e^{j\underline{\hat{k}_r} \cdot \underline{\hat{r}}}, \tag{4.51}$$

where

$$\hat{k}_z = \Omega \cos\theta, \qquad |\underline{\hat{k}_r}| = \hat{k}_r = \Omega \sin\theta, \tag{4.52}$$

and where θ is the angle of the incident wave.
Considering the solution (4.51), considering $f_{ext} = p_1 - p_2$ and equation (4.45) , system (4.24) becomes

$$\hat{k}_r^4 \hat{W} - \Omega^2 \hat{W} - 2\gamma j \Omega \hat{k}_r^2 \hat{\Psi} = \hat{P}_i + \hat{P}_r + \hat{P}_t \tag{4.53a}$$

$$-\Omega^2 \hat{\Psi} + \delta j \Omega \hat{k}_r^2 \hat{\Psi} + \gamma j \Omega \hat{k}_r^2 \hat{W} = 0 \tag{4.53b}$$

$$j\hat{k}_z(\hat{P}_r + \hat{P}_r) = \zeta \Omega^2 \hat{W} \tag{4.53c}$$

$$j\hat{k}_z \hat{P}_t = \zeta \Omega^2 \hat{W} \tag{4.53d}$$

From equations (4.46), (4.47), (4.48), (4.53), and considering conditions (4.52), we have

$$SRI(\theta,\Omega) = 10\log\left(\frac{\left|\hat{k}_r^4 - \Omega^2 + \dfrac{2\gamma^2\Omega^2\hat{k}_r^4}{j\delta\Omega\hat{k}_r^2 - \Omega^2} + \dfrac{2\zeta\Omega^2}{jk_z}\right|^2}{\Omega^2\dfrac{4\zeta}{\cos\theta}}\right)$$

.

In figure 4.7 the Sound Reduction Index for an aluminium plate, a PRE plate, a viscoelastic plate and a PEM plate are shown. Since all considered control systems control system are based on damping, no enhancement is possible in the region controlled by mass, below the critical frequency f_{cr}, where for the selected structure $f_{cr} = 5600Hz$. A detailed definition of f_{cr} is in [Filippi 1984]. Above the critical frequency, since both PRE and viscoelastic controls are frequency independent, there is a linear enhancement and the performances of the PRE plate are better than both those of a standard viscoelastic plate and of a PEM plate.

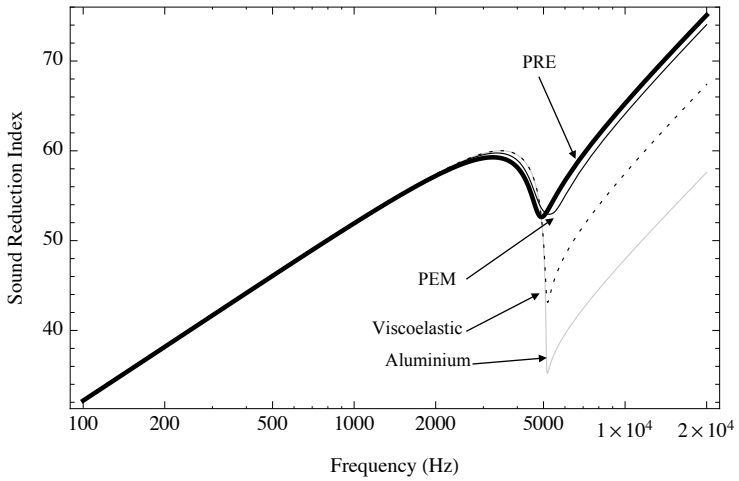

Figure 4.7: SRI of an Aluminium plate, a PRE Plate, a PEM plate and a plate with viscoelastic treatment.

Effect of parameter variations

Hence when considering industrial applications, the incertitudes in the thickness of the resistive layer h_r or of its resistivity ϱ_r introduced by the industrial process, will not compromise the behaviour of the PRE plate. On the other hand, when considering control strategy based on resonant effects, such as those presented in [Carneal 2004, Behrens 2003, Lee 1999b, Zhang 2004, Ozer 2003, Batra 2005] as well as in [Maurini 2005, dell'Isola 2003, Alessandroni 2004, Alessandroni 2002], the

sensitivity with respect to the tuning parameter is very high, and this is one of the main problems when considering industrial applications of these kind of structures.

As an example the effect of small variations of the tuning parameter β on the performances of a PEM plate on a target mode and on the sound reduction index are plotted in figure 4.9. As a consequence of the results obtained in section 4.3.3, small variations of the damping parameter δ do not affect very much the quality of the control. In figure 4.8 we have plotted the effect of the variation of δ on the three performance indices.

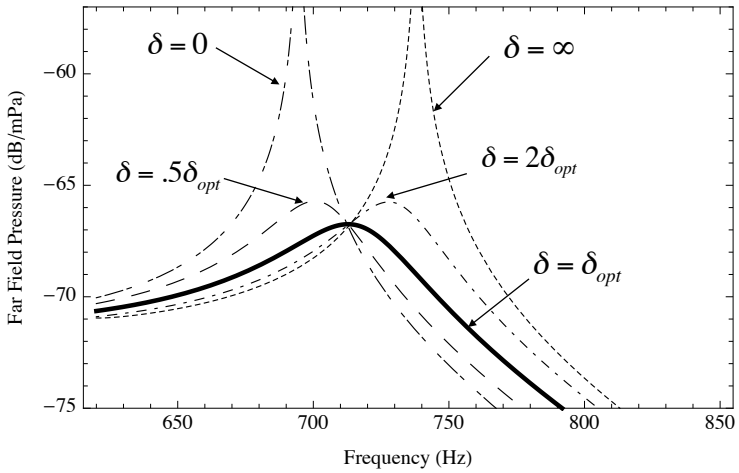

(a) Far Field Pressure

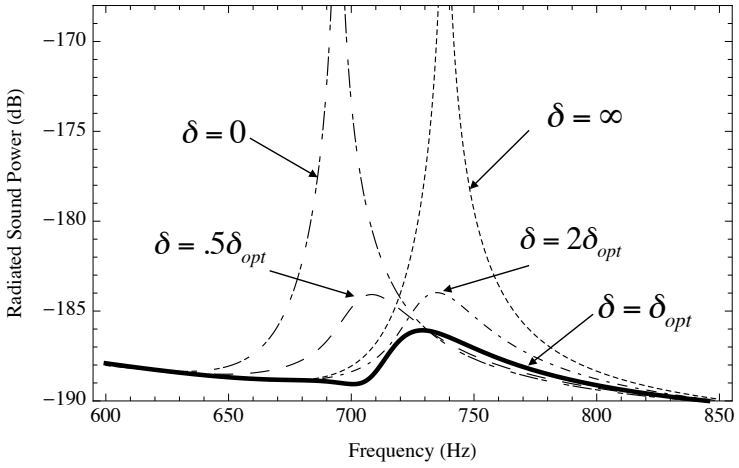

(b) Radiated Sound Power

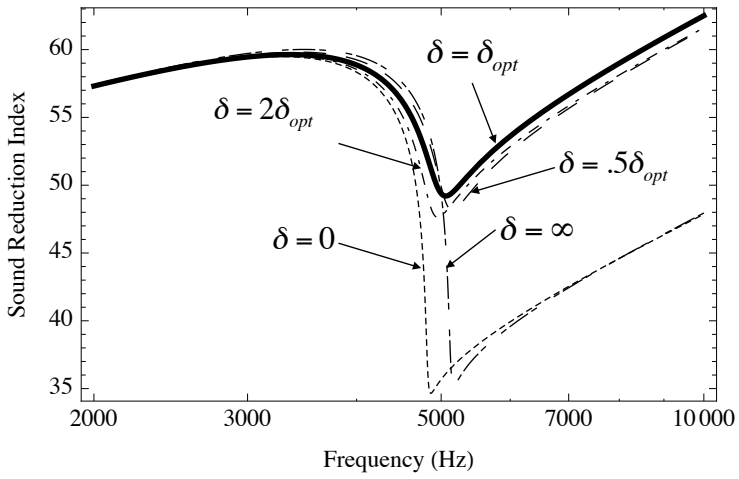

(c) Sound Reduction Index

Figure 4.8: Sound Radiation Index, Radiated Sound Power and Far Field Pressure for a PRE plate as a function of δ.

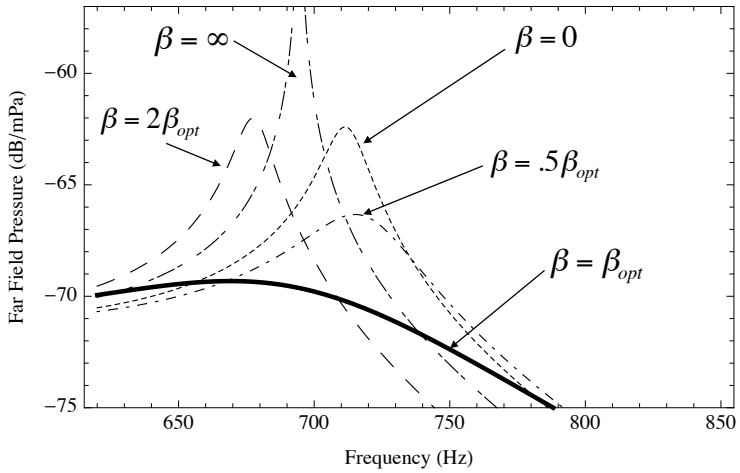

(a) Far Field Pressure

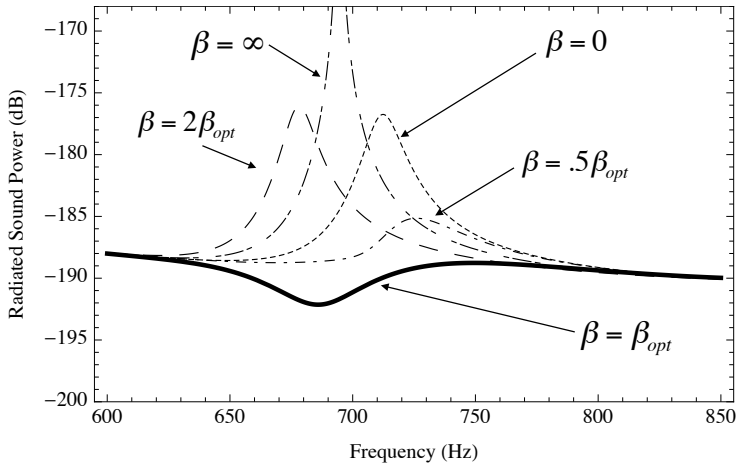

(b) Radiated Sound Power

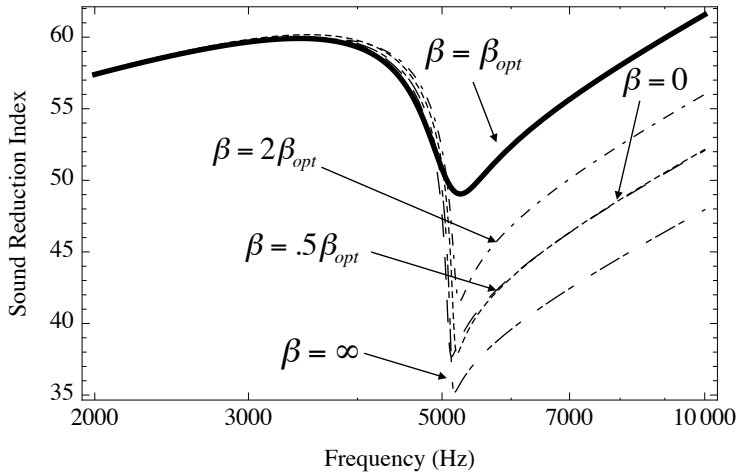

(c) Sound Reduction Index

Figure 4.9: Sound Radiation Index, Radiated Sound Power and Far Field Pressure for a PEM plate as a function of the tuning parameter.

4.5 Conclusions

As shown in section 4.4.2 the proposed smart structure contributes to a considerable improvement of the acoustic isolation properties of a thin plate, with respect to the acoustic performance index considered, i.e. far field sound pressure, radiated sound power at plate level and Sound Reduction Index.
A comparison with a standard viscoelastic damping approach and with another passive piezoelectric structure that introduces frequency independent control, the PEM plate, shows how the PRE plate performs a trade off between the two structures. The PRE plate results more efficient in sound radiation and transmission control than a viscoelastic plate, and it is also important to denote that the piezoelectric layer is thinner than the viscoelastic one, and this can be an advantage in terms of weight optimization for high level applications.
The better behaviour of the PEM plate was to be expected, being the PEM plate a resonant circuit. Despite this fact, the advantages of using a PRE plates are clear when considering the effects of parameters variations and when comparing the complexity of the required circuitry. A detailed study of the dynamic and acoustic behaviour of the proposed smart plate structure shows how the control is frequency independent and not very sensitive of parameter variations. The same analysis performed for the PEM plate shows how sensible a resonant structure is to the tuning parameter variation.
Moreover it is crucial to underline that the PRE plate contains itself a real *embedded* circuit, and that does not need any external power supply and any connection with external circuitry. Other passive smart structures, such as the PEM plate or other RL shunt based controllers, need very complex external circuitry that introduce additional weight and required maintenance. This consideration, along with the distributed nature of the circuit means that, with a particular industrial process, it is possible to build smart panels that only need to be assembled, since the optimal parameters of the circuit are determined at construction level.
The drawback of this structure in terms of realizability consists in finding an industrial process for building the piezoelectric layer, that is much bigger than the commercial components available. This problem can be avoided by using multiple patches immersed in an unique resistive material, or using piezoelectric fibers.

Chapter 5

Experiments

Contents

Object of the Chapter

The objective of this chapter is to validate the modelling and optimization procedure introduced in Chapter 3. To this end an aluminium plate is equipped with a matrix of optimally placed piezoelectric transducers and it is connected to the control circuit, realized by using a real time I/O system. The system is tested in order to verify the control capabilities of the selected circuitry.

5.1 Introduction

This chapter resumes all the experimental activities performed to test the optimization procedure and control systems described in Chapter 3.
The main steps of the experimental part are the following:

1. Identification of the acoustical properties of the selected host structure.
2. Optimization of the piezoelectric patches number and positioning
3. Assembling of the structure
4. Setup of the real time controller
5. Acoustical and vibrational measures

5.2 Experimental set up

5.2.1 Measurement Chain

The measurement chain is composed by:

- *piezoelectric patches* used as colocated sensors/actuators;
- a *piezoelectric patch* used for excitation, bonded on the lower side of the structure;
- Power *voltage and current amplifiers* used for driving the piezoelectric patches;
- a *PC* based *real time* control system with signal acquisition and generation cards.
- a laser *vibrometer* to measure the velocity
- *microphones* to measure acoustic pressure

The details of each instrument are listed in table 5.1. In figure 5.1 there is the standard experimental setup.

Instrument	Manufacturer	Model
Laser Vibrometer	Ometron	VPI 8330
I/O System	OROS	OR763
Piezo Driver	TRek	PZD350
Microphone	Bruel & Kjær	Type 4189
Input card	National Instruments	PCI 6250-E
Output card	National Instruments	PCI 6630
Real Time Control System	-	Linux / RTAI

Table 5.1: References for laboratory equipement.

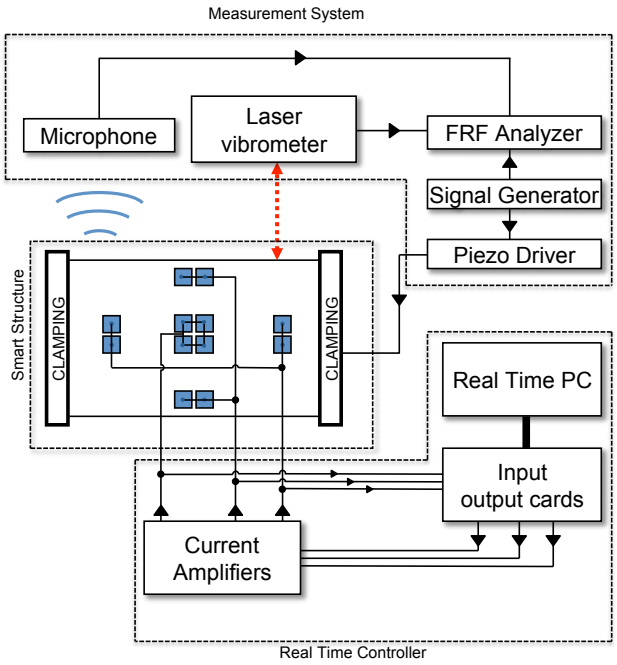

Figure 5.1: Experimental setup

5.2.2 Piezoelectric materials

The used piezoelectric elements are the piezoelectric sheets from Physik Instrumente (PI) Ceramics. They are made of a thickness-polarized thin (thickness hp= 0.20 mm) layer of Lead Zirconate Titanate PIC 151. The corresponding material properties are reported in the Appendix. The upper and lower surfaces of the layer of ceramic material are cover by a thin CuNi film serving as electrode. The electrode mechanical properties (mass and stiffness) are negligible. The thickness and the material properties of the piezoelectric sheets were chosen to obtain relatively high induced-strains with low voltages. The actuators have an accessible lower side electrode on one corner, as shown in figure 5.2.

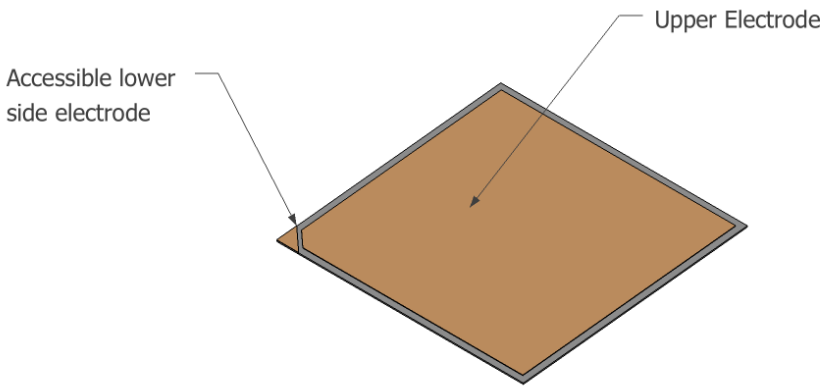

Figure 5.2: Schematic of the pizoelectric patches used for the experiments.

5.2.3 Real Time control system

Since all the control strategies introduced in chapter 3 need high value, or even negative inductors, all the electrical networks will be simulated using an Input/Output Real Time system interfaced with the transducers. The advantage of using this kind of systems are various, and can be resumed in the following points:

- Any circuit can be implemented using graphical editors,
- The parameters of the circuit can be modified in real time,
- Easy switch between one circuit to another,
- Virtual oscioloscopes for monitoring control signals without perturbing the system.

Architecture

To this purpose a Linux based open source system is used, with real time support added by the community project RTAI (*Real Time Application Interface*) and hardware drivers provided by the *COMEDI* project. For creating the real time code a ScicosLab/Scicos environment was used.
A National Instruments PCI6052E card was used for measuring voltages and a National Instruments PCI6633 card was used for generating currents, passing through a voltage controlled current generator.
The shunt network is realised through an active feedback control considering as measurement signal the voltage on each piezoelectric transducer and as

control signal the current flowing through the same piezoelectric transducer, in order to virtually implement the network behaviour. The choice of using voltage as measurement signal and current as control signal is due to the fact that measuring voltage is more accurate, and that driving a PZT patch with current reduces hysteretic phenomena.
An example of the desktop of a PC running RTAI linux is in figure 5.3.

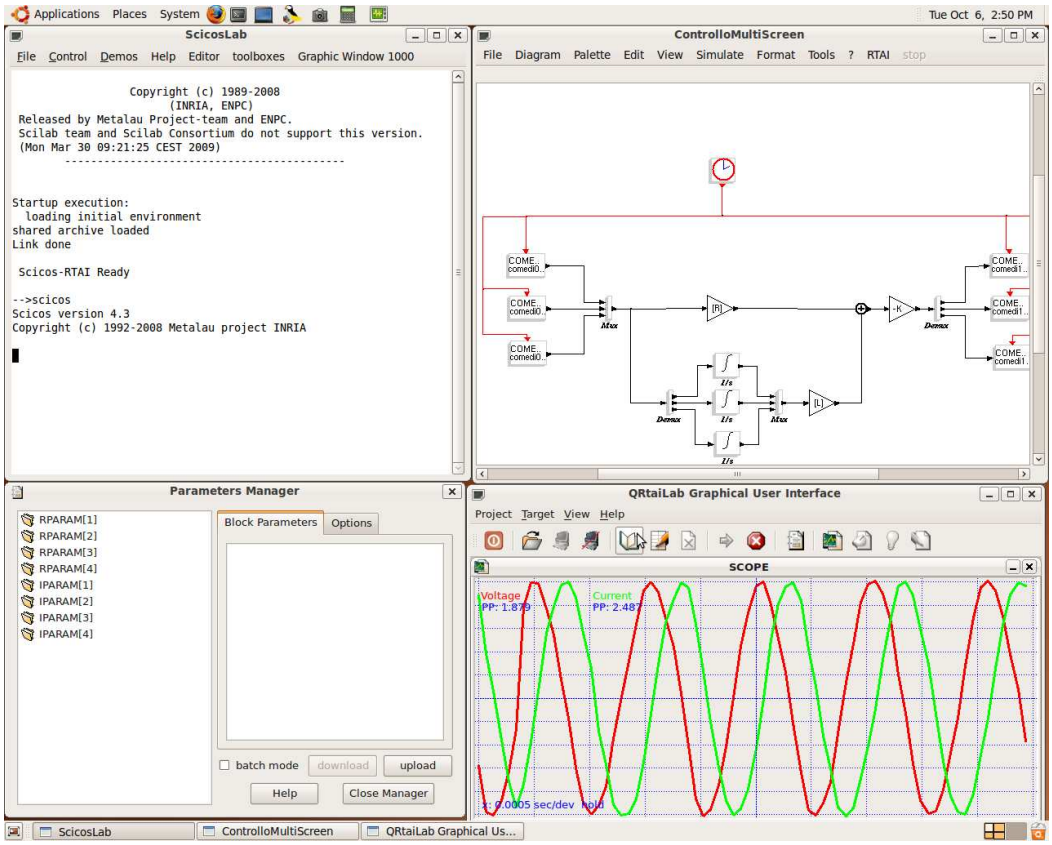

Figure 5.3: PC running RTAI Linux

5.2.4 Electronic circuits

Current generators

The voltage control current generators were realized following the scheme in figure 5.4, using an OPA445 as operational amplifier and precision resistors. The actual realization of the circuit, with three generators on the same card, in figure 5.5.

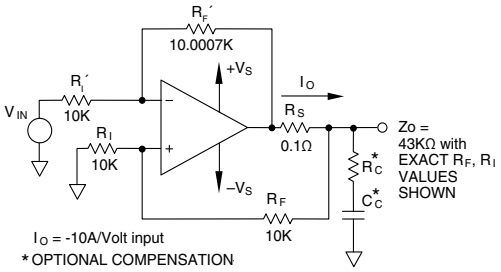

Figure 5.4: Schematic of one current generator

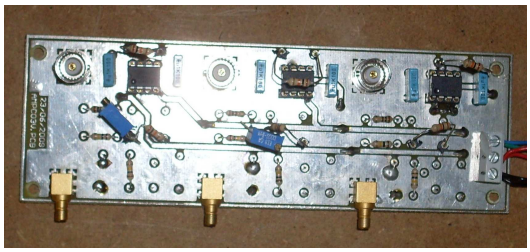

Figure 5.5: Current generators

5.3 Optimization of the smart structure

5.3.1 Acoustic characterization of the host structure

The host structure chosen for the experiments is a rectangular aluminium plate, clamped on short edges and free on the others and fixed on a wooden plate (figure 5.6). The choice of a non classic case study, the Clamped-Clamped-Free-Free plate, permits to highlight the robustness of the proposed smart structure when dealing with non ideal boundary conditions.
As discussed in section 2.2 in order to maximize the sound radiation control performances of the controller with respect to the amount of modes that can be controlled, an accurate analysis of the radiation properties of the plate is performed.

Vibrational and numeric analysis

Since with the Clamped-Clamped-Free-Free (C-C-F-F) boundary conditions it is not possible to analytically derive a solution for the eigenvalue problem, the finite element software (Abaqus^{TM}) was used to calculate the modal shapes. The elements used in the finite elements analysis are C3D20R, 20-node quadratic bricks, with reduced integration.
This result is then compared to the natural frequency measured on the actual structure. This has been done because usually the clamping boundary condition is not perfect, and then to obtain a better optimization the real values of natural frequencies will be used.

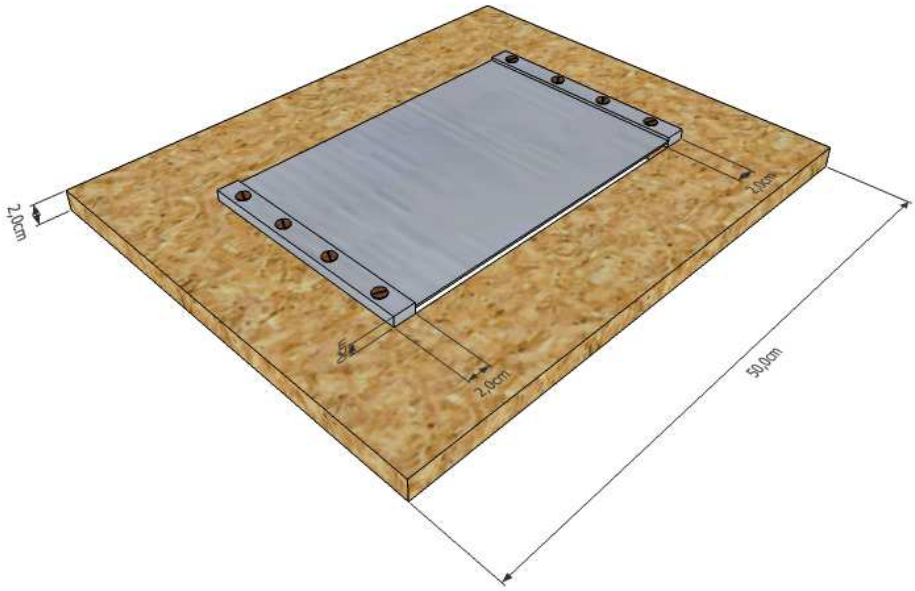

Figure 5.6: Sketch of the host structure

To estimate frequency response function (FRF) of interest, the plate is excited by one piezoelectric actuator with a random band-limited signal so as to excite the first ten modes with a frequency spectrum covering a range from near zero to 1 kHz. A power amplifier to drive the piezoelectric actuator with current is used. It is well known that the piezoelectric material presents a non-linear behaviour when the level of excitation is very high. To check for non-linearity a particular FRF measurement has been repeated a number of times using different levels and types of excitation. Thus, a suited level of excitation has been chosen to avoid non-linearity. A laser vibrometer provides the output. The analysis is performed with a frequency resolution of about 0.625 Hz and 30 averages. The nominal estimate of the FRF magnitude, $\left|\hat{H}(f)\right|$, and phase, $\hat{\alpha}(f)$,for a given point are shown in figure 5.7. Several other measures were made, being the amplitude of the FRF at natural frequencies dependent on the position of the measurement point. The coherence is also displayed to check for random or bias errors.

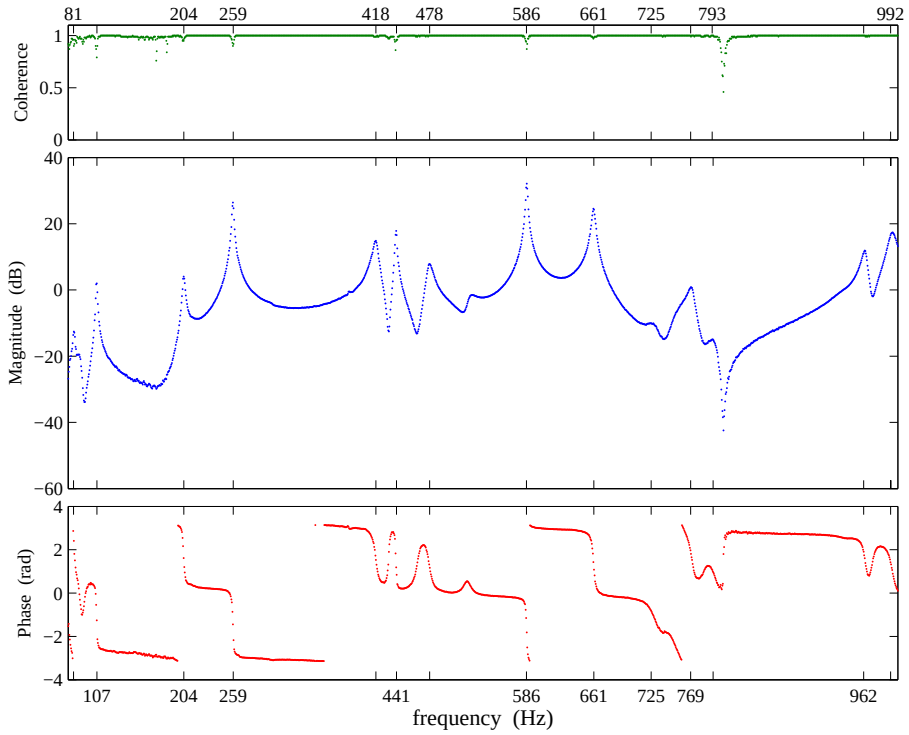

Figure 5.7: FRF of the plate.

The measures are compared with the natural frequencies obtained numerically with ABAQUS. The modal shapes calculated for the plate are plotted in figure 5.8 while the resonance frequencies measured and estimated numerically are listed in table 5.2.

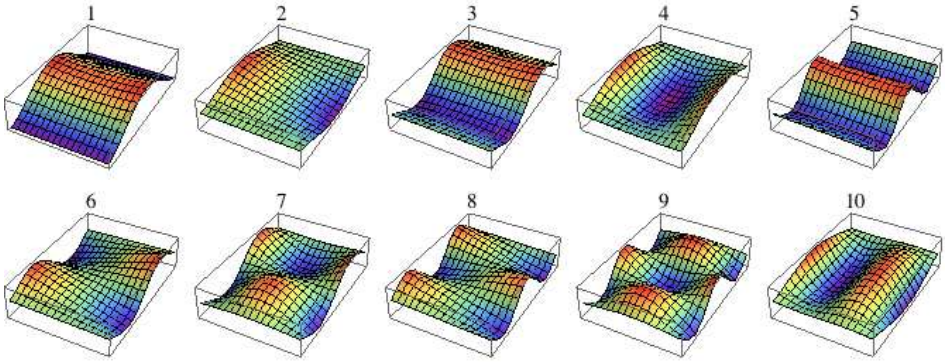

Figure 5.8: Modal shapes calculated with Abaqus

mode	type	measured (Hz)	numerical (Hz)
1	(1,1)	81.25	89.71 (+9.43%)
2	(1,2)	106.9	120.98 (+11.64%)
3	(2,1)	203.8	249.62 (+18.36%)
4	(1,3)	258.8	266.79 (+2.99%)
5	(3,1)	418.1	399.36 (-4.69%)
6	(2,2)	440.6	461.75 (+4.58%)
7	(2,3)	478	491.39 (+2.72%)
8	(3,2)	586.2	543.68 (-7.82%)
9	(3,3)	660.6	583.61 (-13.19%)
10	(1,4)	725	714.94 (-1.41%)

Table 5.2: Resonance frequencies and damping ratios of the plate.

From the analysis of table 5.2 one can see that there is a considerable discrepancy between the estimated and the actual value of the natural frequencies. This difference is due mostly to the nature boundary conditions, which do not perform a good clamping.

Acoustic characterization

Following the procedure described in section 2.2, and as done in section 4.4.2, the structure is decomposed in a matrix of 12×12 elementary elements radiating as pistons. The maximal frequency of interest has been chosen equal to $f_{max} = 1000$, in order to consider the first ten modes. The obtained modal radiation coefficients are listed in table 5.3 and in figure 5.9.

mode	frequency (Hz)	η_i^{norm}
mode (1,1)	81.25	0.638
mode (1,2)	106.9	0.000
mode (2,1)	203.8	0.049
mode (1,3)	258.8	0.520
mode (3,1)	418.1	1.000
mode (2,2)	440.6	0.031
mode (2,3)	478	0.155
mode (3,2)	586.2	0.215
mode (3,3)	660.6	0.398
mode (1,4)	725	0.160

Table 5.3: Resonance frequencies of the plate.

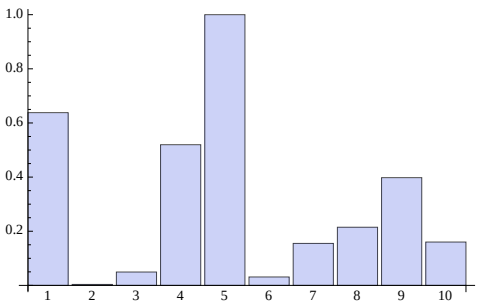

Figure 5.9: Normalized modal radiation coefficents η_i^{norm}

The set ξ_C of modes that have to be controlled are then distinguished with the aid of equation 3.74, and it is:

$$\xi_C = \{4, 5, 9\} \tag{5.1}$$

As expected the most radiating modes are still the odds ones. The first mode has been neglected, being the corresponding natural frequency too low related to the human hearing sensitivity.

5.3.2 Piezolectric patches placement optimization

This section is dedicated to the optimization of the piezoelectric transducer positioning, following the method introduced in section 3.4.
The piezoelectric transducers that will be used for assembling the structure are square shaped, and their dimensions are $2\text{cm} \times 2\text{cm} \times 0.02\text{cm}$. In order to simplify the assembling, the piezoelectric transducers will be positioned only on the upper face of the plate. As stated in section 3.2, this approximation holds because extensional waves can be neglected in this range of frequencies.

Several piezo-elements will be connected in parallel, as done in section 3.4, in order to obtain a coupling matrix as orthogonal as possible and for uncoupling even modes. Since the number of modes to be controlled is equal to three, there will be three groups transducers, each one composed by four piezoelectric patches connected in parallel.
The modal controllabilities $\mathscr{M}_{in}(x_n, y_n)$ in function of the positioning of a single square patch, for target vibrational modes is plotted in figure 5.10.

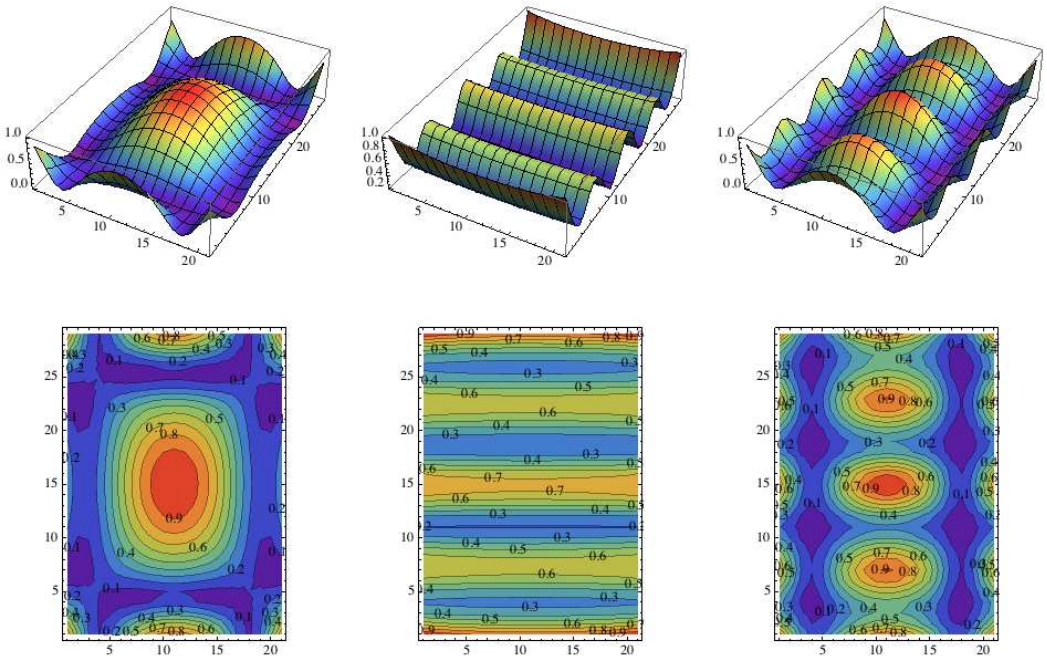

Figure 5.10: Modal controllability for each target mode

The spatial controllability $\mathscr{S}(x_n, y_n)$ and the acoustic controllability $\mathscr{A}_n(x_n, y_n)$ for the plate and for the selected modes are plotted in figures 5.11 and 5.12 respectively. From a comparison between the two plots it is evident how the acoustical controllability permits to find optimal spots for

having an higher authority over the radiated sound power.

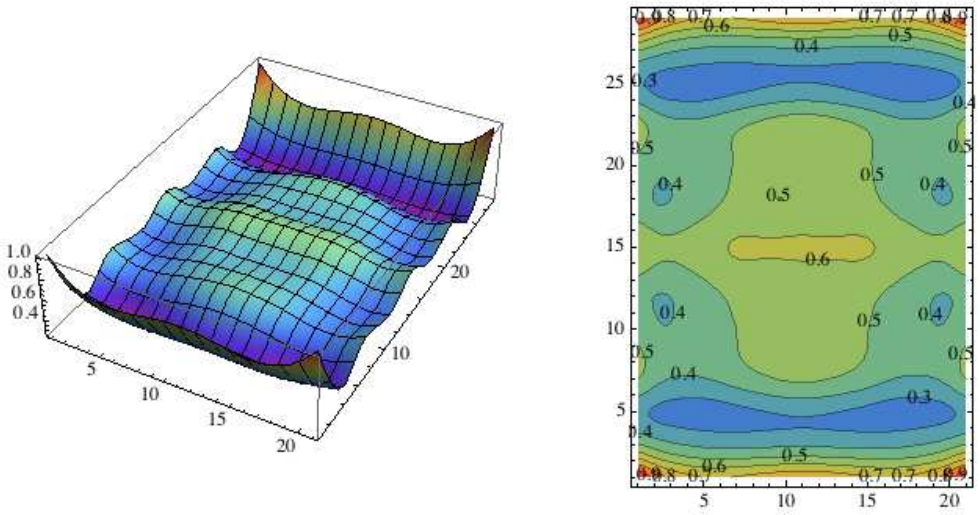

Figure 5.11: Spatial controllability $\mathscr{S}(x_n, y_n)$ in function of the positioning of the actuator

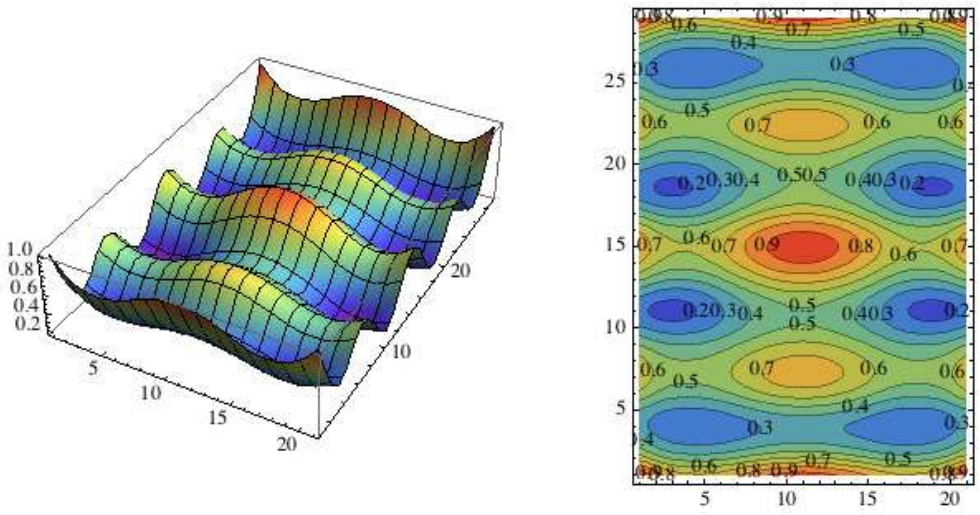

Figure 5.12: $\mathscr{A}_n(x_n, y_n)$ in function of the positioning of the actuator

Analysing figure 5.12 the best spot to assure the acoustic controllability seems to be near the clampings. This is true when considering perfect boundary conditions. Since in our case study, and as highlighted in the previous section, the clampings are not perfect, that zone should be avoided. This because the optimal positioning area is very small, and since the acoustic controllability decreases roughly, this positioning will probably correspond to a small coupling coefficient.
Hence, the research for the optimal values is limited on the set of points R^*,

where

$$R^* = \left\{ (x, y \in S) \,/\, \left(0 \leq x \leq \left(\frac{a - L_{px}}{2}\right)\right) \left(0.2 \leq y \leq \left(\frac{b - L_{py}}{2}\right)\right) \right\}. \tag{5.2}$$

The acoustical controllability for the portion R^* of the plate is plotted in figure 5.13.

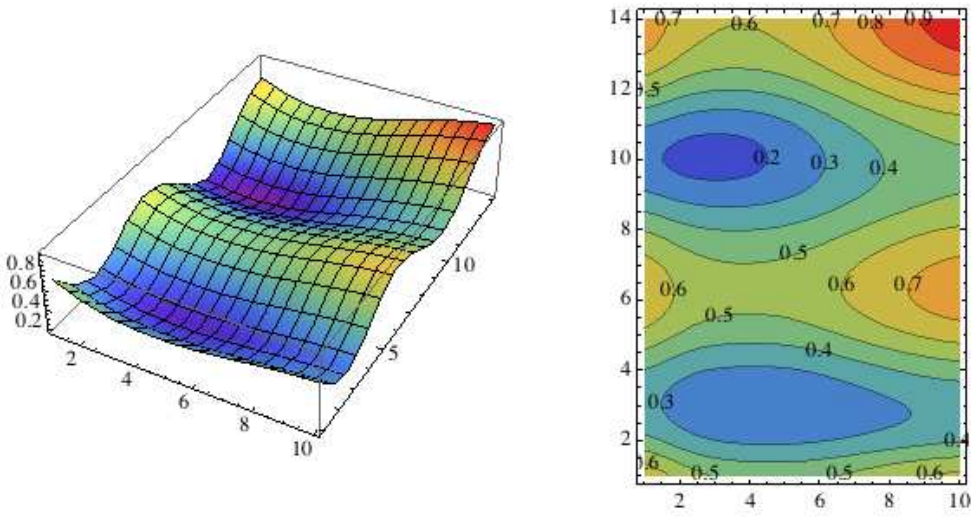

Figure 5.13: Acoustic controllability limited to the set of points R^*

The constrained optimization procedure for obtaining the best positioning for the transducers is then the following

$$\max_{(x_n, y_n) \in R^*} \mathscr{A}_n(x_n, y_n)$$
$$\text{subjected to } \mathscr{M}_{inr}(x_n, y_n) \geqslant .8, \text{ for at least one } i \in \chi_C$$
$$,$$

in order to grant at the same time the highest acoustical controllability assuring the modal controllability for the target modes. The optimal points are then resumed in table 5.4

(x_n, y_n)	$\mathscr{A}_n$	$\mathscr{M}_{4n}$	$\mathscr{M}_{5n}$	$\mathscr{M}_{9n}$
$(0.085, 0.130)$	0.95	0.98	0.75	0.97
$(0.010, 0.130)$	0.78	0.26	0.80	0.76
$(0.085, 0.600)$	0.75	0.39	0.64	0.89

Table 5.4: Optimal locations for the piezoelectric patches

5.4 Modal parameters identification

In order to accurately describe a physical system through a reduced order modal model, as the one introduced in section 3.2.5 , a set of parameters is needed. Since the structure has 3 groups of piezoelectric patches and is described by 10 modal coordinates these parameters are:

- 10 short-circuited adimensional circular frequencies Ω_i
- 30 dimensionless modal couplings γ_{ir}
- 3 electric capacitances C_r

Mechanical resonance frequencies are measured analysing the frequency response of the system through standard techniques used for linear structures. The most complex part of the identification procedure is related to the identification of electromechanical coupling γ_{ir} and electric capacitances C_r.

About the electric capacitance of a piezoelectric patch

The classical definition of the electrical capacitance C of a pair of plane conductors separated by a dielectric material is

$$C = \frac{\varepsilon S}{h} \tag{5.3}$$

where S is the surface of the conductors, ε the dielectric constant and h the distance between the conductors.
The capacitance measures the amount of total energy stored per unit voltage. In a piezoelectric transducer this energy has mechanical and electrical contributions. The amount of total energy stored in electrical form depends on the mechanical constraints applied to the piezoelectric element.
This has as a consequence that piezoelectric patch a without mechanical constraints, i.e. free to move, has a different capacitance than a blocked patch. This different behaviour is modelled using the electric permittivity at constant stress ε^T and at constant deformation ε^S. This distinction implies the definition of two different capacitances for a piezoelectric patch, the blocked capacitance C_r^S and free capacitance C_r^T, defined as follows:

$$C_r^S = \frac{\varepsilon_{33}^S S}{h}, \qquad C_r^T = \frac{\varepsilon_{33}^T S}{h}. \tag{5.4}$$

For common piezoelectric materials (e.g. PZT-5H) the percentile difference between C^T and C^S is as high as 40%. The capacitance of a piezoelectric element bonded on, or embedded in a structure is different from both these values and depends on the relative stiffness of the host structure and the

piezoelectric material. The capacitance that appears in a modal model is the capacitance measured when the modal coefficients are blocked, the *blocked modal capacitance* C_r^Y. Unfortunately this capacitance cannot be directly measured, for instance with a multimeter or an impedance analyzer. The capacitance that is obtained connecting one of this instruments to a piezoelectric patch leaving the structure free to deform is the *free modal capacitance* C_r^T

Overview of the selected identification methods

In the literature several techniques for estimating modal parameters of a smart structure, are proposed and tested. Among these, three methods have been selected for solving the identification problem.

The first method is the *Open/Shorted circuit* (OS) method,introduced in [Hagood 1991]. It is based on the comparison of the natural frequencies of the structure with open or short circuited patches. This method has the advantage of being very simple, both in simulations and experimental situations.

The second proposed method is the *Resonant Shunting* (RS) method, introduced in [Porfiri 2007]. It is based on the properties of dynamic properties of systems with two degrees of freedom, and uses a resonant RL circuit shunted on the piezoelectric patch in order to have a resonant system. This method permits to measure the coupling coefficient and blocked modal capacitance with small uncertainties, but needs a tunable external circuit, usually difficult to realize. It is difficult to use this method in simulations.

The third method uses a multi-degree of freedom curve fit it order to derive the piezoelectric parameters from the experimental impedance of the transducer, and it is described in [Carabelli 2000].

OS method With this method the coupling coefficients γ_{ir} are identified using the non-dimensional circular frequencies Ω_i of the structure with every transducer short-circuited, and the non-dimensional circular resonance frequency $\Omega_i^{(r)} = \omega_i^{(r)}/\omega_i$ of the structure with every transducer short-circuited except the $r-th$ one left open-circuited.
If the modes are reasonably spaced in frequency the influence of the $j-th$ mode on the mode $i-th$ can be neglected for $j \neq i$. Then the value of open-frequencies can be derived from equations (4.31) with $I_r = 0$:

$$\Omega_i^{(r)} = \Omega_i \sqrt{1+\gamma_{ir}^2}, \tag{5.5}$$

and then

$$\gamma_{ir} = \Omega_i \sqrt{1+\gamma_{ir}^2}, \tag{5.6}$$

If the circular frequencies are measured with an uncertainty σ_ω, the uncertainty of the coupling estimate is [Porfiri 2007]

$$\frac{\sigma(|\gamma_{ir}|)}{|\gamma_{ir}|} \simeq \frac{\sqrt{2}}{\gamma_{ir}^2}\frac{\sigma_\omega}{\omega_i} \tag{5.7}$$

where the approximation holds because the value of γ_{ir} is usually small, (typically $0.01 \leqslant \gamma_{ir} \leqslant 0.3$. Thus, the estimate of γ with the OS method is very sensitive to errors in the measure of the resonance frequencies

The values of the blocked modal capacitances is derived from the value of free modal capacitance, measured with a multimeter, and are calculated from the static form of system (4.31) assuming that the modal forces are zero. The value of the blocked modal capacitances is then

$$C_r^Y = \frac{C_r^F}{1 + \sum_{j=1}^n \gamma_{ir}^2} \tag{5.8}$$

It is important to underline that this indirect estimation is more accurate if the number of considered modes, and then of coupling coefficients in the series, is sufficiently high.

RS method This method is developed using the concept of fixed points, the same concept used in section 3.3.2 for the optimization of the forced response of an RL circuit. When condition (3.46) is satisfied, it is easy to calculate the absolute value of the coupling coefficient and the Capacitance

$$|\gamma_{ir}| = \sqrt{2}\frac{\Omega_T - \Omega_T}{\Omega_i} = \sqrt{2}\frac{\omega_T - \omega_S}{\omega_i} \tag{5.9}$$

$$C_r^{Y_i} = \frac{1}{\omega_i^2 L} \tag{5.10}$$

If the circular frequencies are measured with an uncertainty σ_ω, the uncertainty of the coupling estimate is [Porfiri 2007]

$$\frac{\sigma(|\gamma_{ir}|)}{|\gamma_{ir}|} \simeq \frac{2}{|\gamma_{ir}|}\frac{\sigma_\omega}{\omega} \tag{5.11}$$

where the approximation holds because the value of γ_{ir} is usually small.

Impedences curve fit method Piezoelectric parameters of the transducers can be derived by performing multi-degree of freedom curve fits, as described in [Carabelli 2000]. The generic impedance of a piezoelectric transducer is defined by the ratio between the voltage V_r of the transducer and the current I_r injected into the transducer in this way:

$$Z_r(\omega) = \frac{1}{j\omega}\left(C_r + \frac{1}{j\omega R_N} + \sum_{i=1}^{N}\frac{g_{ir}^2}{\omega_i^2 - \omega^2 + 2j\zeta_i\omega_i\omega}\right)^{-1} \tag{5.12}$$

where R_N is the Norton equivalent resistance of the current generator, g_{ir} is the dimensional coupling coefficient, C_r the capacitance and ζ_i the mechanical modal damping. This non-linear curve-fitting problem is solved in least-squares sense defining the cost function

$$E = \sum_{l=1}^{N} w_l(\Omega_l) \left| \left(\hat{Z}_h(\Omega_l) - Z_h(\Omega_l) \right)^2 \right| \tag{5.13}$$

in which $w_l(\Omega_l)$ is a weighting factor, and N is the number of the data points. The curve fit process has to determine the values of the unknown piezoelectric modal parameters such that the error E is minimised. During the estimation process, uncertainty information is taken into account. The coherence function, $\hat{\gamma}^2_{xy}(\Omega_l)$, is chosen as weighting function w_l. The normalised piezoelectric coupling coefficients are computed by the following relationship

$$\gamma_{jh} = \frac{g_{jh}}{\omega_j \sqrt{\rho_{pl} C_h}} \tag{5.14}$$

Comparison Each strategy has its advantages and its drawbacks. The O/S method is the simplest, but suffers from the incertitudes in measuring the natural frequencies, and gives only an indirect calculus for the capacity. The RS method is accurate, but requires several measures and complex tunings. For the experimental setup used in our experimentationn, since there are current generators, the most convenient is the curve fit method.

5.4.1 Numerical simulations

In order to verify the correct positioning of the piezoelectric patches a numerical analysis has been performed, again using Abaqus. For the sake of simplicity, the numerical coupling coefficients matrix and the capacitances have been calculated using the Open/Short circuit technique. An example of a vibration mode calculated with abaqus is in figure 5.14 The obtained couping matrix is

$$\tilde{\mathbf{\Gamma}}_{\text{FEM}} = \begin{bmatrix} -0.055 & -0.040 & 0.012 \\ -0.055 & 0.036 & -0.057 \\ 0.079 & -0.038 & 0.044 \end{bmatrix}. \tag{5.15}$$

C_1	C_2	C_3
122	121	122

Table 5.5: Capacitances of the piezoelectric transducers (nF), calculated with Abaqus.

Remark 12. *It is important to undeline that this numerical simulation does not take account of the effect of the epoxy resin.*

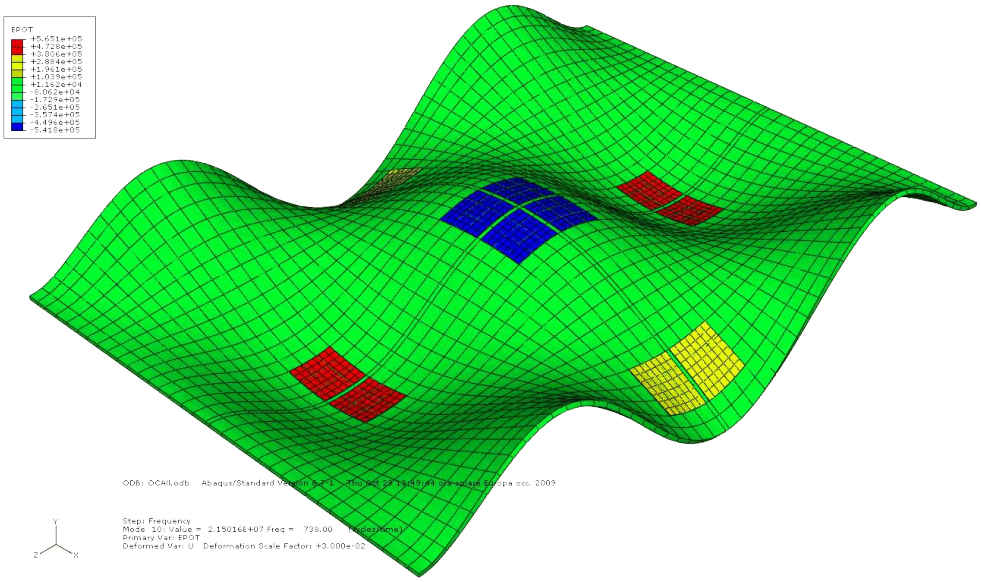

Figure 5.14: Mode (3,3) with piezoelectric actuators, calculated with Abaqus.

5.4.2 Assembly of the smart structure

The structure has been assembled following the optimization procedure described in the previous section. The piezoelectric patches have been bonded on the surface of the plate using a two-component structural epoxy resin at ambient temperature.
The resulting smart structure is in figure 5.15.

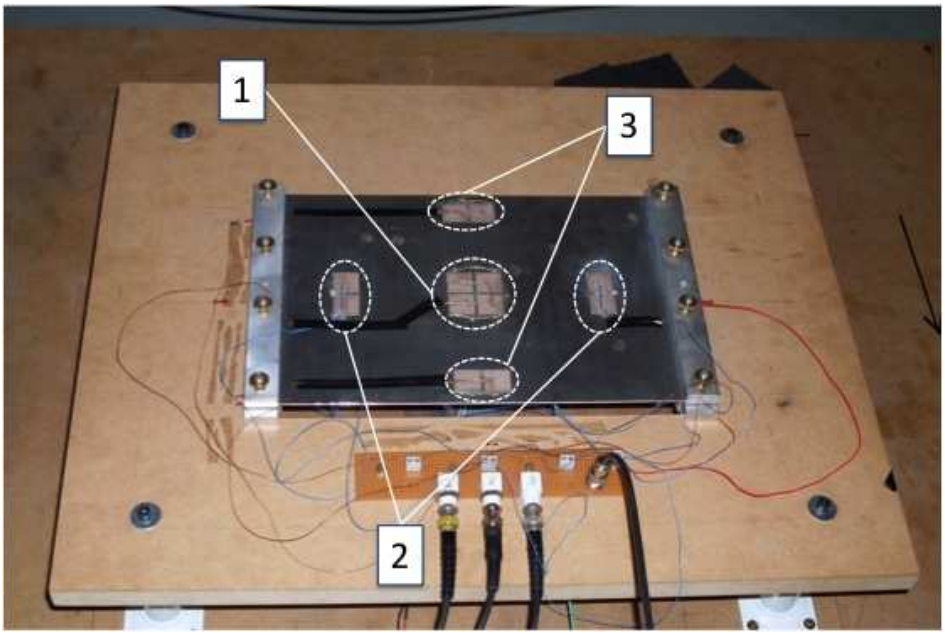

Figure 5.15: Assembled smart structure

5.4.3 System Identification Measures

In this section the identification of the electromechanical parameters is performed.

5.4.3.1 Coupling coefficients and capacitances

The method that has been chosen for measuring the piezoelectric parameters is the impedances curve fit methos. This method has the advantage of being very easy to apply, and of providing accurate results. Since the modes to be controlled is limited, only the coupling coefficients relative to those modes will be measured.
For measuring the impedance of the piezoelectric transducer a random excitation current is applied over a frequency range near zero to 1 kHz and the resulting voltage response is measured on the same piezoelectric transducer. This type of test requires a current source which is voltage driven.

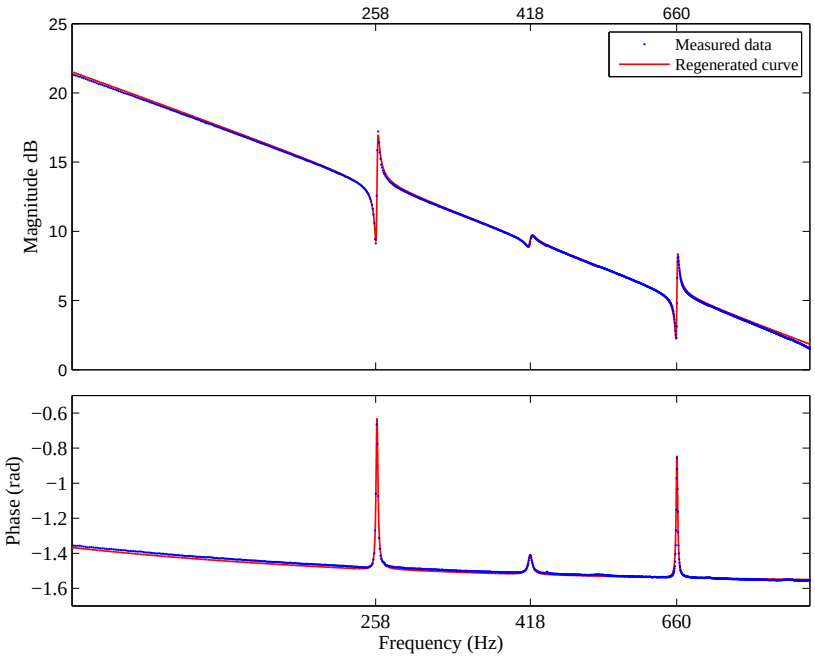

Figure 5.16: Comparison of measured electric impedance of the first piezoelectric transducer and curve fit.

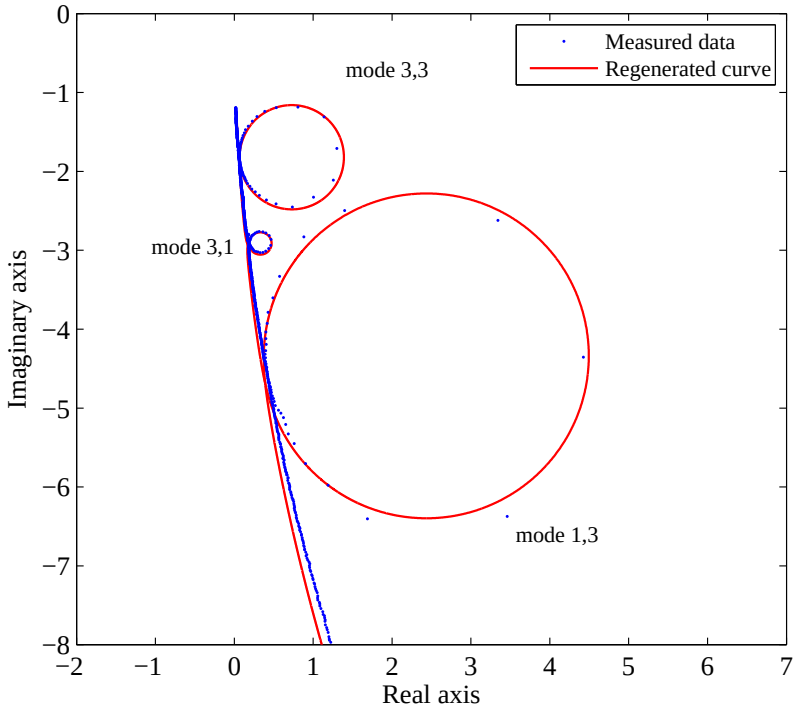

Figure 5.17: Comparison of the nyquist plot of the measured electric impedance of the first piezoelectric transducer and curve fit.

In figures 5.16 and 5.17, it is shown the comparison between the measured piezoelectric impedances and the regenerated curves obtained by the extracted piezoelectric parameters. The obtained normalized electromechanical matrix is then

$$\tilde{\mathbf{\Gamma}} = \begin{bmatrix} -0.077(-12\%) & -0.024(-16\%) & 0.010(-14\%) \\ -0.036(-12\%) & 0.031(-16\%) & -0.033(-14\%) \\ 0.059(-12\%) & -0.054(-17\%) & 0.030(-13\%) \end{bmatrix}. \tag{5.16}$$

while the capacitances are summarized in table 5.6 . As shown by the per-

C_1	C_2	C_3
$121(-1\%)$	$120(-1\%)$	$122(\pm 0\%)$

Table 5.6: Capacitances of the piezoelectric transducers (nF).

centage values in equation (5.16) and table 5.6 , these results differ with those obtained from the FE simulation, mostly because of the geometrical imperfections of the plate and of the clampings. These imperfections reflect on modal shapes influencing the value of the coupling, especially for low frequency modes. This occurs because the optimization of transducers position was performed starting from the calculated modal shapes, rather than the ones of the real structure, but also for the presence of the epoxy resin, which was not considered in the numerical simulations.

5.5 Results

In this sections the results of simulations and measures are presented. First of all the three selected control strategies are tested on the electromechanical model of the structure with the identified parameters. This is done in order to verify the correct behaviour of the controllers, and to give a reference of how well the real time system works. Then the measures are presented. The measures have been realized following procedures present in the literature [Chen 2009, Ducarne 2009, Giorgio 2009, Maurini 2007, Porfiri 2007, Thomas 2009].

5.5.1 Simulations

Using the parameters calculated in section 5.4.3, the smart structure is simulated, using a Simulink/Matlab code, as done in section 4.4.2. This simulation uses the actual value of the coupling coefficients, and then permits to have a good estimation of the control capabilities of the proposed passive circuits.

The first simulation regards the FRF of the velocity at a point of the plate, figure 5.18. The plot shows how the control system damps the selected modes. A mean attenuation of $20dB$ for each target mode is obtained, and the RL network performs better than the simple RL shunt.

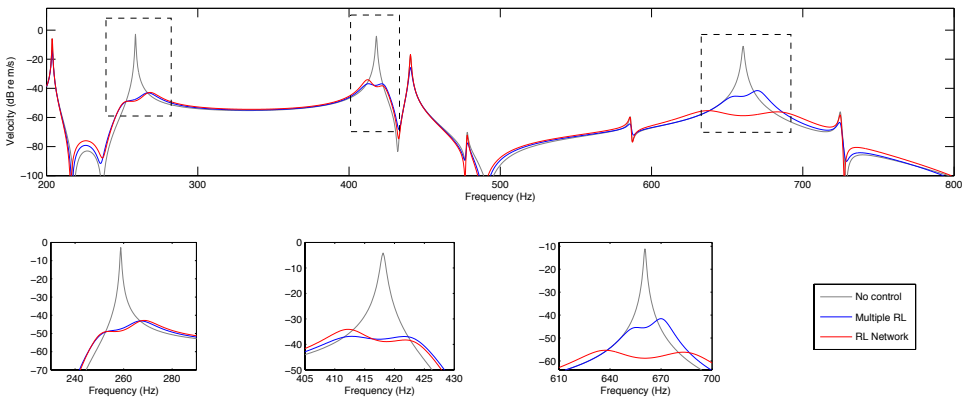

Figure 5.18: Simulated FRF Response of the plate velocity with different types of control

The far field sound pressure and the radiated sound power are plotted in figure 5.19 and 5.20 respectively, showing the effective authority of the controller over the radiated sound power and pressure.

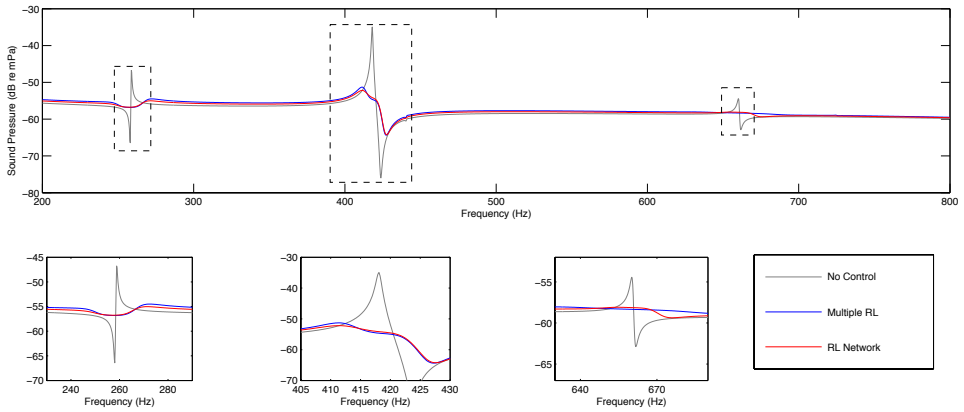

Figure 5.19: Simulated FRF of the sound pressure with different types of control

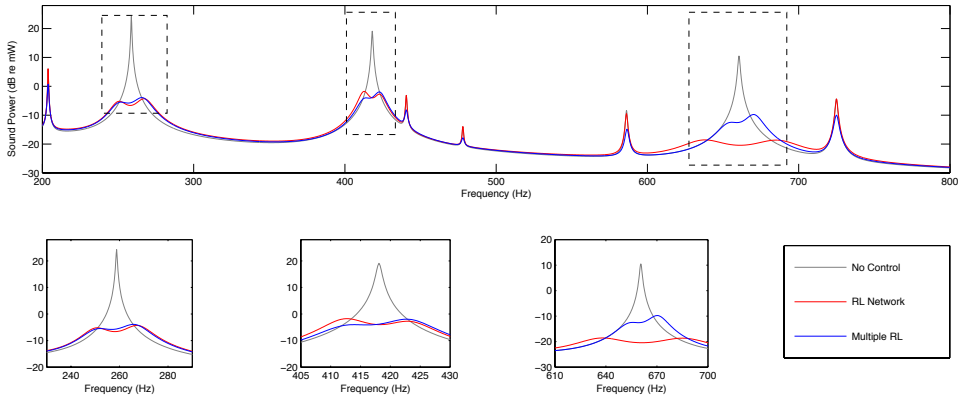

Figure 5.20: Simulated FRF of the radiated sound power with different types of control

These simulations are in agreement with those of section 5.5.1. The effect of this controller are more evident on the 9-th mode because it is well coupled with all the piezoelectric patches. An accurate description of the results will follow in the next section.

5.5.2 Setup of the Real Time controller

The use of a real time controller for the implementation of passive circuits for vibration control is already present in the literature, the most recent works are [Giorgio 2009, Ducarne 2009]. This authors used the package *xPC Terget* from Matlab/Simulink for running the real time code.
In this work the software used is based on a comunity project, RTAI, and all open source.

The functionement is almost the same as Simulink. The circuit is composed by logic boxes interconnected to each other and to the I/O port. An exemple window of of the program Scicos, the open source equivalent of Simulink, is in figure 5.21.

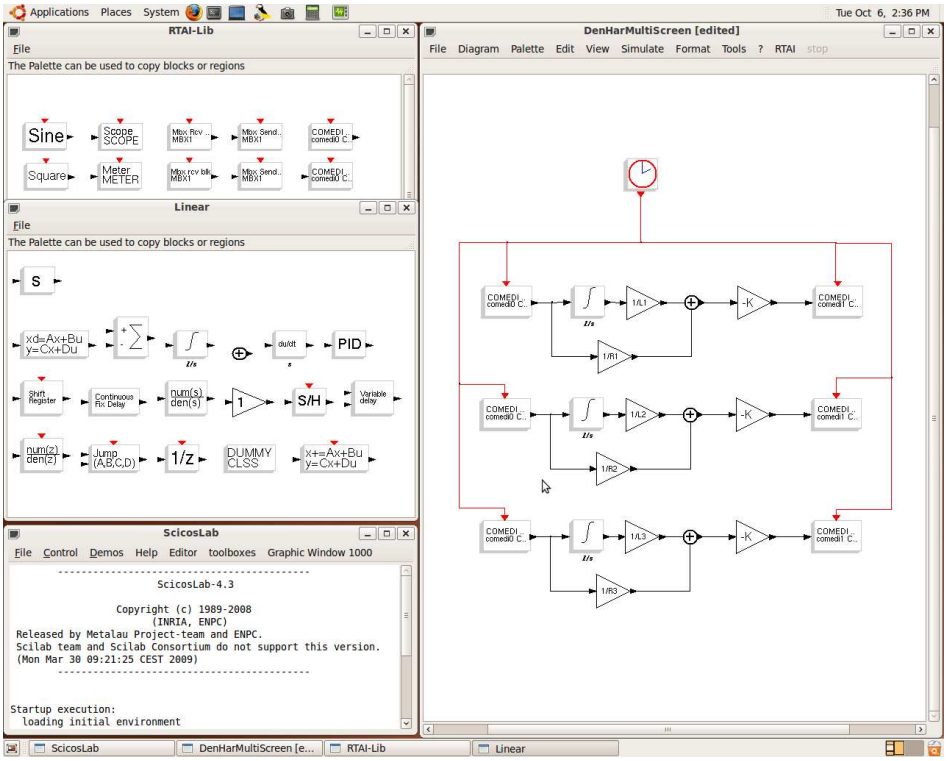

Figure 5.21: Scicos example window.

The drivers for the acquisition and generator cards are granted by another internet community project, COMEDI. The database of card supported by COMEDI is larger than the one supported by *xPC Target*, and that is one of the reasons why we choosed the open source platform for developing the controllers.

The Sciocos diagram used for the multimode real time controller is in figure 5.23, while the one used for the RL circuit is in figure 5.22.

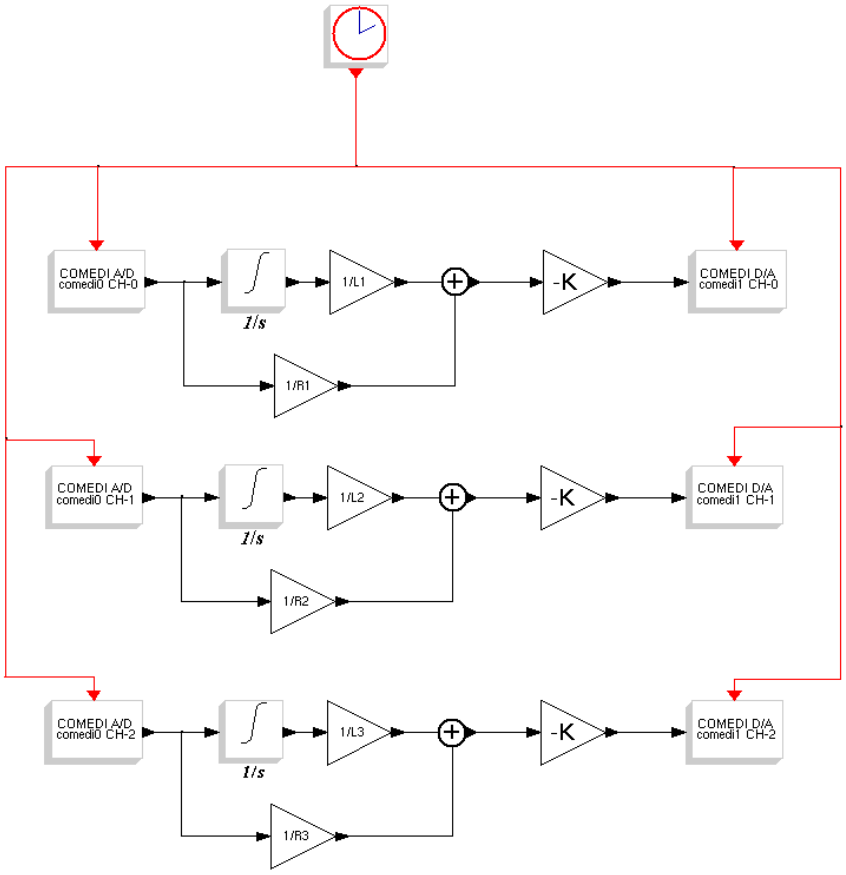

Figure 5.22: Scicos diagram for the real time program of the multiple RL circuit.

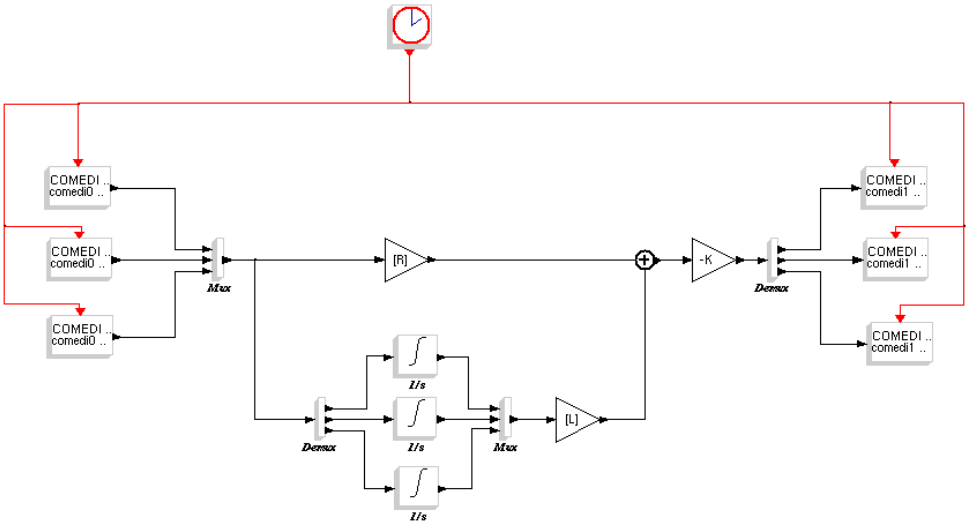

Figure 5.23: Scicos diagram for the real time program of the RL network circuit.

5.5.3 Measures

Vibrational analysis

To check the validity of control, an FFT analysis is performed to calculate a FRF of the beam. To this end an OROS I/O measurement system was used. The disturbance actuator is one piezoelectric transducer placed in the lower side of the plate, driven by a random multi-sine waveform with a frequency range from 50 Hz to 800 Hz and an amplitude of the single sine-wave equal to 2V. A power voltage amplifier TREk was used to correctly drive the transducer. A laser vibrometer and a microphone are used to measure the velocity and pressure, and, therefore, to calculate the FRF. The acquisition time is 1.6 s, and this implies a frequency resolution $df = 0.625Hz$. The other three groups of piezoelectric transducers are used to control plate vibrations.

The measures in figure 5.24 were obtained using a PZT patch as disturbance and measuring the velocity with the vibrometer and shows how the proposed control reduces the amplitude of modes of interest more efficiently than a single RL shunt. The multimodal control has different performances for each mode because of the different coupling coefficients of the transducers.

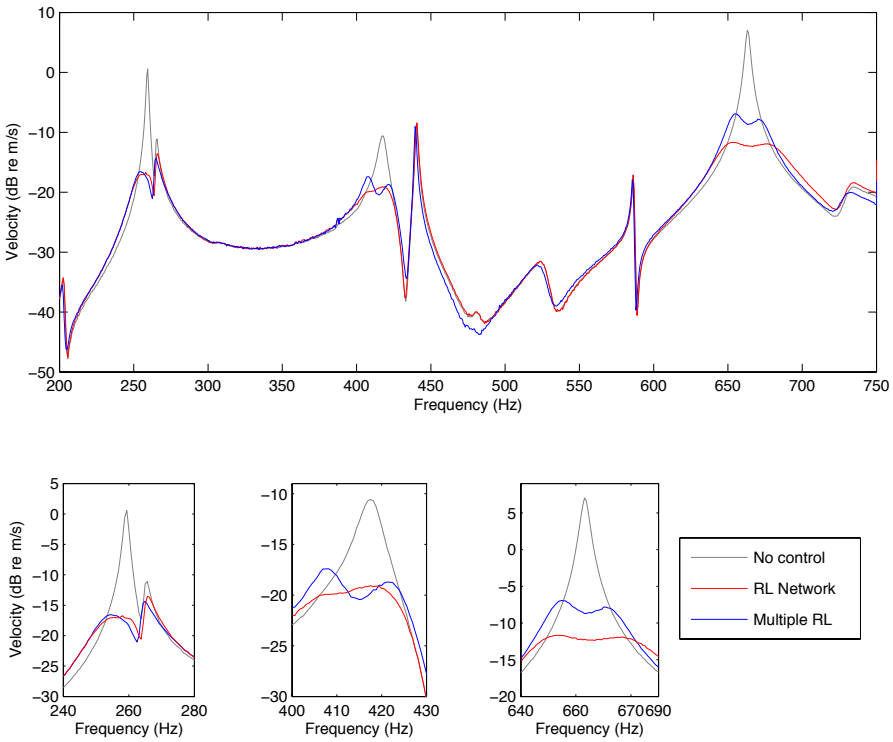

Figure 5.24: FRF Response of the plate velocity with different types of control

This because each piezoelectric patch contributes to the damping of a certain mode proportionally to its coupling with it. Being the 9^{th} mode,

the (3,3), well coupled with all three transducers, this results in an higher damping. The 4^{th} mode, the (3,1), is well coupled only with one transducer and then the damping is the same of that of the RL shunt. The 5^{th} mode, the (1,3), is well coupled with two transducers, and then the damping introduced by the RL network is higher than for the RL Shunt.

Remark 13. *It is important to remark that, for the RL shunts, the patches have been selected for having a good coupling with that mode. This means that a wrong selection of the patch, or a failure, results in a complete loss of control authority of the controller on that mode. This does not occur when using a RL network, which uses all the transducers for controlling each mode.*

The damping listed in table 5.7 show how the RL network introduces a mean 20dB damping on each mode.

Mode	No Control	Multiple *RL*	*RL* Network
4	0.57	−16.72 (−17.29)	−16.72 (−17.29)
5	−10.57	−17.4 (−6.83)	−19.19 (−8.62)
9	7.03	−9.92 (−16.95)	−11.9 (−19.82)

Table 5.7: Amplitude of the modal velocities and the damping introduced by the controllers on each mode.

Acoustic analysis

The measures plotted in figure 5.25 is obtained using a PZT patch as disturbance and measuring the pressure following the ISO 3745 [ISO 3745 1977] standard. The results show a considerable reduction in terms of far field sound pressure with the proposed controller, in agreement of the results obtained in figure 5.24.
Several considerations can be done from the analysis of the figure 5.25. First of all, although the measure being quite disturbed, due to the not perfect acoustic insolation of the testing room, the uncontrolled curve shows that the more radiating modes are effectively the ones selected with the previous acoustical analysis. Then the efficacity of the controller in controlling the structure at thaose frequencies is confirmed.
Finally it is important to denote as the Real Time control system implemented using RTAI is performant, allowing us to simulate a multi I/O complex circuit like the RL network without any problems.

The values of the amplitude of the pressure field, expressed in dB, calculated for each target mode, are listed in table 5.8

The last measure, plotted in figure 5.26, shows the far field sound pressure radiated by each mode without and with control for each of the three controlled modes. The measure is obtained exciting each mode with a pure

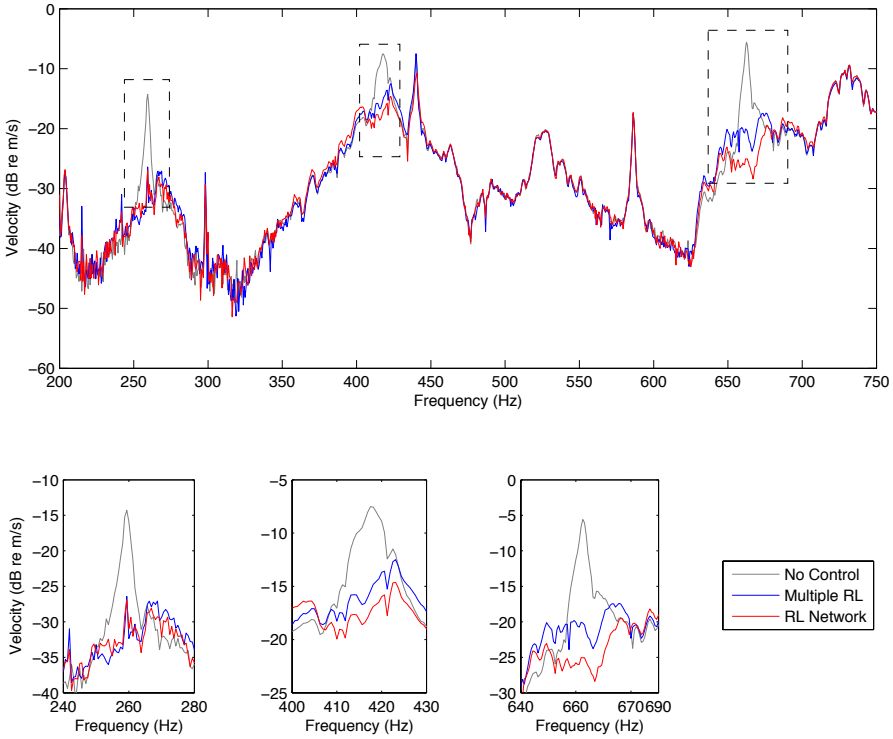

Figure 5.25: FRF Response of far field sound pressure with different types of control

tone sent to a piezoelectric patch with a power voltage amplifier, and measured using a microphone. From this measure one can appreciate again the effectiveness of the RL network controller over the three target modes.

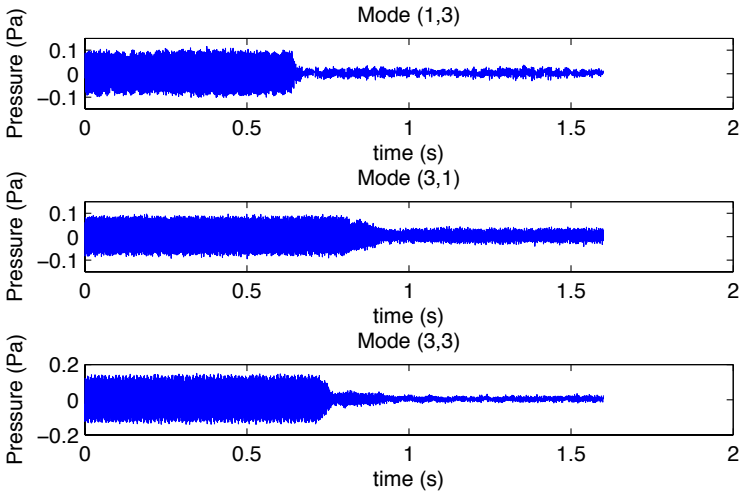

Figure 5.26: Sound pressure of each mode at its natural frequency, with and without control.

Mode	No Control	Multiple RL	RL Network
4	-14.28	-26.9 (-12.62)	-26.9 (-12.62)
5	-7.51	-14.82 (-7.03)	-16.87 (-9.35)
9	-5.58	-20.05 (-14.47)	-25.07 (-19.49)

Table 5.8: Amplitude of the sound pressure calculated at the natural frequecies and damping introduced by the controllers.

Comments

This section presents the experimental activity carried on during the thesis, and had as main objective the validation of the theoretical results presented in Chapter 3. A smart plate as been then designed, optimized and assembled following the guidelines of Chapter 3 and the control system has been realized using a Real Time I/O controller. The measures show how in a real case study the proposed design and optimization procedure gives excellent results on the control of radiated sound power.

Chapter 6

Conclusions

6.1 Summary

The objective of this work was the modelling and optimization of passive and semi-passive piezoelectric smart structures, with the aim of reducing the radiated and transmitted sound power. This thematic has been analysed in details, starting from a study of the radiation properties of thin plane structure, in order to deduce useful elements for finding new criteria of optimization. These results are then applied to the modelling of smart structure, with localized and distributed piezoelectric patches positioning. Several control circuits have been analysed and developed, as the case of the Piezoelectric Electrode Plate. A summary of the main results and the specific original contributions is presented below.

Radiation and transmission properties of thin plates

The study of radiation and transmission properties of thin plates was the object of Chapter 2. The analysis of the radiated sound was performed with the aim, on one hand, of finding a simpler way to solve the radiation problem, and on the other hand of finding a method for determining the most radiating modes of the structure. To this end classical methods have been efficiently placed side by side with novel techniques, with the introduction of the radiation filters. This had as a main result the introduction of a numerical method which permits to calculate the modal radiation efficiency for each vibrational mode of the structure. This has as a main advantage the possibility of effectively optimize the control strategy for acting only on most radiating modes, but also gives a simple method for calculating the radiated sound power.
The phenomenon of the transmission of plane waves and diffused sound fields has been discussed too. The problem has been examined in order to find the structural modifications to be introduced by the controller to improve sound isolation.

Localized piezoelectric smart structures

The problem of the modelling and optimization of localized piezoelectric smart structures has been investigated in chapter 3. The modal model of

the smart structure has been obtained using a variational principle. The core of the optimization process stands in the applications of the results obtained from the analysis of the radiation properties of the structure. This allow us to concentrate the control effort only on modes that, in terms of radiation efficiency and then, are the most important, using a small number of transducers and a simpler circuit, for efficiently controlling the radiated sound power over a large band. The optimization of the number of transducers to be used, that is equal to the number of modes to be controlled, has been obtained exploiting the results presented in chapter 2 about modal radiation efficiency and sensitivity of the human hearing. Then an original procedure for the optimization of the placement of the piezoelectric patches is presented, along with the introduction of a novel cost function, the acoustic controllability.

This cost function considers the authority of the control system over the overall acoustic radiation, giving the best positioning for effectively control the most radiating modes.
Then several multi-modal passive and semi-passive circuits have been analysed and optimized for the control of radiated sound power, with the aim of finding the best circuit suitable for acoustic applications. The best choice reveals to be a multi-modal RL network, both for the performances that for the robustness of the controller. The entire modelling and optimization procedure is then applied to the classical case study of a simply supported plate, with excellent results.

Distributed piezoelectric smart structures

The thematic of the reduction of radiated and transmitted sound power by means of distributed piezoelectric smart structures is the object of chapter 4. The main objective was to find a way to design a distributed piezoelectric structure, overcoming to the difficulties related to the complexity of the circuitry and the density of the transducers, especially at high frequencies. To this end an original smart structure, the Piezoelectric Resistive Electrode (PRE) plate is presented. This structure consists of an aluminium plate entirely covered by two piezoelectric layers with a controlled resistivity electrode bonded on each free piezoelectric surface. This homogeneous system is optimized for all frequencies and performs a good trade off between good performances and easy implementation. The modelling, design and optimization of this structure is described in detail, and its acoustic behaviour is compared with that of different multi-modal distributed passive controllers. The results show how the robustness and the performances of the proposed structure are good for sound radiation and transmission control.

Experiments

Section 5 presents the experimental activity carried on during the thesis, and had as main objective the validation of the theoretical results presented in Chapter 3. A smart plate as been then designed, optimized and assembled following the guidelines of Chapter 3 and the control system has been realized using a Real Time I/O controller. The measures show how in a real case study the proposed design and optimization procedure gives excellent results on the control of radiated sound power. The application of the procedure to a non classic case study, the Clamped-Clamped-Free-Free plate permits to highlight the robustness of the proposed controller when dealing with non ideal boundary conditions.

6.2 Original contributions

The main original contributions of this thesis to the existing literature are listed below.

- Complete critical analysis of the radiation properties of thin structures and definition of modal radiation efficiency, with the aim of optimizing passive piezoelectric control.
- Model of a localized piezoelectric smart plate using a variational approach.
- Original approach to sound radiation control, with the controller acting only on most radiating modes.
- Original procedure for the optimization of the number of transducers and of their positioning, with the definition of a new cost function, the acoustic controllability.
- Critical analysis and optimization of semi-passive control networks suitable for sound radiation control.
- Modelling, design end optimization of an innovative distributed smart structure, the Piezoelectric Resistive Electrode plate.
- Application of distributed piezoelectric smart structures to sound radiation and transmission control.
- Setup of a realtime multi-input multi-output control system using open source software and drivers.
- Comparison between theoretical and experimental results for localized piezoelectric control and radiation properties of a plate.

6.3 Suggestions for future work

Further applications and extensions of the work on localized structures should concentrate on a better way of finding the modal shape of the real structure, for having a more efficient optimization. This can be efficiently done using the results provided by the acoustic imagery, or using a automated scanning laser vibrometer.
Moreover, for the distributed structures, and mainly for the PRE plate, extensions are possible on the construction of a prototype and on the addition of mechanical properties, e.g. viscoelastic behaviour, to the resistive layer.

6.4 Pubblications and conference proceedings

The material presented in this thesis was partially published in the following journal papers and conference proceedings.

1. Control of sound radiation and transmission by a piezoelectric plate with a optimized resistive electrode, Rosi, Pouget, dell'Isola, European Journal of Mechanics/A Solids (Submitted)

2. Control of sound radiation and transmission by distributed passive piezoelectric networks, Giuseppe Rosi, Roberto Paccapeli, Jo el Pouget, Francesco dell,Isola, part of: Proceedings of the 16th International Congress on Sound and Vibration (ICSV16), (CD-ROM proceedings) (ISBN: 978-83-60716-71-7) , pages: 1-7, 2009, International Institute of Sound and Vibration, Krakow, Poland

3. 9th European Conference on Applications of Polar Dielectrics (ECAPD9) 26-29 August 2008 Rome : Control of sound radiation and transmission by distributed passive piezoelectric networks

Bibliography

[3M 1993] 3M. Scotchdamp(tm) vibration control systems., 1993. 148

[Alessandroni 2002] Silvio Alessandroni, Francesco dell'Isola and Maurizio Porfiri. *A revival of electric analogs for vibrating mechanical systems aimed to their efficient control by PZT actuators*. International Journal of Solids and Structures, vol. 39, no. 5295-5324, 2002. 3, 81, 101

[Alessandroni 2004] Silvio Alessandroni, Ugo Andreaus, Francesco dell'Isola and Maurizio Porfiri. *Piezo-ElectroMechanical (PEM) Kirchhoff–Love plates*. European Journal of Mechanics A/Solids, vol. 23, pages 689–702, 2004. 3, 81, 98, 101

[Alessandroni 2005] S. Alessandroni, U. Andreaus, F. dell'Isola and M. Porfiri. *A passive electric controller for multimodal vibrations of thin plates*. Computers and Structures, vol. 83, no. 15-16, pages 1236–1250, Jun 2005. 81

[Bai 2002] Mingsian R. Bai and Mingchun Tsao. *Estimation of sound power of baffled planar sources using radiation matrices*. Journal of the Acoustical Society of America, vol. 112, no. 3, pages 876–883, 2002. 3, 13, 98, 99

[Batra 2005] R.C. Batra, F. dell'Isola, S. Vidoli and D. Vigilante. *Multimode vibration suppression with passive two-terminal distributed network incorporating piezoceramic transducers*. International Journal of Solids and Structures, vol. 42, pages 3115–3132, 2005. 101

[Baumann 2007] Oliver Nicholas Baumann and Stephen John Elliott. *Global optimization of distributed output feedback controllers*. Journal of Acoustical Society of America, vol. 122, no. 3, pages 1587–1594, 2007. 81

[Behrens 2003] S. Behrens, S.O.R. Moheimani and A.J. Fleming. *Multiple mode current flowing passive piezoelectric shunt controller*. Journal of Sound and Vibration, vol. 266, pages 929–942, 2003. 3, 41, 58, 101

[Benjeddou 2002] A. Benjeddou, J. F. Deu and S. Letombe. *Free vibrations of simply-supported piezoelectric adaptive plates: an exact sandwich formulation*. Thin-walled Structures, vol. 40, no. 7-8, pages 573–593, 2002. 42

[Borgiotti 1994] Giorgio V. Borgiotti and Kenneth E. Jones. *Frequency independence property of radiation spatial filters*. Journal of the Acoustical

Society of America, vol. 96, no. 6, pages 3516–3524, 1994. 3, 13, 15, 99

[Carabelli 2000] S. Carabelli and A. Tonoli. *System properties of flexible structures with self-sensing piezoelectric transducers.* Journal of Sound and Vibration, vol. 235, no. 1, pages 1 – 23, 2000. 121, 122

[Carneal 2004] James P. Carneal and ChrisR. Fuller. *An analytical and experimental investigation of active structural acoustic control of noise transmission through double panel systems.* Journal of Sound and Vibration, vol. 272, pages 749–771, 2004. 2, 3, 101

[Carrera 2007] E. Carrera and C. Fagiano. *Mixed piezoelectric plate elements with continuous transverse electric displacements.* Journal of mechanics materials and structures, vol. 2, no. 3, pages 421–438, Mar 2007. 42

[Caruso 2001] G. Caruso. *A critical analysis of electric shunt circuits employed in piezoelectric passive vibration damping.* Smart Materials and Structures, vol. 10, no. 5, pages 1059–1068, 2001. 40

[Chen 2009] C. P. Chen, C. H. Huang and Y. Y. Chen. *Vibration analysis and measurement for piezoceramic rectangular plates in resonance.* Journal of Sound and Vibration, vol. 326, no. 1-2, pages 251–262, 2009. 127

[Chomette 2008] B. Chomette, D. R. Remond, S. Chesne and L. Gaudiller. *Semi-adaptive modal control of on-board electronic boards using an identification method.* Smart Materials and Structures, vol. 17, no. 6, DEC 2008. 2

[Cremer 1973] Ungar Cremer Heckl. Structure borne sound. Springer-Verlag, 1973. 7, 16, 70, 96, 97

[dell'Isola 2003] Francesco dell'Isola, Maurizio Porfiri and Stefano Vidoli. *Piezo-ElectroMechanical (PEM) structures: passive vibration control using distributed piezoelectric transducers.* Comptes Rendus de l'Academie des Sciences, Mécanique, vol. 331, pages 69–76, 2003. 3, 81, 101

[Den Hartog 1956] J. Den Hartog. Mechanical vibrations. New York , McGraw-Hill, 1956. 40, 54, 95

[Ducarne 2009] Julien Ducarne. *Modeling and optimisation of non-linear vibration damping by switch shunting of piezoelectric elements.* PhD thesis, CNAM, 2009. 40, 127, 128

[Elliott 1990] SJ Elliott, PA Nelson, IM Stothers and CC Boucher. *In-flight experiments on active control o propeller-induced cabin noise*. Journal of Sound and Vibration, vol. 140, no. 2, pages 219–238, 1990. 81

[Elliott 1993] S. J. Elliott and M. E. Johnson. *Radiation modes and the active control of sound power*. Journal of Acoustical Society of America, vol. 94, no. 4, page 1993, October 1993. 3, 13, 15, 99

[Elliott 2002] SJ Elliott, P Gardonio, TC Sors and MJ Brennan. *Active vibroacoustic control with multiple local feedback loops*. Journal of the Acoustical Society of America, vol. 111, no. 2, pages 908–915, 2002. 81

[Elliott 2004] SJ Elliott, L Benassi, MJ Brennan, P Gardonio and X Huang. *Mobility analysis of active isolation systems*. Journal of Sound and Vibration, vol. 271, no. 1-2, pages 297–321, 2004. 81

[Elliott 2005] SJ Elliott. *Distributed control of sound and vibration*. Noise control engineering journal, vol. 53, no. 5, pages 165–180, 2005. International Symposium on Active Control of Sound and Vibration, Williamsburg, VA, SEP 20-22, 2004. 81

[Fahy 1985] F.J. Fahy. Sound and structural vibration. Academic Press, London., 1985. 16

[Fahy 2001] F.J. Fahy. Fundations of acoustical engineering. Elsevier, 2001. 7, 16, 96, 97

[Fernandes 2002] Amâncio Fernandes and Joël Pouget. *An accurate modelling of piezoelectric multi-layer plates*. European Journal of Mechanics A/Solids, vol. 21, pages 629–651, 2002. 42

[Filippi 1984] P. J. T. Filippi. Acoustique générale. Les editions de phisique, 1984. 7, 16, 96, 97, 101

[Fleming 2003] A. J. Fleming, S. Behrens and S. O. R. Moheimani. *Reducing the inductance requirements of piezoelectric shunt damping systems*. Smart materials and structures, vol. 12, no. 1, pages 57–64, 2003. 40

[Frampton 2006] KD Frampton. *Vibro-acoustic control with a distributed sensor network*. Journal of the Acoustical Society of America, vol. 119, no. 4, pages 2170–2177, 2006. 81

[Gardonio 2004] P. Gardonio, E. Bianchi and S.J. Elliott. *Smart panel with multiple decentralized units for the control of sound transmission. Part I: theoretical predictions*. Journal of Sound and Vibration, vol. 274, pages 163–192, 2004. 2, 81

[Gardonio 2005] Paolo Gardonio and Stephen J. Elliott. *Smart panels with velocity feedback control systems using triangularly shaped strain actuators*. Journal of the Acoustical Society of America, vol. 117, no. 4, pages 2046–2064, April 2005. 2, 81

[Gawronski 1997] W Gawronski. *Actuator and sensor placement for structural testing and control*. Journal of Sound and Vibration, vol. 208, no. 1, pages 101–109, NOV 1997. 2

[Giorgio 2009] I. Giorgio, A. Culla and D. Del Vescovo. *Multimode vibration control using several piezoelectric transducers shunted with a multiterminal network*. Archive of Applied Mechanics, vol. 79, no. 9, pages 859–879, Sep 2009. 41, 59, 64, 127, 128

[Hagood 1991] N. W. Hagood and A. von Flotow. *Damping of structural vibrations with piezoelectric materials and passive electrical networks*. Journal of Sound and Vibrations, vol. 146, pages 243–268, 1991. 40, 52, 56, 121

[Halim 2003] Dunant Halim and S.O. Reza Moheimani. *An optimization approach to optimal placement of collocated piezoelectric actuators and sensors on a thin plate*. Mechatronics, vol. 13, pages 27–47, 2003. 2, 41, 64, 67

[Hurlebaus 2006] S. Hurlebaus and L. Gaul. *Smart structure dynamics*. mechanical system and signal processing, vol. 20, no. 2, pages 255–281, 2006. 42

[IEEE 1987] IEEE. Ieee standard on piezoelectricity - ieee std 176-1987. Institute of Electrical and Electronic Engineers, 1987. 47, 87

[ISO 3745 1977] ISO 3745. Iso 3745, acoustics—determination of sound power levels of noise sources—precision methods for anechoic and semi-anechoic rooms, 1977. iso 3745, acoustics—determination of sound power levels of noise sources—precision methods for anechoic and semi-anechoic rooms. 1977. 11, 96, 98, 132, 151

[Kinsler 2000] Lawrence E Kinsler, Austin R. Frey, Alan B. Coppens and James V. Sanders. Fundamentals of acoustics. John Wiley and Sons, 2000. 35

[Kuttruff 2007] Hinrich Kuttruff. Acoustics. Taylor and Francis, 2007. 35, 151

[Larbi 2006] W. Larbi, J. F. Deu and R. Ohayon. *A new finite element formulation for internal acoustic problems with dissipative walls*. Inter-

national journal for numerical methods in engineering, vol. 68, no. 3, pages 381–399, 2006. 1

[Lee 1999a] J.C. Lee and J.C. Chen. *Active control of sound radiation from a rectangular plate excited by line moment.* Journal of Sound and Vibration, vol. 220, no. 1, pages 99–115, 1999. 2

[Lee 1999b] Jen Chien Lee and Jish Chson Chen. *Active control of sound radiation from rectangular plates using multiple piezoelectric actuators.* Applied Acoustics, vol. 57, pages 327–343, 1999. 2, 3, 101

[Li 2007] Sheng Li and Xianhui Li. *The effects of distributed masses on acoustic radiation behavior of plates.* Applied Acoustics, 2007. 1

[MasahiroToyoda 2005] MasahiroToyoda and Daiji Takahashi. *Reduction of acoustic radiation by impedance control with a perforated absorber system.* Journal of Sound and Vibration, vol. 286, pages 601–614, 2005. 1

[Maurini 2004] C Maurini, F dell'Isola and D Del Vescovo. *Comparison of piezoelectronic networks acting as distributed vibration absorbers.* mechanical system and signal processing, vol. 18, no. 5, pages 1243–1271, SEP 2004. 81

[Maurini 2005] Corrado Maurini. *Piezoelectric composites for distributed passive electric control: beam modelling, modal analysis, and experimental implementation.* PhD thesis, Université Paris 6 - Sapienza Università di Roma, 2005. 3, 81, 94, 101

[Maurini 2007] C. Maurini, M. Porfiri and J. Pouget. *On the identification of modal couplings and inherent capacitances of piezoelectric structures - art. no. 65230U*, 2007. 127

[Moheimani 1999] S.O.R. Moheimani and T. Ryall. *Considerations on placement of piezoceramic actuators that are used in structural vibration control.* In Proceedings of the 38th IEEE Conference on Decision and Control (Cat. No.99CH36304), numéro vol.2, pages 1118–23 vol.2, Piscataway, NJ, USA, 1999 1999. IEEE Control Syst. Soc, IEEE. Proceedings of 1999 Conference on Decision and Control, 7-10 December 1999, Phoenix, AZ, USA. 41, 67

[Ohayon 1998] Roger Ohayon and Christian Soize. Structural acoustics and vibration. Academic Press, London., 1998. 7

[Oniszczuk 2004] Z. Oniszczuk. *Forced transverse vibrations of an elastically connected complex rectangular simply supported double-plate system.* Journal of Sound and Vibration, vol. 270, pages 997–1011, 2004. 35

[Ozer 2003] M. Bulent Ozer and Thomas J. Royston. *Passively minimizing structural sound radiation using shunted piezoelectric materials.* Journal of Acoustical Society of America, vol. 114, no. 4, pages 1934–1946, 2003. 3, 40, 41, 101

[Porfiri 2007] M. Porfiri, C. Maurini and J. Pouget. *Identification of electromechanical modal parameters of linear piezoelectric structures.* Smart Materials and Structures, vol. 16, no. 2, pages 323–331, Apr 2007. 121, 122, 127

[Serrand 2000] M Serrand and SJ Elliott. *Multichannel feedback control for the isolation of base-excited vibration.* Journal of Sound and Vibration, vol. 234, no. 4, pages 681–704, 2000. 81

[Strassberger 2000] Michael Strassberger and Heinz Waller. *Active noise reduction by structural control using piezoelectric actuators.* Mechatronics, vol. 10, pages 851–868, 2000. 2

[Sze 004] KY Sze, XM Yang and H Fan. *Electric assumptions for piezoelectric laminate analysis.* International Journal of Solids and Structures, vol. 41, no. 9-10, pages 2363–2382, MAY 2004. 42

[Teresi 1997] L. Teresi and A. Terio. *On variational Approaches to Plate Models.* Meccanica, vol. 32, no. 143-156, 1997. 42

[Thomas 2009] O. Thomas, J. F. Deu and J. Ducarne. *Vibrations of an elastic structure with shunted piezoelectric patches: efficient finite element formulation and electromechanical coupling coefficients.* International journal for numerical methods in engineering, vol. 80, no. 2, pages 235–268, Oct 2009. 40, 127

[Trindade 2007] M. A. Trindade. *Optimization of active-passive damping treatments using piezoelectric and viscoelastic materials.* Smart Materials and Structures, vol. 16, no. 6, pages 2159–2168, DEC 2007. 2

[Trindade 2008] Marcelo A. Trindade and Ayech Benjeddou. *Refined sandwich model for the vibration of beams with embedded shear piezoelectric actuators and sensors.* Computers and Structures, vol. 86, no. 859-869, 2008. 42

[Wallace 1972] C.E. Wallace. *Radiation Resistance of a Rectangular Panel.* Journal of the Acoustical Society of America, vol. 51, no. 3, pages 946–952, 1972. 3

[Wu 1996] S. Y. Wu. *Piezoelectric shunts with a parallel R-L circuit for structural damping and vibration control.* In Proc. SPIE, Smart Materials and Structure, volume 2720, pages 259–269, 1996. 60

[Zhang 2004] Wenfeng Zhang, Jinhao Qiu and Junji Tani. *Robust Vibration Control of a Plate Using Self-sensing Actuators of Piezoelectric Patches.* Journal of Intelligent Material Systems and Structures, vol. 15, pages 923–931, 2004. 2, 3, 101

Appendix A

Parameters used in simulations and experiments

A.1 Parameters of the simply supported plate

In this section the parameters used for the simulation described in section 3 are presented:

Coefficient	Value	Description
Y	$70 \times 10^9\ N/m^2$	Young Modulus
ν	.33	Poisson Ratio
ρ	$2700\ Kg/m^3$	Mass density
a	$.21\ m$	Length
b	$.30\ m$	Width
h	$2 \times 10^{-3}\ m$	Thickness

Table A.1: Aluminium plate constitutive parameters and dimensions of the plate used in simulations

Coefficient	Value	Description
Y_p	$6.6 \times 10^{10}\ N/m^2$	Young Modulus
ν_p	.29	Poisson Ratio
ρ_p	$7500\ Kg/m^3$	Mass density
d_{31}	$-274 \times 10^{-12}\ m/V$	Coupling coefficient
ε_{33}^S	$3.0104 \times 10^{-8}\ Fm^{-1}$	Dielectric constant
h_p	$0.20 \times 10^{-3}\ m$	Thickness

Table A.2: Piezoelectric transducers constitutive parameters and dimensions using in simulations

A.2 Characteristics of the PRE plate

In this section the parameters used for the simulation described in section 4 are presented.
The dimensions of the aluminium plate are in table A.3 The plate is assumed to be covered by a piezoelectric layer having the properties shown in Table

A.5. The properties of the viscoelastic layer are listed in Table A.4. The characteristic quantities in the simulations are presented in Table A.6. The optimal values for the resistive layer are presented in Table A.7.

Coefficient	Value	Description
Y	$70 \times 10^9\ N/m^2$	Young Modulus
ν	.33	Poisson Ratio
ρ	$2700\ Kg/m^3$	Mass density
a	$.21\ m$	Length
b	$.30\ m$	Width
h	$2 \times 10^{-3}\ m$	Thickness

Table A.3: Aluminium plate constitutive parameters and dimensions

Coefficient	Value	Description
Y_v^*	See reference [3M 1993]	Complex Young Modulus
ν_v	.49	Poisson Ratio
ρ_v	$1000\ Kg/m^3$	Mass density
h_v	$2 \times 10^{-3}\ m$	Thickness

Table A.4: Viscoelastic material parameters and dimensions

Coefficient	Value	Description
Y_p	$6.6 \times 10^{10}\ N/m^2$	Young Modulus
ν_p	.29	Poisson Ratio
ρ_p	$7500\ Kg/m^3$	Mass density
d_{31}	$-274 \times 10^{-12}\ m/V$	Coupling coefficient
ε_{33}^S	$3.0104 \times 10^{-8}\ Fm^{-1}$	Dielectric constant
h_p	$0.267 \times 10^{-3}\ m$	Thickness

Table A.5: Piezoelectric transducers constitutive parameters and dimensions

Coefficient	Value	Description
t_0	$1\ s$	Characteristic time
Ψ_0	$1\ Vs$	Characteristic flux linkage
W_0	$10 \times 10^{-3}\ m$	Characteristic deflection

Table A.6: Characteristic quantities

Coefficient	Value	Description
Y	$70 \times 10^9\ N/m^2$	Young Modulus
ν	.33	Poisson Ratio
ρ	$2700\ Kg/m^3$	Mass density
a	$.21\ m$	Length
b	$.30\ m$	Width
h	$2 \times 10^{-3}\ m$	Thickness

Table A.8: Aluminium plate constitutive parameters and dimensions of the plate used in the experiments

Coefficient	Value	Description
h_r	$1 \times 10^{-4}\ m$	Thickness
ϱ_r	$.231\ \Omega \cdot m$	Specific resistivity

Table A.7: Resistive layer properties

A.3 Characteristics of the smart plate used in the experiments

Coefficient	Value	Description
Y_p	$6.6 \times 10^{10}\ N/m^2$	Young Modulus
ν_p	.29	Poisson Ratio
ρ_p	$7500\ Kg/m^3$	Mass density
d_{31}	$-274 \times 10^{-12}\ m/V$	Coupling coefficient
ε_{33}^S	$3.0104 \times 10^{-8}\ Fm^{-1}$	Dielectric constant
h_p	$0.20 \times 10^{-3}\ m$	Thickness

Table A.9: Piezoelectric transducers constitutive parameters and dimensions using in the experiments

List of Figures

List of Tables